Electronic Supplementary Material (ESI) for Energy & Environmental Science.

Supplementary Information

H-buffer effects boosting H-spillover for efficient hydrogen evolution reaction

Yan et al.

Table of Contents

Methods

Materials. Sucrose ($C_{12}H_{22}O_{11}$, 99.9%), sodium bicarbonate ($NaHCO_3$, 99.8%), and chloroplatinic acid hexahydrate ($H_2PtCl_6{\cdot}H_2O$, AR) were purchased from Shanghai Aladdin Bio-Chem Technology Co., Ltd. Phosphomolybdic acid hydrate ($H_3P(Mo_3O_{10})_4{\cdot}xH_2O$, {$PMo_{12}$} AR) and silicotungstic acid ($SiO_2{\cdot}12WO_3{\cdot}26H_2O$, {$SiW_{12}$} AR) were purchased from Shanghai Macklin Biochemical Co., Ltd. Phosphotungstic acid hydrate ($H_3O_{40}PW_{12}{\cdot}xH_2O$,{$PW_{12}$}99%) was obtained from Shanghai Titan Scientific Co., Ltd. Silicomolybdic acid solution ($H_4SiO_4{\cdot}12MoO_3$,{$SiMo_{12}$} AR) and Nafion (5 wt.%) were from Sigma-Aldrich. Activated carbon was bought from Jiangsu Xianfeng Nanomaterials Technology Co., Ltd.

Preparation of Pt_1@POMs@PC. POMs@PC samples (PMo_{12}@PC, PW_{12}@PC, $SiMo_{12}$@PC, and SiW_{12}@PC) were firstly synthesized via our reported method.[1] Then these POMs@PC (25 mg) samples were dispersed in 10 mL ultrapure water, followed by magnetic stirring for 20 min to obtain a homogeneous suspension. Secondly, 260 μL of $H_2PtCl_6{\cdot}6H_2O$ aqueous solution (20 mg/mL) was added slowly to achieve the equimolar coordination between Pt and POMs. After stirring the mixture for 16 h at 60 ℃, the suspension was separated by centrifugation. The precipitates were washed with ultrapure water several times and then dried at 60 ℃ under vacuum overnight. The obtained samples were denoted as Pt_1@POMs@PC (viz. Pt_1@PMo_{12}@PC, Pt_1@PW_{12}@PC, Pt_1@$SiMo_{12}$@PC, and Pt_1@SiW_{12}@PC). To ensure that each Pt is anchored in the nano-capturer, a series of Pt_x@POMs@PC, where *x* means mole ratios of Pt and POMs (0, 0.2, 0.4, 0.6, 0.8, 1, 1.2, 1.4) were also synthesized. As controls, pure PC and commercial activated carbon (AC)-supported POMs were also used to support Pt, expressed as Pt_1@PC and Pt-POMs/AC, respectively.

Materials characterizations. XRD patterns were collected on a Rigaku D/Max Ultima IV (Cu-Kα radiation, λ = 1.5418 Å) diffractometer with filtered. The morphology of the samples was characterized by HRTEM (JEM-2010, accelerating voltage of 200 kV), and high-angle annular dark-field scanning transmission electron microscopy (JEOL JEM-ARM200F STEM with a spherical aberration corrector, accelerating voltage of 200 kV). EDS data was collected by an X-MaxN100TLE detector. Ionic (Mo, W, and Pt) concentration was analyzed by inductively coupled plasma-optical emission spectroscopy (ICP-OES; Avio 200). UV–vis spectrum was conducted on a TU-1950 spectrophotometer. Nitrogen adsorption/desorption experiments were carried out on 77 K of Micromeritics ASAP 2020 equipment. The Brunauer–Emmett–Teller (BET) model was used for the specific surface area determination. Elemental electron binding energy was measured by X-ray photoelectron spectroscopy (XPS; ESCALAB 250XI). X-ray absorption fine structure (XAFS) including X-ray absorption near-edge structure (XANES) and extended X-ray absorption fine structure (EXAFS) of the Pt_1@PMo_{12}@PC and Pt_1@PC were collected at the SPring-8 14b2, where a pair of channel-cut Si (111) crystals was used in the monochromator (**Note S4**).

Electrochemical measurements. All electrochemical experiments were conducted on a CHI760E electrochemical workstation in a three-electrode system at room temperature. The catalyst ink was prepared by ultrasonically dispersing 2 mg of catalysts into 750 μL of a mixture containing 550 μL water, 180 μL isopropanol, and 20 μL Nafion for 2 h. Then, a glassy carbon electrode (GCE: diameter=3 mm) cast by catalyst ink (3.5 μL), a graphite rod (diameter=5 mm), and a saturated calomel electrode (SCE) were used as the working electrode, counter electrode, and reference electrode, respectively. Note that Pt contents in Pt_1@POMs@PC series determined by ICP-OES are in the range of 2.1–3.8 wt.% (**Table S12**), which are close to XPS results (**Table**

S13). The calibration of SCE electrode was performed in a high-purity H_2-saturated 0.5 M H_2SO_4 with two Pt foils used as the working electrode and counter electrode, respectively, while the SCE was calibrated as the reference electrode. Cyclic voltammetry (CV) was conducted at a scan rate of 1 mV s^{-1}, and the average of the two potentials at which the current crossed zero was taken as the thermodynamic potential for the hydrogen electrode reaction. As shown in **Fig. S68**, the CV result of RHE calibration in 0.5 M H_2SO_4 can be described as E(RHE) =E(SCE) + 0.2636 V. Linear sweep voltammetry was recorded at 5 mV s^{-1} in Ar-saturated 0.5 M H_2SO_4. Tafel slopes were determined by plotting the overpotential *vs*. the logarithm of current density (log |j|). EIS measurements were conducted in the frequency range from 10^5 Hz to 10^{-2} Hz with an amplitude of 5 mV at various HER overpotentials. The stability tests for the Pt_1@POMs@PC, Pt-POMs/AC, and Pt_1@C were conducted using chronopotentiometry at a current density of 10 mA cm^{-2}. The mass activity and TOF information can be found in **Note S5**. H/D kinetic isotope effects (KIEs) experiment and pH-dependence measurement were also conducted to verify the occurrence of H-spillover.

In situ Raman spectroscopy measurements. In-situ Raman spectra were collected in a confocal Raman microscopic spectrometer (Renishaw, inVia Qontorin) with an excitation of 532 nm laser while electrochemical curves were collected using a CHI 760E electrochemical workstation in 0.5 M H_2SO_4. The catalyst ink was dropped on a 3×3 mm hydrophobic carbon paper, followed by drying at 25 °C. In the in-situ Raman test, the carbon rod is used as a counter electrode, and the reference electrode is an Ag/AgCl electrode. Chronoamperometry was performed at various potentials in 0.5 M H_2SO_4 during the Raman measurement.

Computational Details

Extended Tight-binding (xTB) calculations. All extended tight-binding calculations were done by xTB 6.4.0 package.[2] Geometry Frequency Noncovalent 0 (GFN0)-xTB level of parametrization was adapted for geometry optimization[3]. To simulate the nano-porous graphite, 4 layers of graphite were constructed on the *z*-direction. The hexagonal graphite cell was redefined to be an orthogonal cell. A 9 × 16 supercell was used, which has a dimension of 30 Å on the x-direction and 32 Å on the y-direction. The model was cleaved out to be non-periodic and the dangling bonds on the edge of graphite were passivated by hydrogen atoms. A 12.6 Å nano-pore was constructed by creating a semi-sphere vacancy on the graphite surface as suggested by previously reported works.[1, 4, 5] Vacancies are created only on the first three carbon layers as the radius of the semi-sphere does not exceed 8 Å, which indicates that the 4th layer remains at the bottom of the sphere. The size of the nano-pore is referred to as the diameter of the pore on the first layer. The binding energy (E_b) of Pt in Pt_1@POMs@G is defined as:

$$E_b = E(Pt_1@POMs@G) - E(POMs@G) - E(Pt)$$

where E(Pt_1@POMs@G) is the total energy of the Pt loaded on the POMs@G substrate, E(POMs@G) is the total energy of the isolated POMs@G substrate, and E(Pt) is the total energy of isolated Pt atom. Therefore, a more negative E_b corresponds to a more favored adsorption. E_b for other models can be seen in **Note S6.**

To investigate whether Pt will agglomerate or not, we have carried out theoretical calculations on thermodynamic processes. The cohesive energies per Pt atom ($E_{coh\text{-}Pt}$) from thermodynamics are evaluated as:

$$E_{coh\text{-}Pt} = (E_{cluster} - N \times E_{atom})/N$$

where $E_{cluster}$ is the energy of a Pt cluster consisting of a certain number (*N)* of Pt atoms, E_{atom} is the energy of a single Pt atom in a vacuum, and $E_{coh\text{-}Pt}$ refers to the energy gained when isolated single atoms are assembled into clusters. A more negative $E_{coh\text{-}Pt}$ indicates a more stable Pt cluster. To model the Pt cluster or nanoparticle, Wulff construction was employed to minimize the total surface energy of Pt, as reported by Tran et al[6]

All involved structures are isolated and non-periodic to avoid the periodic Coulombic interaction for charged systems (i.e., charged slabs). The charge density difference of Pt_1@POMs@G ($\Delta\rho$) is defined as:

$$\Delta\rho = \rho(Pt_1@POMs@G) - \rho(POMs@G) - \rho(Pt)$$

where ρ (Pt_1@POMs@G) is the electron density of the Pt loaded on the POMs@G substrate, ρ(POMs@G) is the electron density of the isolated POMs@G substrate, and ρ(Pt) is the electron density of the isolated Pt atom. Thus, a positive $\Delta\rho$ indicates obtaining electrons and a negative $\Delta\rho$ indicates losing electrons. The charge density difference and Hirshfeld population analysis were done by using *Multiwfn* software.[7] $\Delta\rho$ for other models can be seen in **Note S7.**

The H adsorption-free energy (G_{ads}) is defined as:

$$\Delta G_{ads} = G[H + surf] - G[surf] - \tfrac{1}{2}G[H_2]$$

where G[H+surf] is the free energy of the H absorbed surface, G[surf] is the free energy of the surface, and $G[H_2]$ is the free energy of the surface. The free energy change of the surface before and after adsorption is neglected:

$$\Delta G_{ads} = (E[H_{abs} + surf] + ZPE[H_{abs}] - TS[H_{abs}]) - E[surf] - \tfrac{1}{2}(E[H_2] + ZPE[H_2] - TS[H_2])$$

$$\Delta G_{ads} = \Delta E + \Delta ZPE - T\Delta S$$

where E is the electronic energy, ZPE is the zero point energy, and S is the entropy. H_{abs} refers to the absorbed H. The electronic energy change (ΔE) is:

$$\Delta E = E[H + surf] - E[surf] - \tfrac{1}{2}E[H_2]$$

The entropy change (ΔS) is:

$$\Delta S = S[H_{absorb}] - \tfrac{1}{2}S[H_2]$$

The ZPE change (ΔZPE) is:

$$\Delta ZPE = ZPE[H_{abs}] - \tfrac{1}{2}ZPE[H_2]$$

The estimated contribution from ΔZPE and $T\Delta S$ at 298 K is approximated to be 0.24 eV[8], which gives that:

$$\Delta G_{ads} = \Delta E + 0.24\ eV$$

Molecular dynamics (MD) simulation. molecular dynamics (MD) studies have been conducted to verify the kinetic stabilities of the absorbed Pt single atoms. Note that the Geometry Frequency Noncovalent force field (GFN-FF)[9] was adopted. Meanwhile, the canonical ensemble (NVT) was used with a targeted temperature of 298.15K after 50 ps (the time step for propagation is 1 fs) for Pt_1@PMo_{12}@G-01, Pt_1@PW_{12}@G-01, Pt_1@$SiMo_{12}$@G-01, and Pt_1@SiW_{12}@G-01.

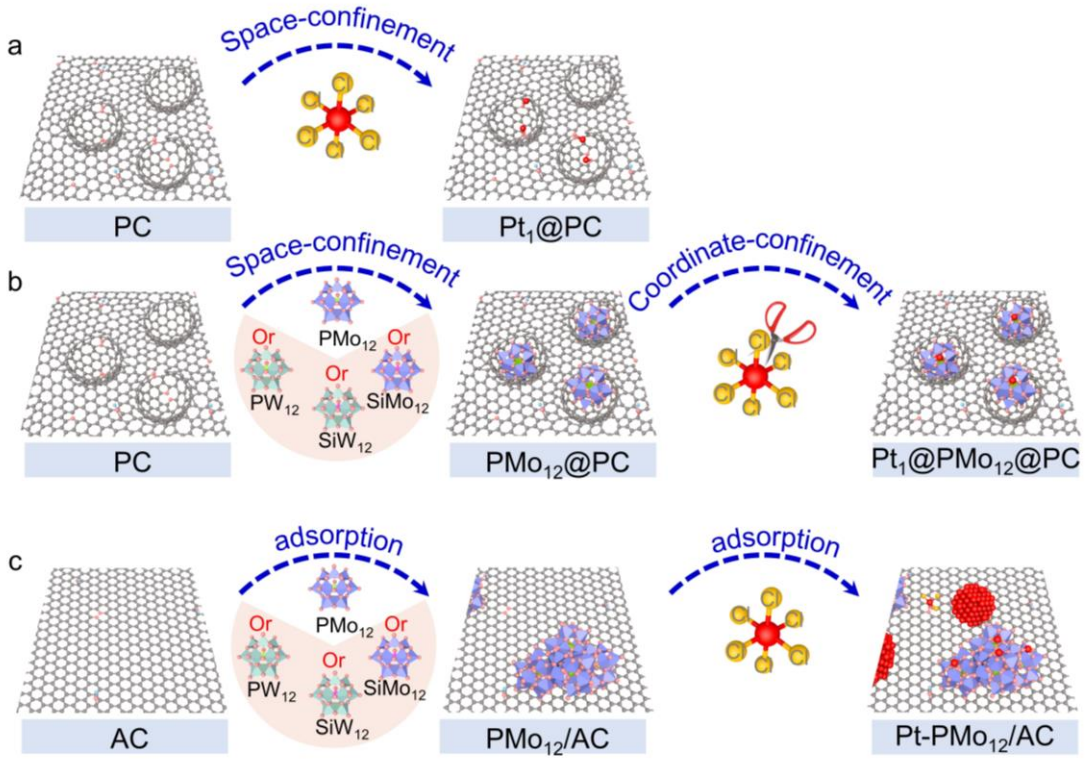

Fig. S1. Schematic illustration of the preparation process for (**a**) Pt_1@PC, (**b**) Pt_1@POMs@PC, and (**c**) Pt-POMs/AC.

Note that we take PMo_{12} here as an example to illustrate the preparation process.

Pt was confined in the PC support by wet impregnation. The exceptional affinity of PC for Pt can be attributed to its oxygen-enriched hydroxyl, and carboxyl groups on the surface inherited from precursor. We found that when commercial AC was used as the substrate, Pt nanoparticles were generated, which is due to lower binding energies between the Pt atom and POMs/AC, as confirmed by calculations. Because unconfined POMs are also at risk of agglomeration.

Note that both pure Pt precursors and POMs can be dispersed in the liquid-phase systems. Owing to the limited coordination sites on the POMs surface, when the unsaturated sites of POMs are completely occupied by single Pt atoms, an excess of Pt precursors is prone to agglomerate into NPs until the surface is stabilized by POMs. Even though reducing the input of metal precursors, the generation of NPs can hardly be completely inhibited due to the spatially inhomogeneous dispersion caused by the high mobility of metal precursors. Hence, to avoid their aggregation, it is necessary to restrict the spatial dispersion and mobility of POMs before mixing with Pt precursors.[10]

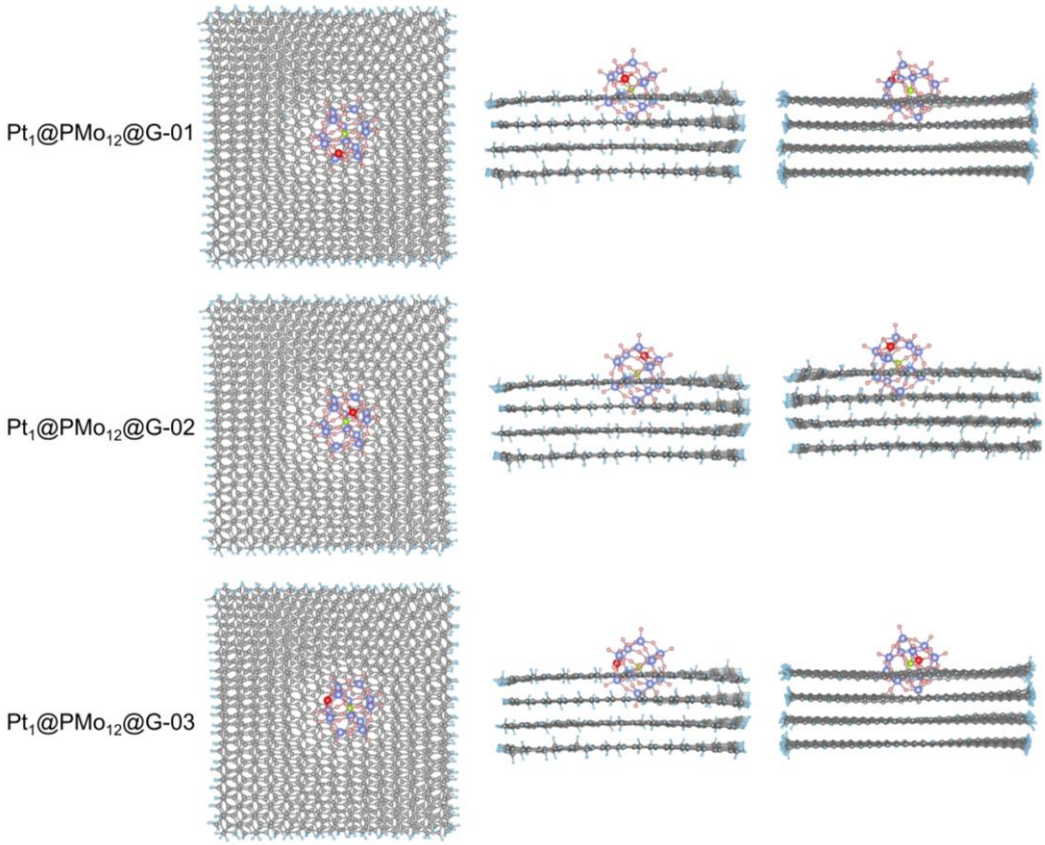

Fig. S2. Optimized structural models showing the top view, front view, and side view of $Pt_1@PMo_{12}@G$-01, $Pt_1@PMo_{12}@G$-02, and $Pt_1@PMo_{12}@G$-03 with the Pt atom anchored on the O4H site.

Note that there are three O4H sites exposed on the surface of confined POMs. POMs@G-01, POMs@G-02, and POMs@G-03 refer to different O4H site models.

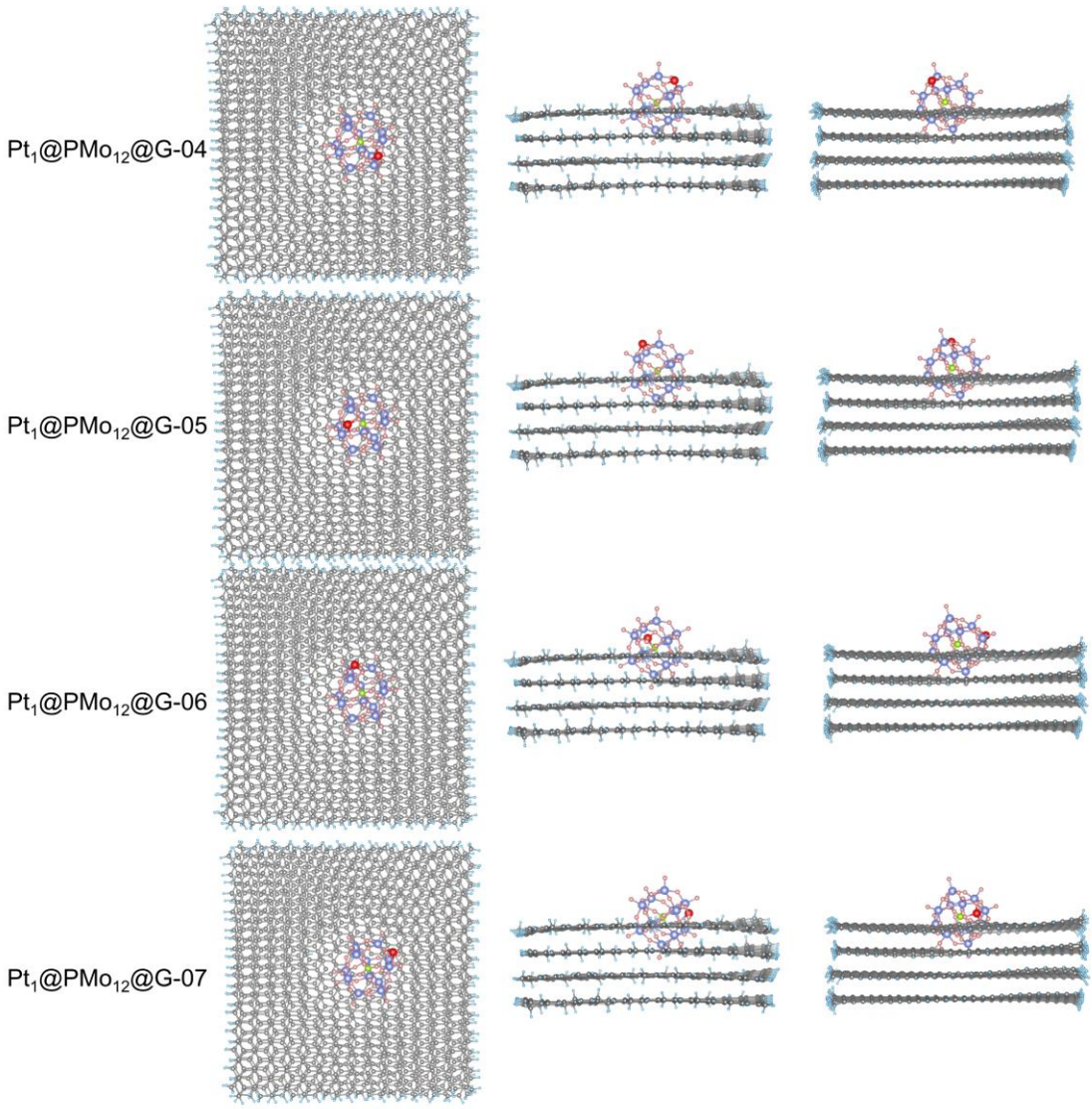

Fig. S3. Optimized structural models showing the top view, front view, and side view of $Pt_1@PMo_{12}@G$-04, $Pt_1@PMo_{12}@G$-05, $Pt_1@PMo_{12}@G$-06, and $Pt_1@PMo_{12}@G$-07 with the Pt atom anchored on the O3H site.

Note that there are four O3H sites exposed on the surface of confined POMs. POMs@G-04, POMs@G-05, POMs@G-06, and POMs@G-07 refer to different O3H site models.

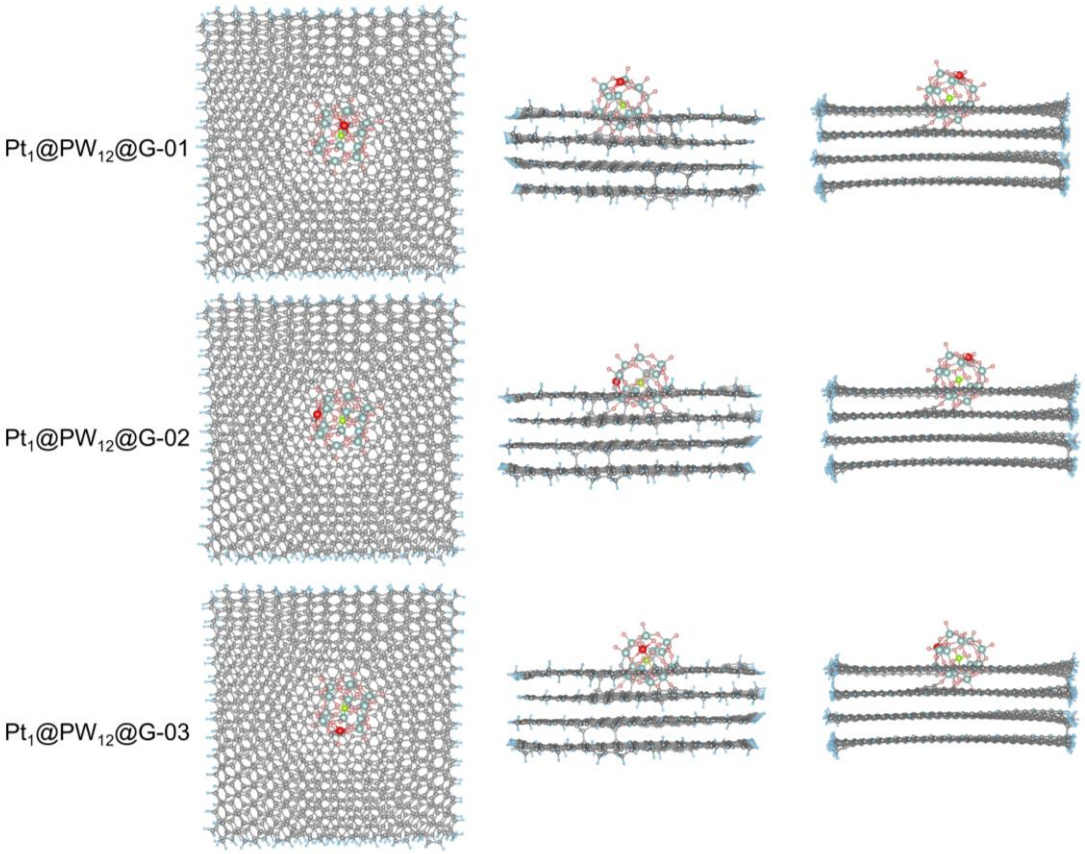

Fig. S4. Optimized structural models showing the top view, front view, and side view of $Pt_1@PW_{12}@G$-01, $Pt_1@PW_{12}@G$-02, and $Pt_1@PW_{12}@G$-03 with the Pt atom anchored at the O4H site.

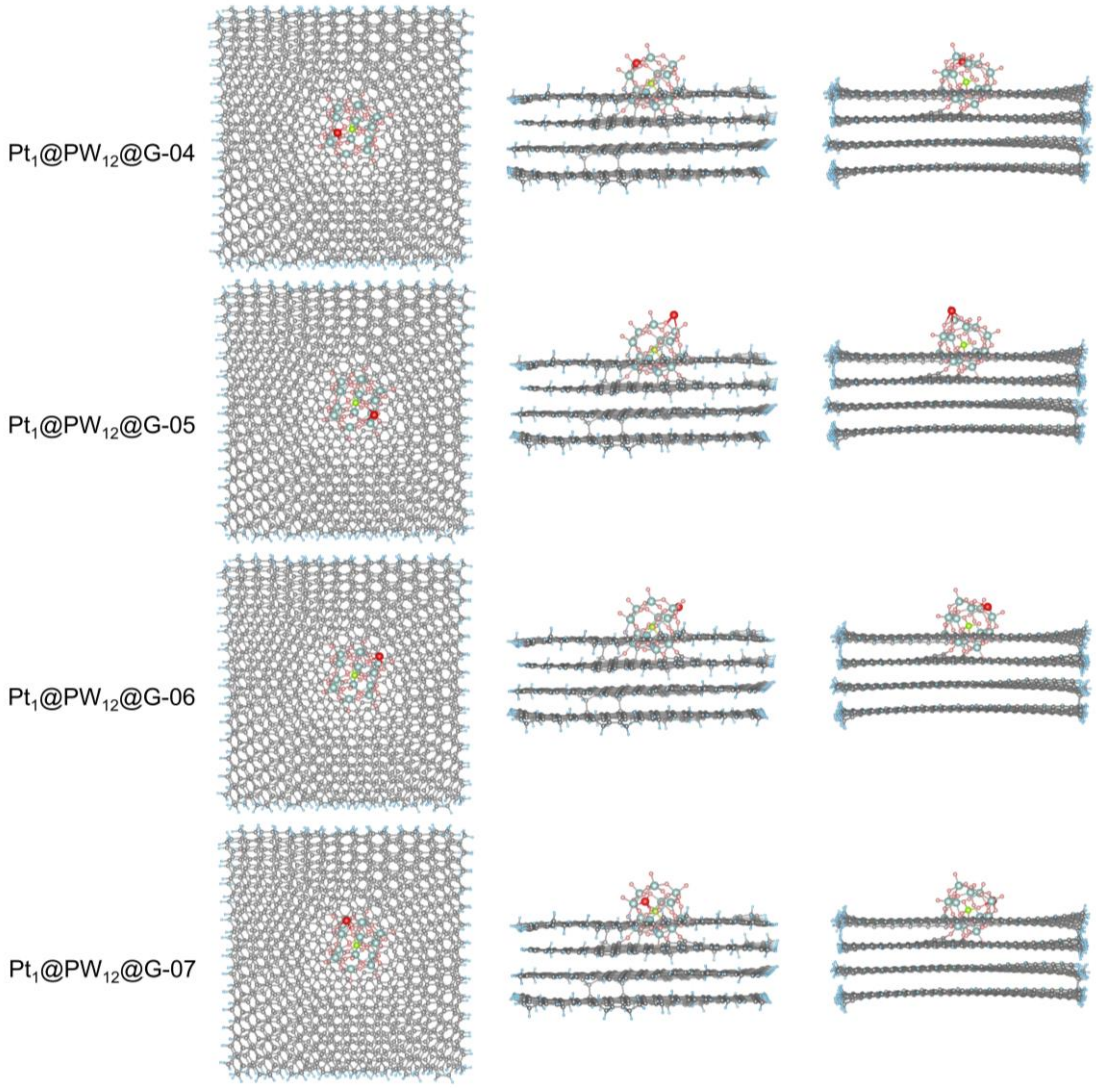

Fig. S5. Optimized structural models showing the top view, front view, and side view of $Pt_1@PW_{12}@G$-04, $Pt_1@PW_{12}@G$-05, $Pt_1@PW_{12}@G$-06, and $Pt_1@PW_{12}@G$-07 with the Pt atom anchored at the O3H site.

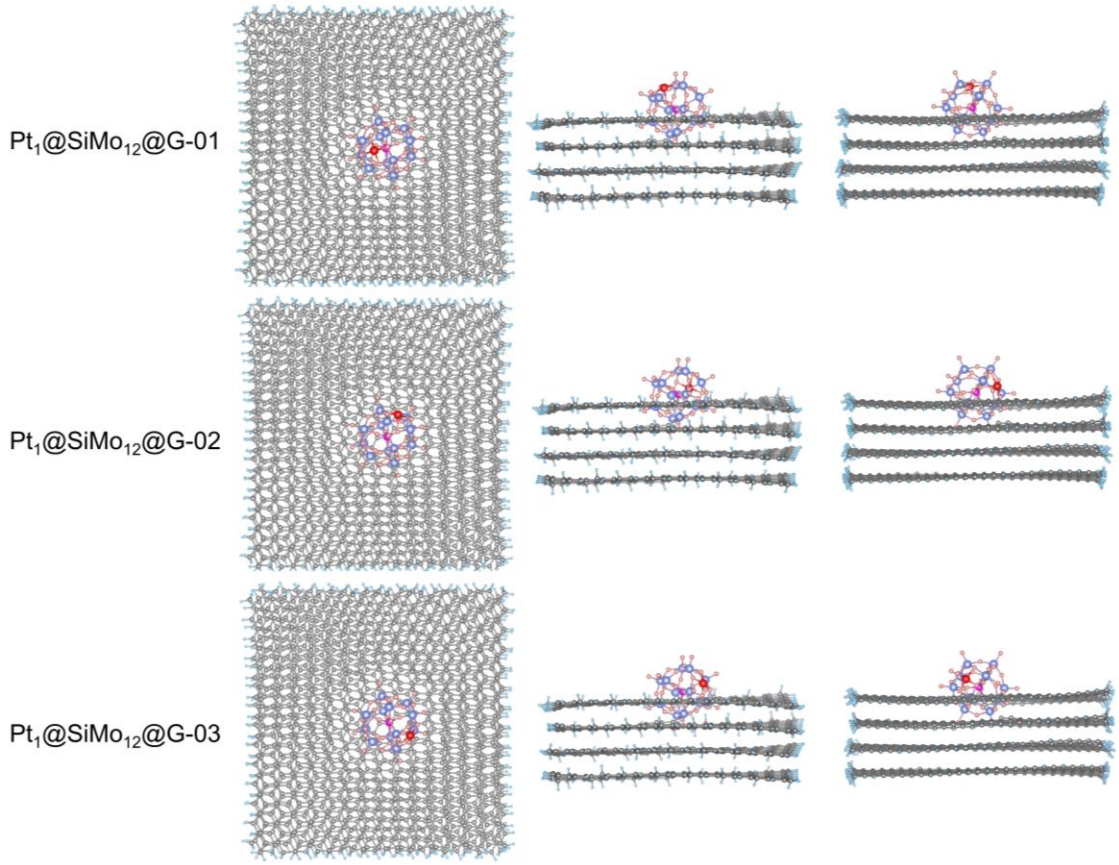

Fig. S6. Optimized structural models showing the top view, front view, and side view of $Pt_1@SiMo_{12}@G$-01, $Pt_1@SiMo_{12}@G$-02, and $Pt_1@SiMo_{12}@G$-03 with the Pt atom anchored at the O4H site.

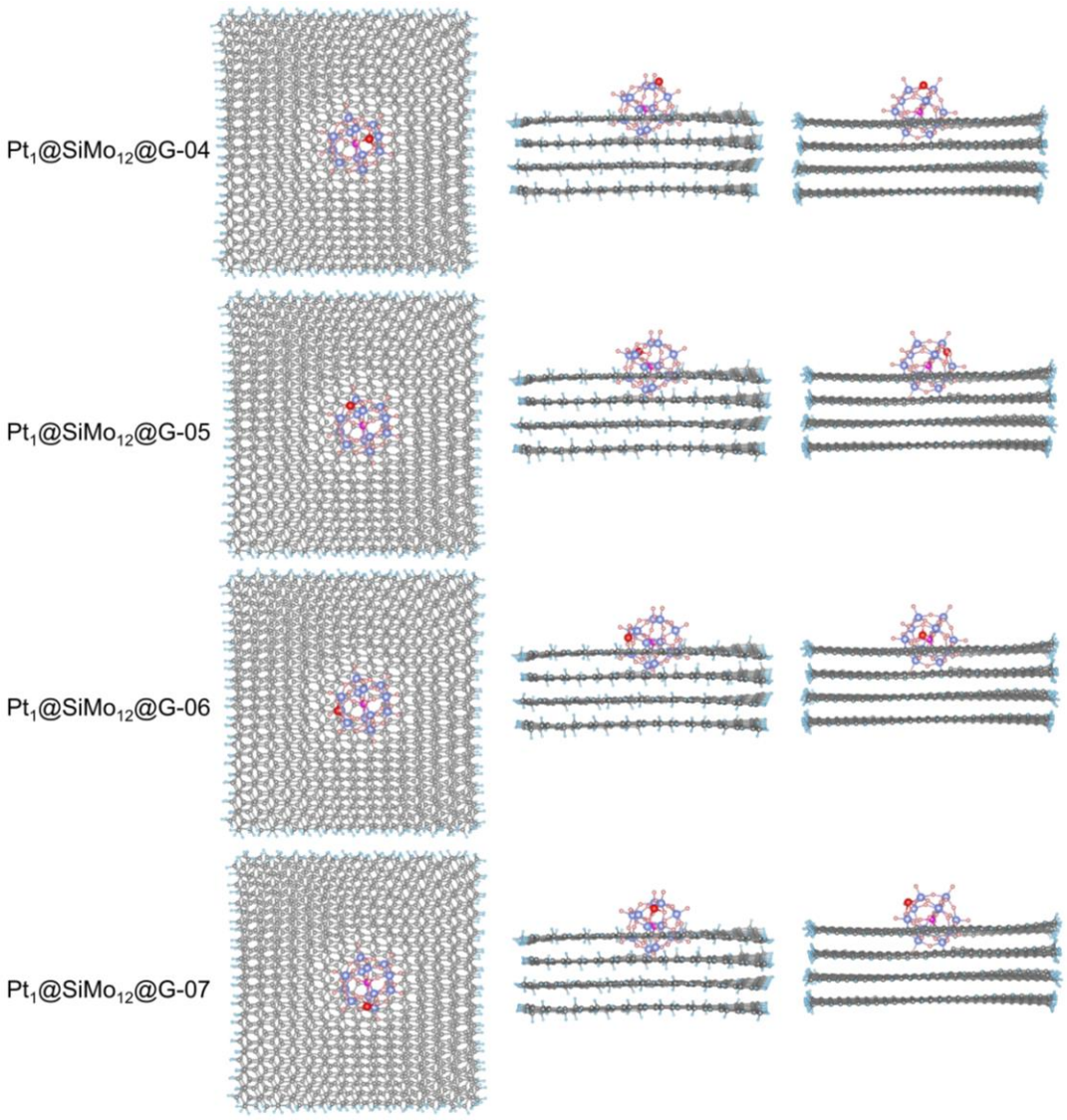

Fig. S7. Optimized structural models showing the top view, front view, and side view of $Pt_1@SiMo_{12}@G$-04, $Pt_1@SiMo_{12}@G$-05, $Pt_1@SiMo_{12}@G$-06, and $Pt_1@SiMo_{12}@G$-07 with the Pt atom anchored at the O3H site.

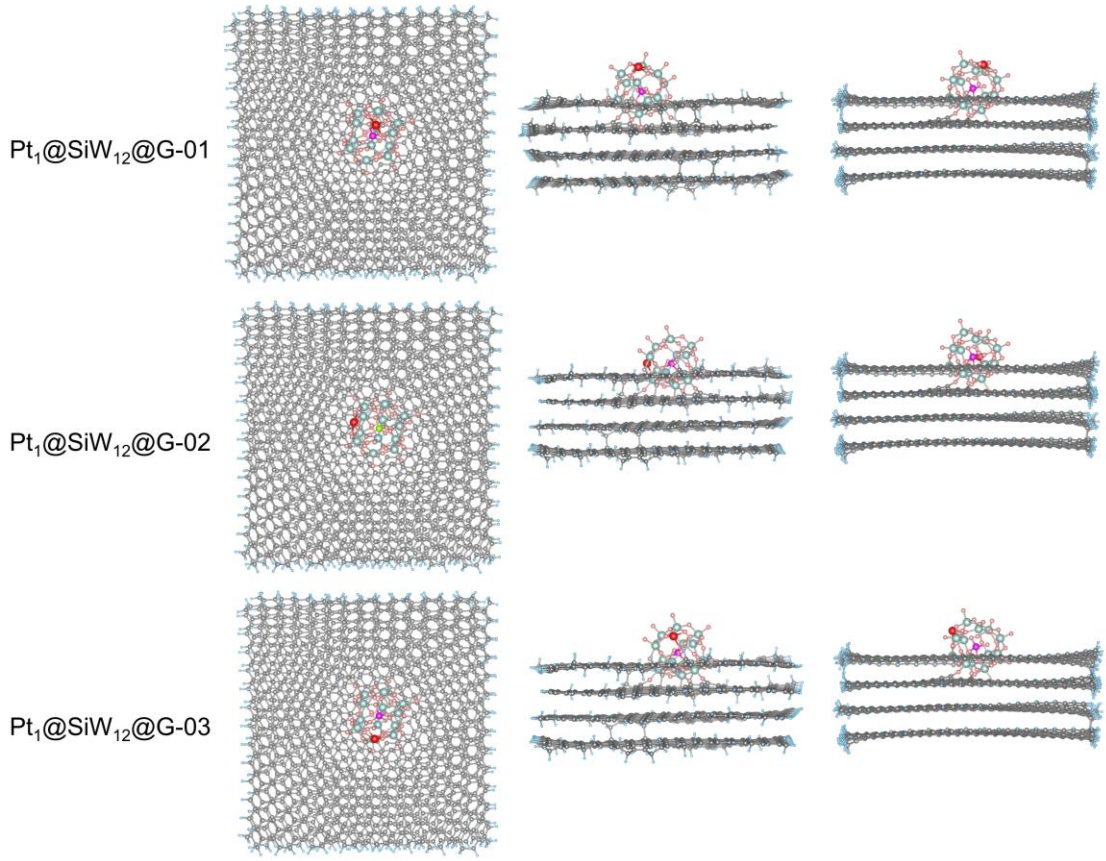

Fig. S8. Optimized structural models showing the top view, front view, and side view of $Pt_1@SiW_{12}@G$-01, $Pt_1@SiW_{12}@G$-02, and $Pt_1@SiW_{12}@G$-03 with the Pt atom anchored at the O4H site.

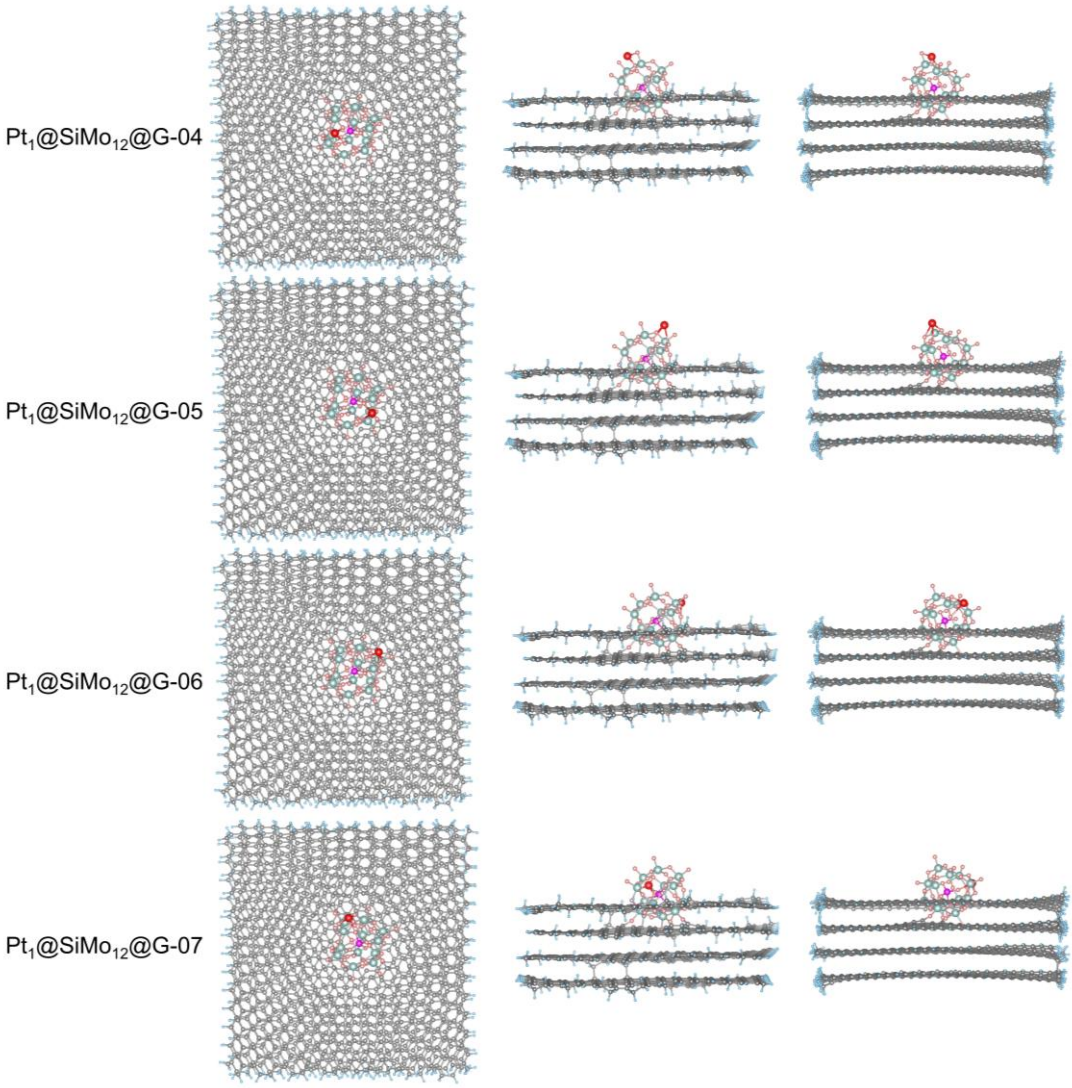

Fig. S9. Optimized structural models showing the top view, front view, and side view of $Pt_1@SiW_{12}@G$-04, $Pt_1@SiW_{12}@G$-05, $Pt_1@SiW_{12}@G$-06, and $Pt_1@SiW_{12}@G$-07 with the Pt atom anchored at the O3H site.

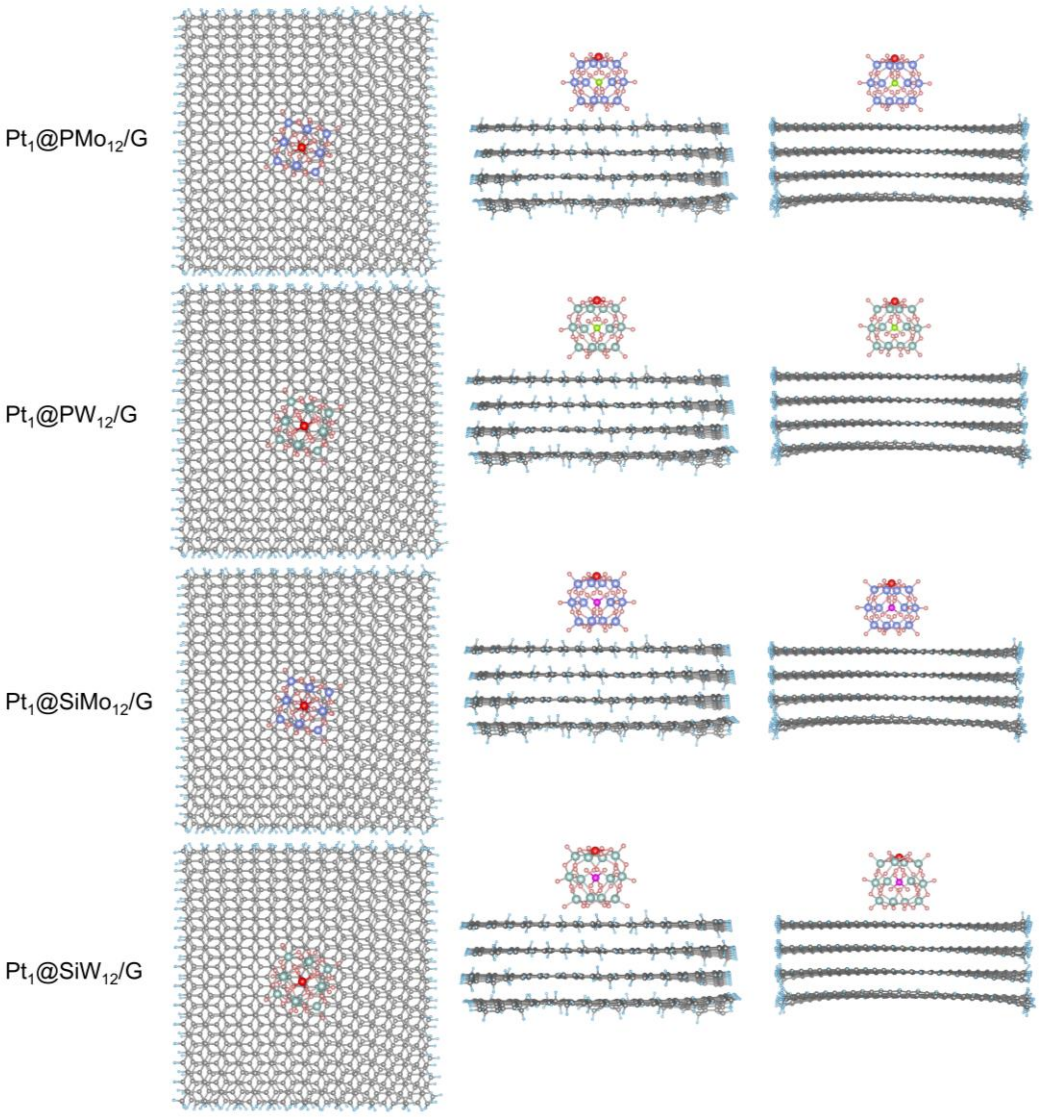

Fig. S10. Optimized structural models showing the top view, front view, and side view of non-confined systems (Pt_1@PMo_{12}/G, Pt_1@PW_{12}/G, Pt_1@$SiMo_{12}$/G, and Pt_1@SiW_{12}/G), with the Pt atom anchored at the O4H site.

Considering that the binding of Pt at the 4H site of POMs in the dual-confined system is more stable, we performed computational modeling on the unconfined system with Pt atoms at the 4H site of POMs/G as a control.

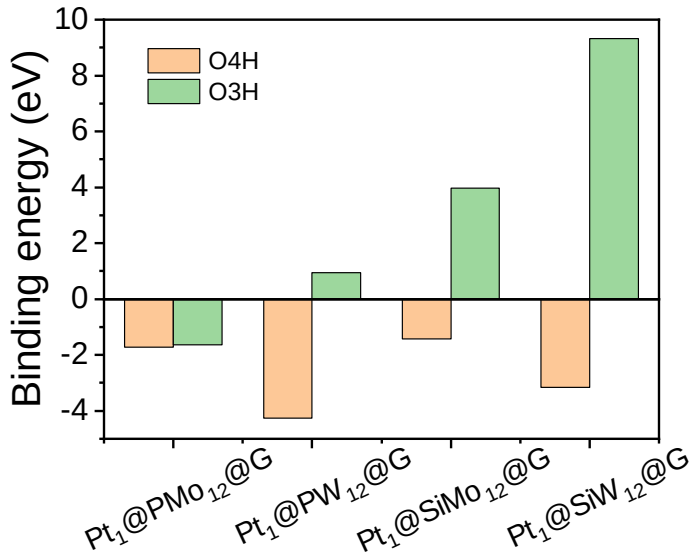

Fig. S11. Binding energies of Pt on O4H or O3H sites exposed on the surface of Pt_1@POMs@G. There are three exposed O4H sites and four O3H sites in the dual-confinement system. So, the binding energy here is an average value.

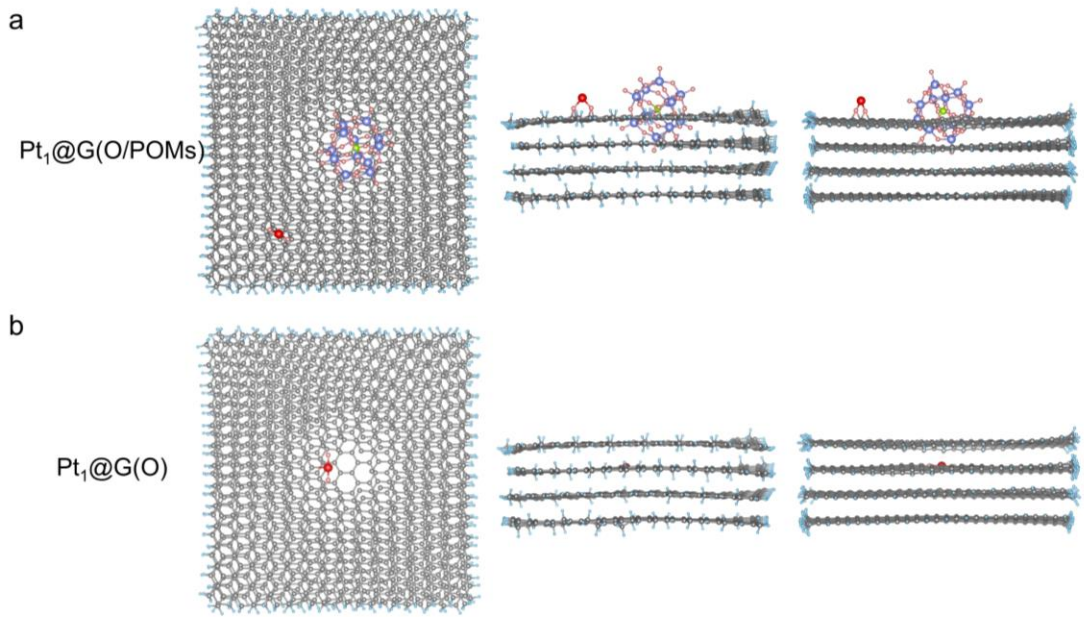

Fig. S12. Optimized structural models showing the top view, front view, and side view of (**a**) Pt_1@G(O/POMs) and (**b**) Pt_1@G(O).

G(O/POMs) represent the PC support containing (confining) POMs. G(O) is the model for PC-containing O, and G is the model for bare PC.

Take PMo_{12} as a prototype, according to the xTB results, the configuration for Pt_1@G(O/POMs) and Pt_1@G(O) can be predicted as in **Fig. S12.**

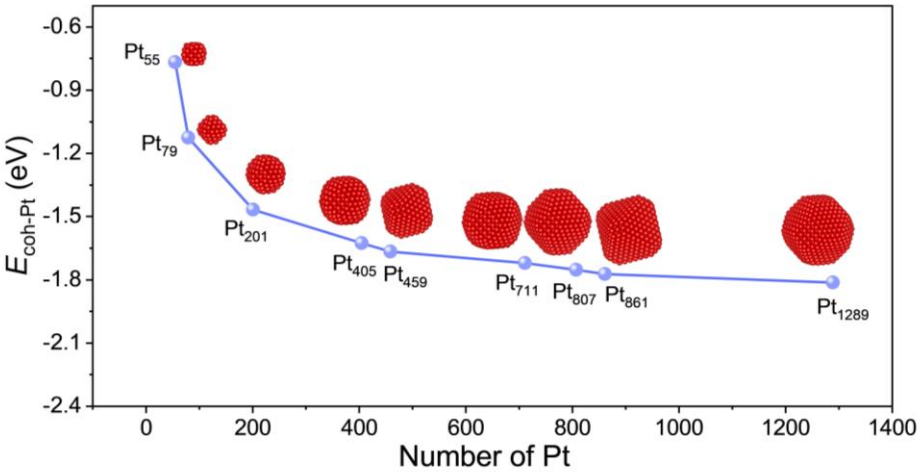

Fig. S13. The cohesive energies per Pt atom (E_{coh-Pt}) for small Pt clusters or large Pt nanoparticles.

If the interaction between Pt and supports is stronger than the cohesive energy of Pt atoms, Pt atoms can generally stay atomically at confined POMs. In contrast, if the binding energy drops below the cohesive energy value of Pt atoms, Pt atoms will agglomerate[11]. The general process of crystal formation involves the formation of crystal nuclei, followed by gradual growth. In **Fig. S13**, the results show that E_{coh-Pt} is -0.77 eV for a smaller cluster (viz. Pt_{55}) in the early growth stage. In comparison, the binding energy between a Pt atom and PW_{12}@G is -2.6 eV, which is more negative than E_{coh-Pt} for Pt_{55} (**Fig. 1b**). This indicates that in the Pt_1@PW_{12}@PC, a single Pt atom is more inclined to be absorbed on PW_{12}@G rather than aggregating into Pt clusters. Although the E_{coh-Pt} converges to -1.81 eV for a larger nanoparticle (viz. Pt_{1289}), the assembly of absorbed Pt single atom into the Pt cluster is inhibited at its early stage. Similarly, Pt_1@PMo_{12}@G, Pt_1@$SiMo_{12}$@G, and Pt_1@SiW_{12}@G, also show more negative binding energies toward Pt atoms (-1.46 eV, -1.30 eV, and -1.47 eV, respectively). Therefore, the Pt atoms tend to be stably loaded on the confined POMs in the Pt_1@POMs@G system rather than self-agglomerate.

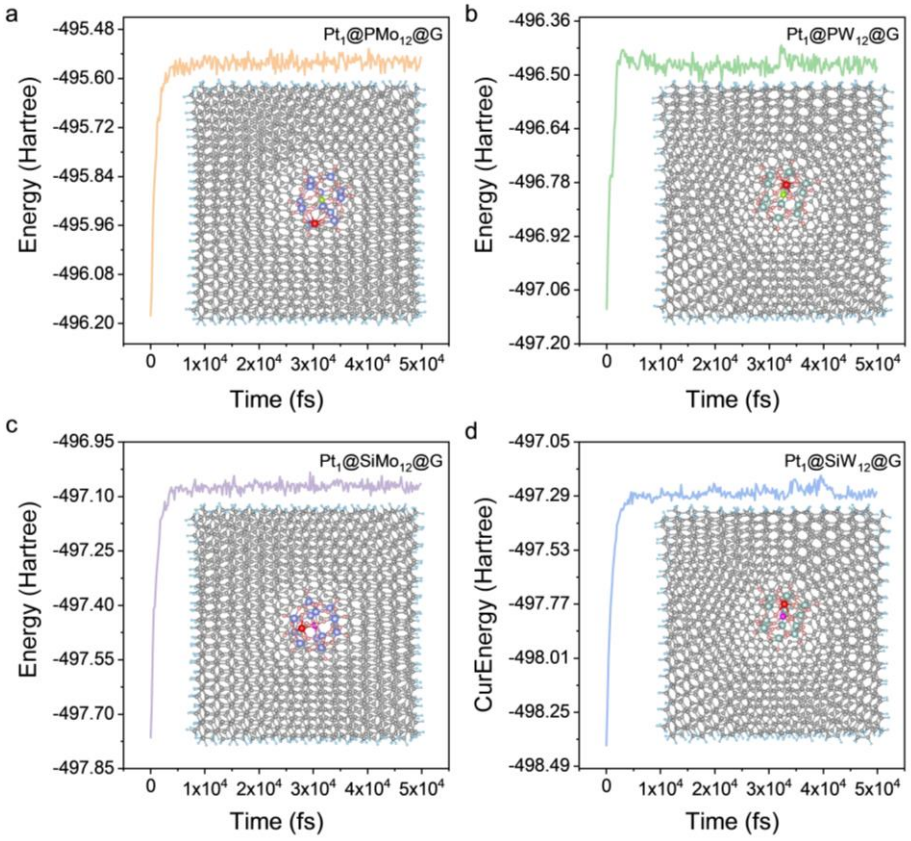

Fig. S14. MD simulation. Total energies of (**a**) $Pt_1@PMo_{12}@G$, (**b**) $Pt_1@PW_{12}@G$, (**c**) $Pt_1@SiMo_{12}@G$, and (**d**) $Pt_1@SiW_{12}@G$ in 50 ps. Inset: last frame structure of $Pt_1@PMo_{12}@G$ in (**a**), $Pt_1@PW_{12}@G$ in (**b**), $Pt_1@SiMo_{12}@G$ in (**c**), and $Pt_1@SiW_{12}@G$-01 in (**d**) after 50 ps MD simulation.

Fig. S14 shows the total energy and final frame of $Pt_1@PMo_{12}@G$, $Pt_1@PW_{12}@G$ $Pt_1@SiMo_{12}@G$, and $Pt_1@SiW_{12}@G$. No significant reconstruction is observed when all systems have reached equilibrium at 298.15 K, suggesting that the absorbed Pt single atom is kinetically stable at room temperature.

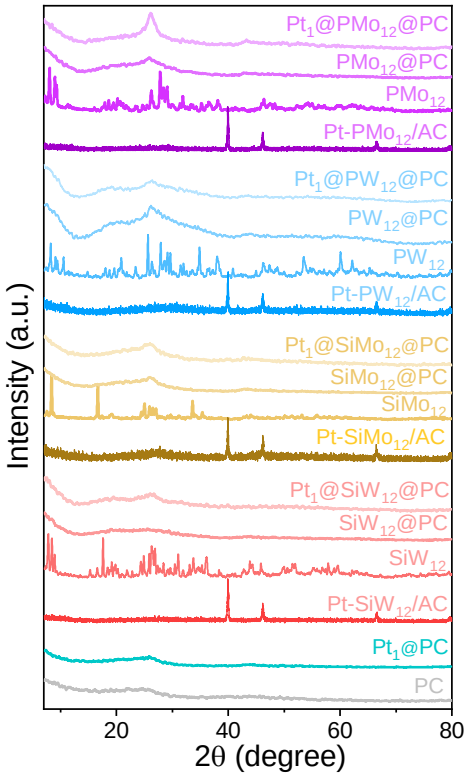

Fig. S15. XRD patterns of PC, Pt_1@PC, POMs (viz. PW_{12}, PMo_{12}, SiW_{12}, $SiMo_{12}$), POMs@PC (viz. PW_{12}@PC, PMo_{12}@PC, SiW_{12}@PC, $SiMo_{12}$@PC), Pt_1@POMs@PC (viz. Pt_1@PW_{12}@PC, Pt_1@PMo_{12}@PC, Pt_1@SiW_{12}@PC, Pt_1@$SiMo_{12}$@PC), and Pt@POMs/AC (viz. Pt@PW_{12}/AC, Pt_1@PMo_{12}/AC, Pt@SiW_{12}/AC, Pt@$SiMo_{12}$/AC).

PC, POMs@PC, and Pt_1@POMs@PC show only similar major reflections with the amorphous phase of graphite at ~ 26° and 44°[12] but no characteristic reflections of Pt NPs and POMs are found.[13] While in the XRD pattern of Pt-POMs/AC, three strong and sharp diffraction peaks at 40º, 47º, and 68º are observed, corresponding to the respective (111), (200), and (220) crystal phases of Pt NPs.

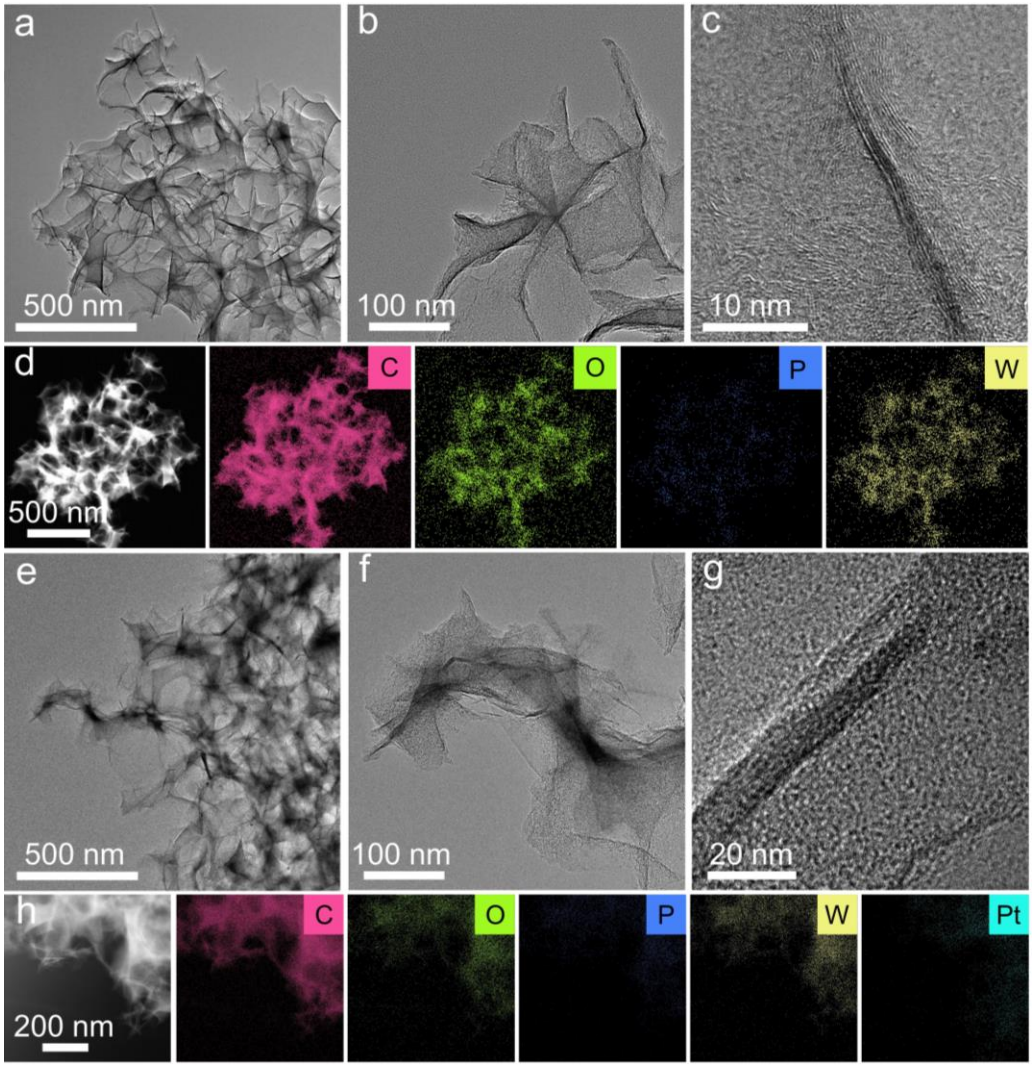

Fig. S16. (**a**−**d**) TEM images of PW_{12}@PC and corresponding EDS mapping images of C, O, P, and W elements. (**e**−**h**) TEM images of Pt_1@PW_{12}@PC and the corresponding EDS mapping images of C, O, P, W, and Pt elements.

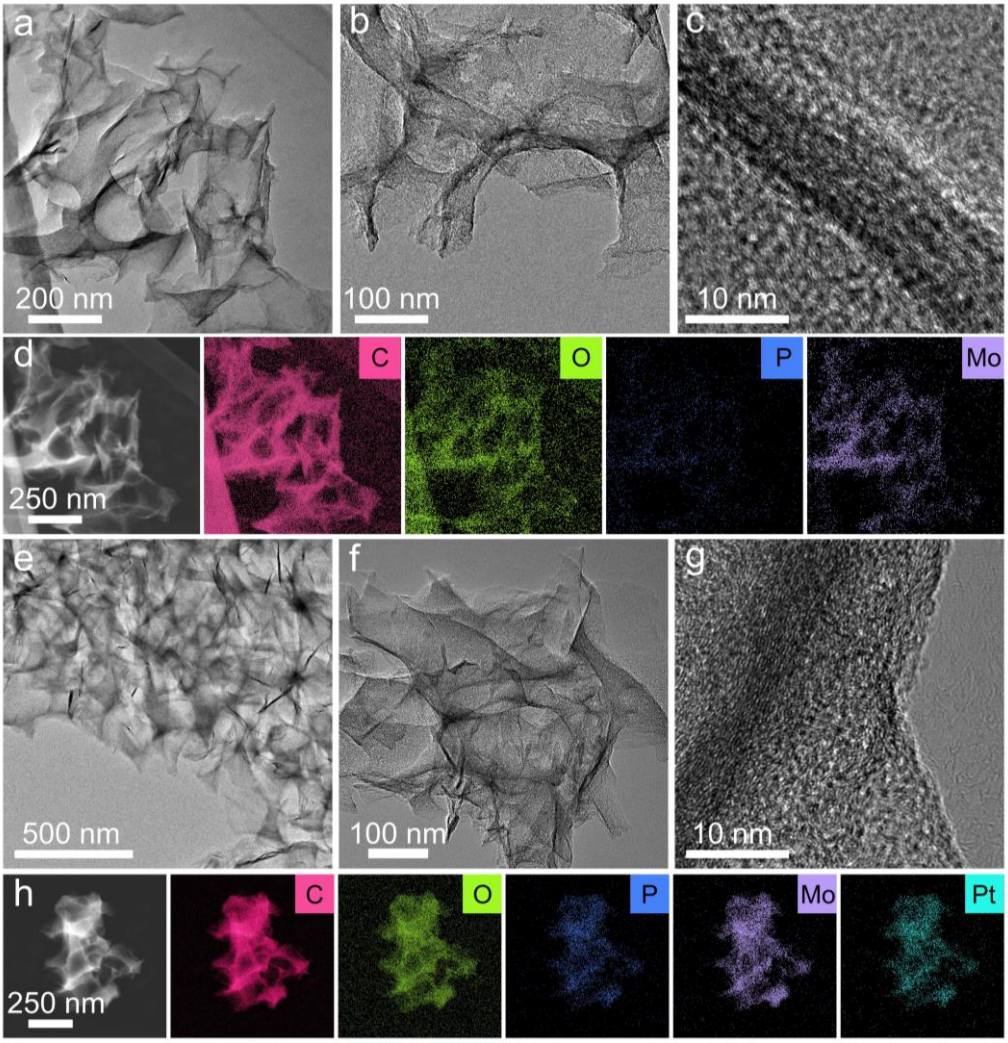

Fig. S17. (**a**−**d**) TEM images of PMo_{12}@PC and corresponding EDS mapping images of C, O, P, and Mo elements. (**e**−**h**) TEM images of Pt_1@PMo_{12}@PC and corresponding EDS mapping images of C, O, P, Mo, and Pt elements.

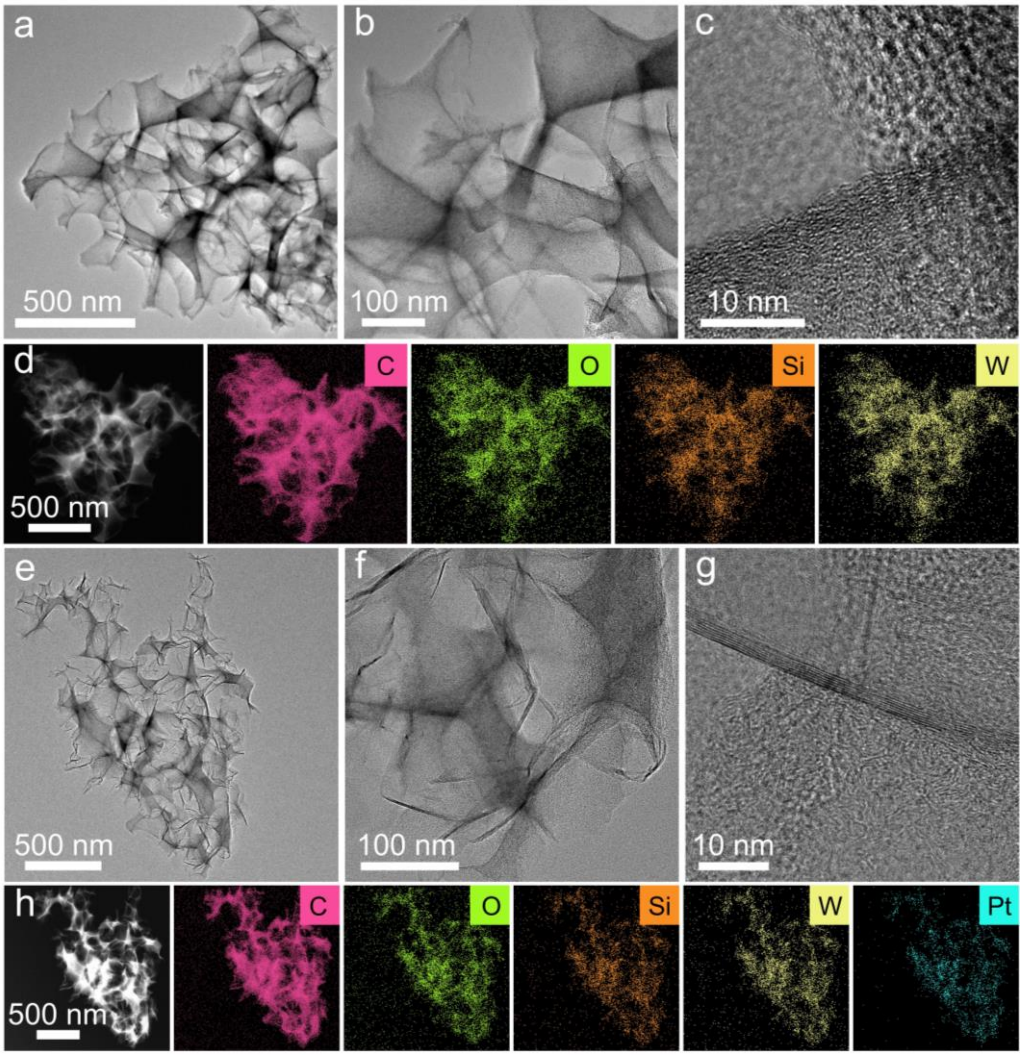

Fig. S18. (**a**−**d**) TEM images of SiW_{12}@PC and corresponding EDS mapping images of C, O, Si, and W elements. (**e**−**h**) TEM images of Pt_1@SiW_{12}@PC and corresponding EDS mapping images of C, O, Si, W, and Pt elements.

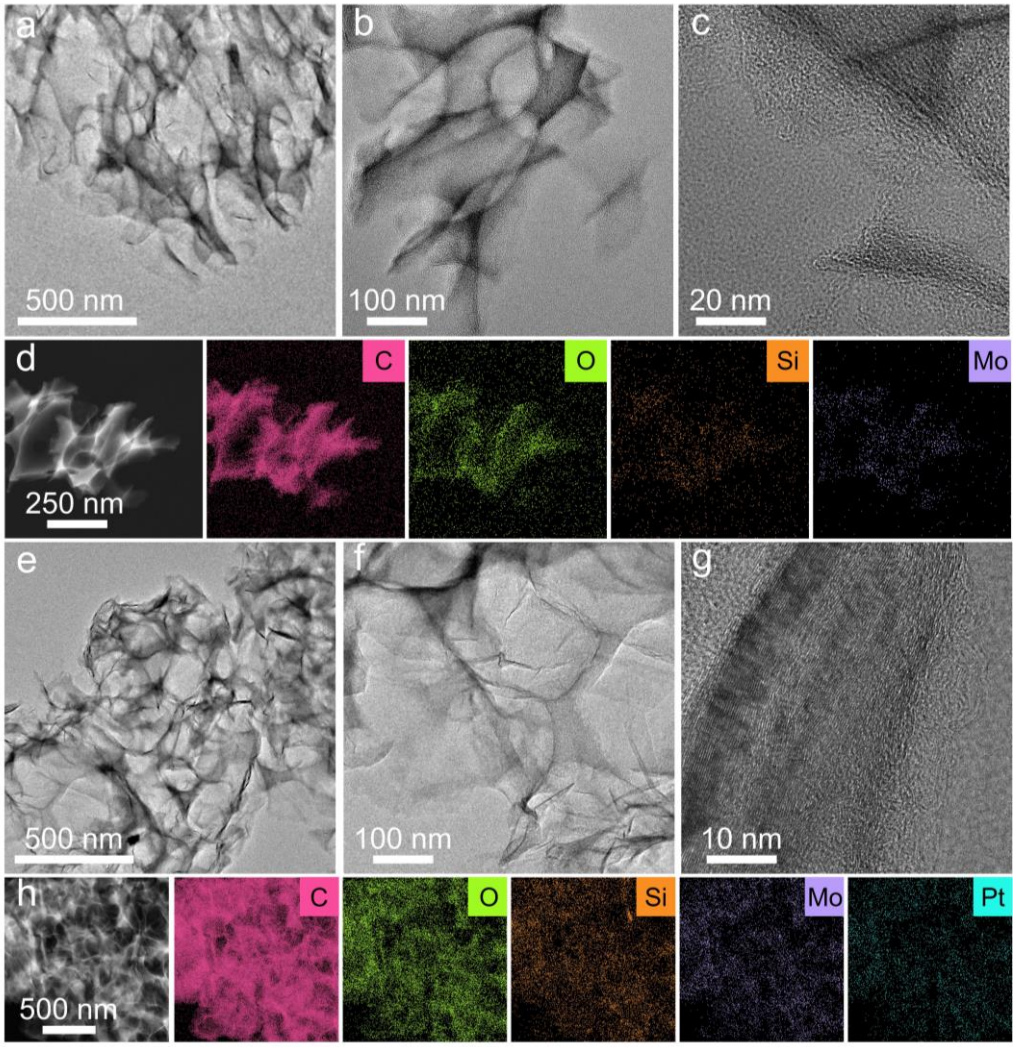

Fig. S19. (**a**−**d**) TEM images of $SiMo_{12}$@PC and corresponding EDS mapping images of C, O, Si, and Mo elements. (**e**−**h**) TEM images of Pt_1@$SiMo_{12}$@PC and corresponding EDS mapping images of C, O, Si, Mo, and Pt elements.

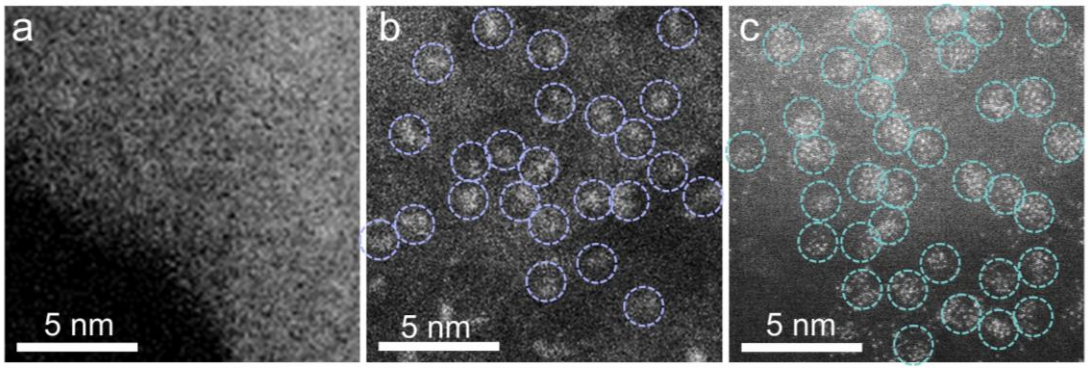

Fig. S20. HAADF-STEM images of (**a**) PC, (**b**) PMo_{12}@PC, and (**c**) PW_{12}@PC.

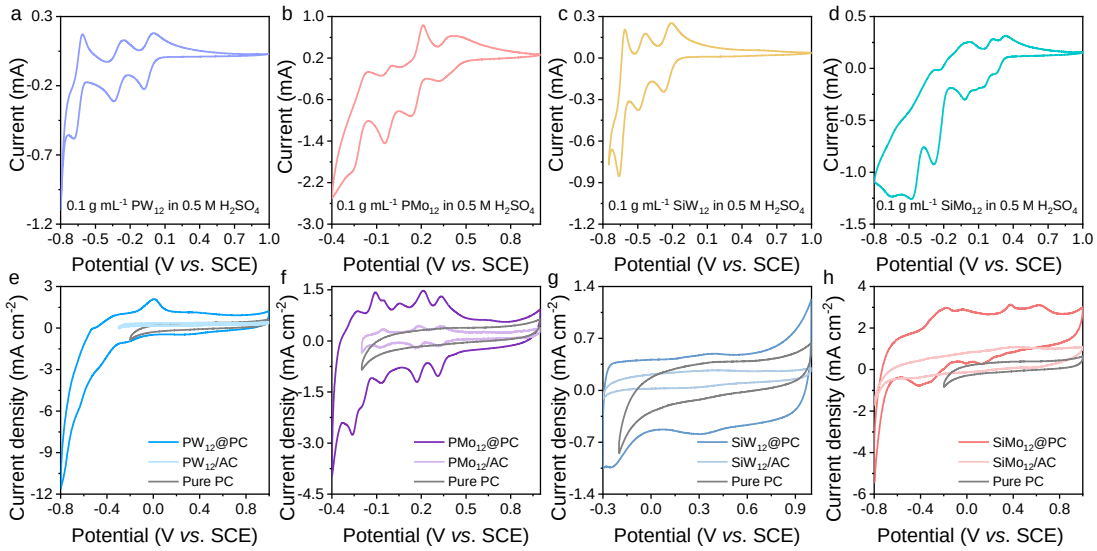

Fig. S21. CV curves of (**a**) pure PW_{12} solution, (**b**) pure PMo_{12} solution, (**c**) pure SiW_{12} solution, and (**d**) pure $SiMo_{12}$ solution in 0.5 M H_2SO_4 at 40 mV s^{-1}. (**e**–**h**) CV curves of PC, POMs/AC, and POMs@PC in 0.5 M H_2SO_4 at 40 mV s^{-1}.

Note that the concentration of pure PMo_{12} here is ~ 53-fold of that (1 mM) confined in PC, because that the redox peaks of 1 mM pure POMs solutions in 0.5 M H_2SO_4 are difficult to be detected. As shown in **Fig. S21**, the redox peaks of POMs are essentially invisible in conventional unconfined materials (POMs/AC). On the contrary, several pairs of successive reversible redox peaks of POMs are stimulated in POMs@PC due to the confinement of isolated POMs in PC. So, the monodisperse state of POMs in POMs@PC is also confirmed by the presence of multiple-intrinsic redox peaks induced by the precise confinement, which are invisible in conventional POMs/AC.

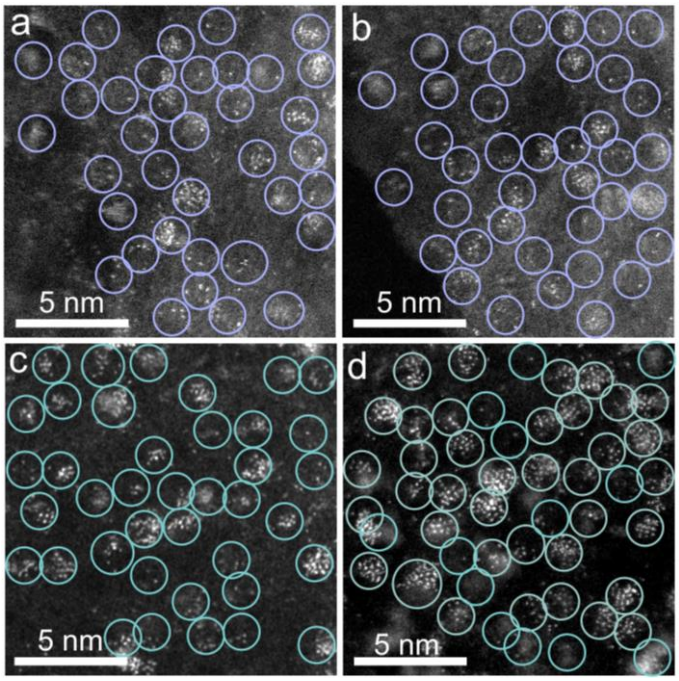

Fig. S22. HAADF-STEM images of (**a**) Pt_1@PMo_{12}@PC and (**b**) Pt_1@PW_{12}@PC.

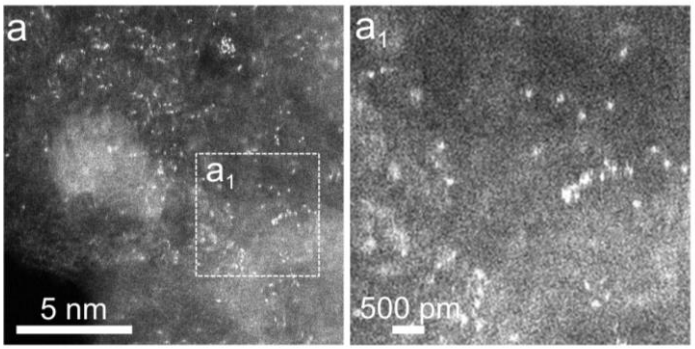

Fig. S23. HAADF-STEM image of Pt_1@PC. Enlarged HAADF-STEM image of the square region in a_1.

Considering the suitable pore size of PC, the free $[PtCl_6]^{2-}$ ions (~ 0.5 nm)[13] can also be captured by pure PC via the Pt–O coordination effect, as bright dots being identified as Pt atoms in Pt_1@PC.

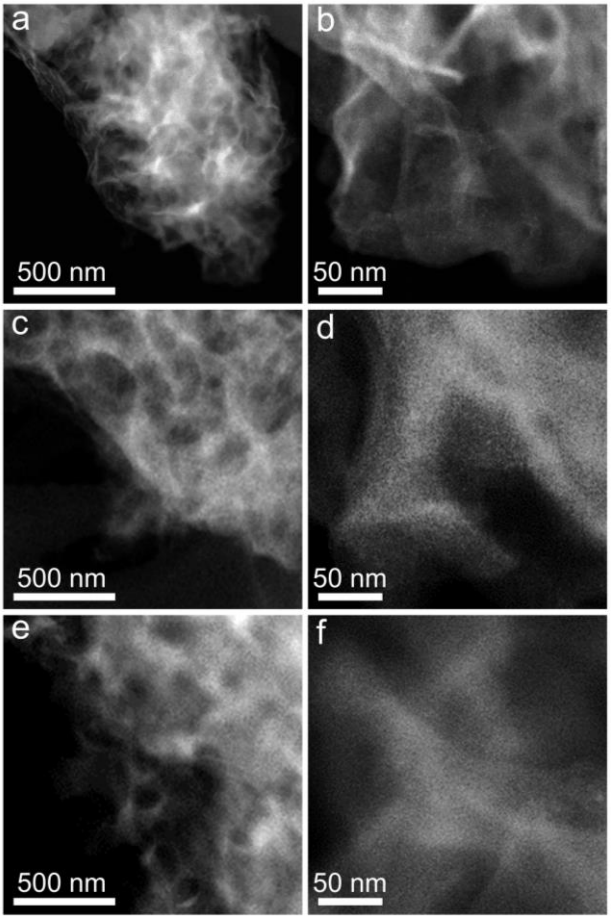

Fig. S24. HAADF-STEM images of (**a**), (**b**) Pt_1@PMo_{12}@PC, (**c**), (**d**) Pt_1@PW_{12}@PC, and (**e**), (**f**) Pt_1@PC.

Sub-angstrom resolution HAADF-STEM images show that the morphology of PC is well preserved with maintained silk-like interconnected frameworks after POMs and Pt loading with no nanoparticles or clusters found at low magnification.

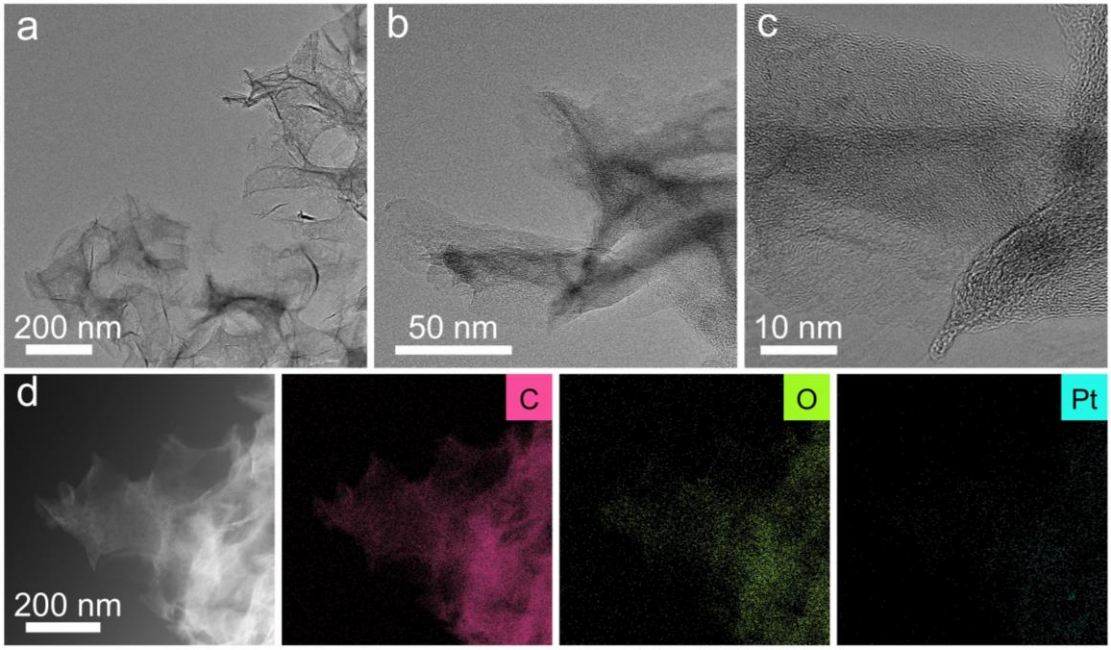

Fig. S25. TEM images of Pt_1@PC and corresponding EDS mapping images of C, O, and Pt elements.

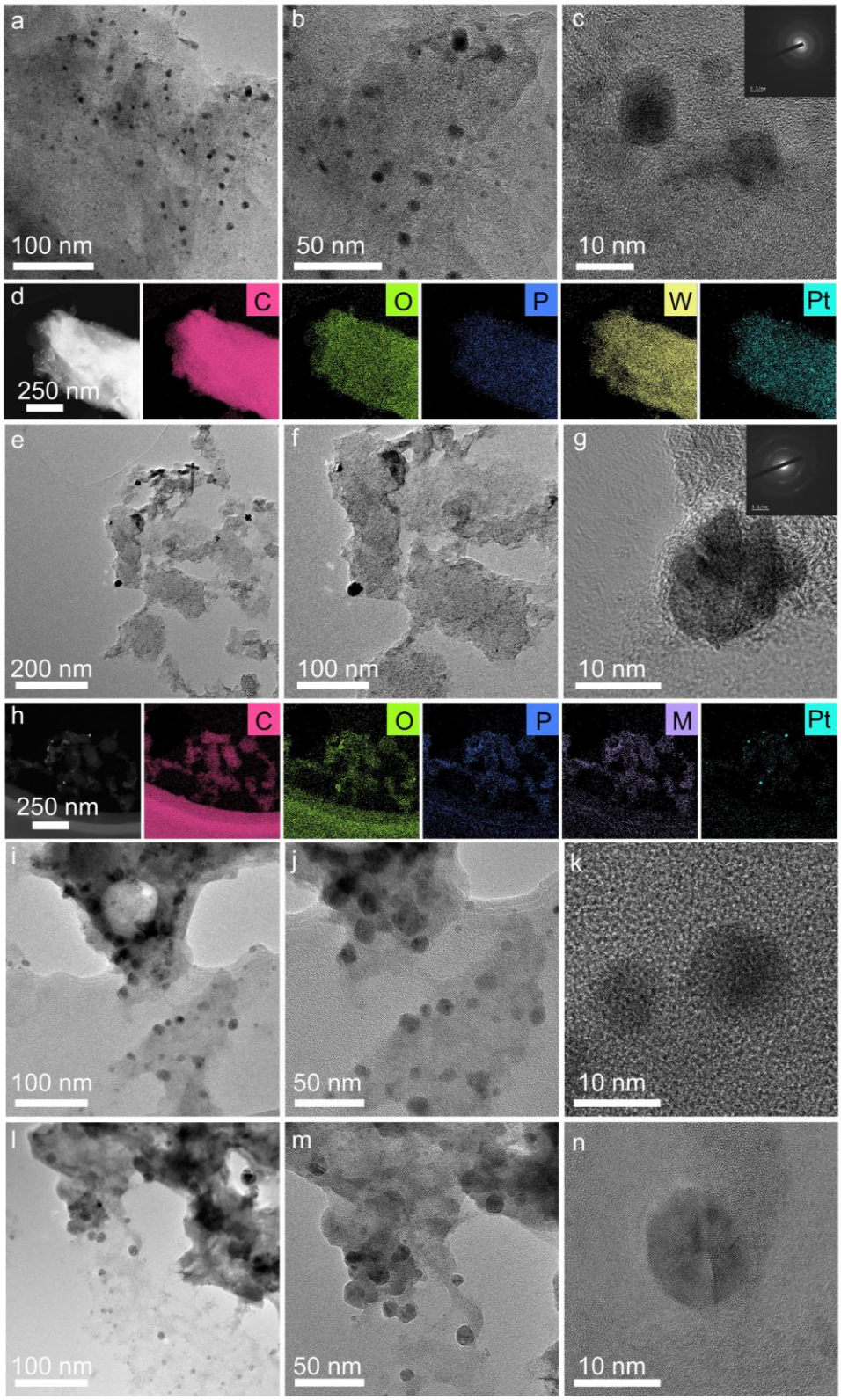

Fig. S26. (**a**–**d**) TEM images of Pt-PW_{12}/AC and corresponding EDS mapping images of C, O, P, W, and Pt elements. (**e**–**h**) TEM images of Pt-PMo_{12}/AC and corresponding EDS mapping images of C, O, P, Mo, and Pt elements. TEM images of (**i**–**k**) Pt-SiW_{12}/AC and (**l**–**n**) Pt-$SiMo_{12}$/AC.

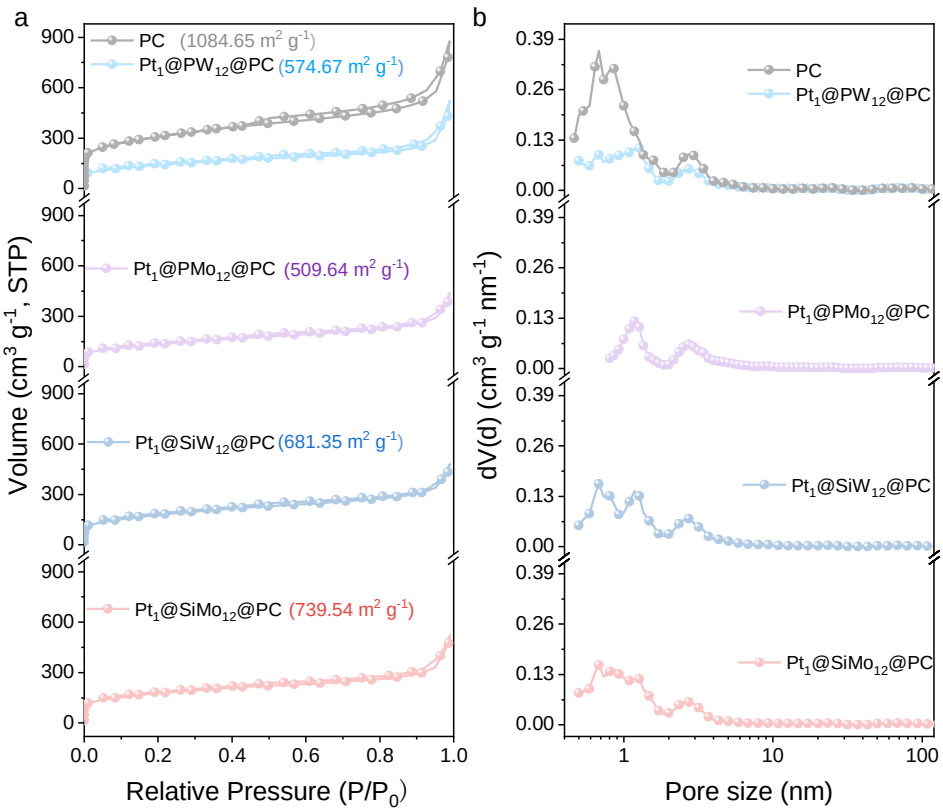

Fig. S27. (**a**) N_2 sorption isotherms. (**b**) Pore size distributions calculated by non-local density functional theory (NLDFT).

The nitrogen adsorption isotherms of Pt_1@POMs@PC were recorded at 77 K. In **Fig. S27a**, all samples exhibit reversible type II form, presumably attributing to the presence of a large number of super-micropores in these samples. The N_2 uptake capacity at saturation was reduced significantly after the confinement of POMs Pt and atoms into the pores of PC. Correspondingly, the pore size distributions are also in agreement with these results (**Fig. S27b**).

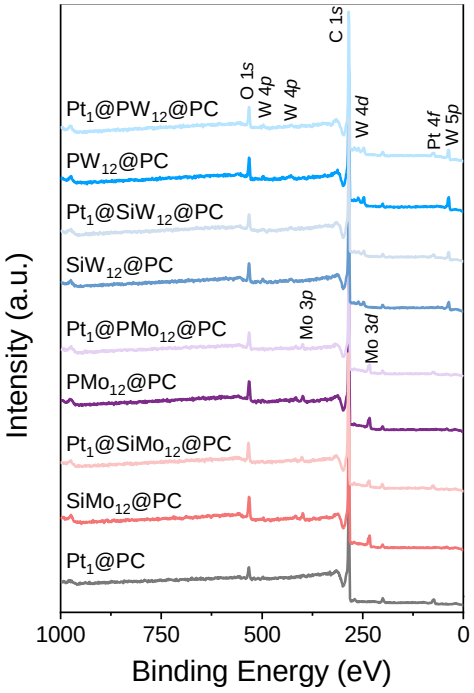

Fig. S28. XPS survey spectra of Pt_1@PC and Pt_1@POMs@PC.

XPS mapping allows qualitative analysis of the chemical valence state and electronic structure of elements to infer the interactions between substances. **Fig. S28** exhibits the full XPS survey of Pt_1@PC, POMs@PC, Pt_1@POMs@PC, which verifies the presence of main elements such as Pt, Mo, W, C, and O.[14, 15]

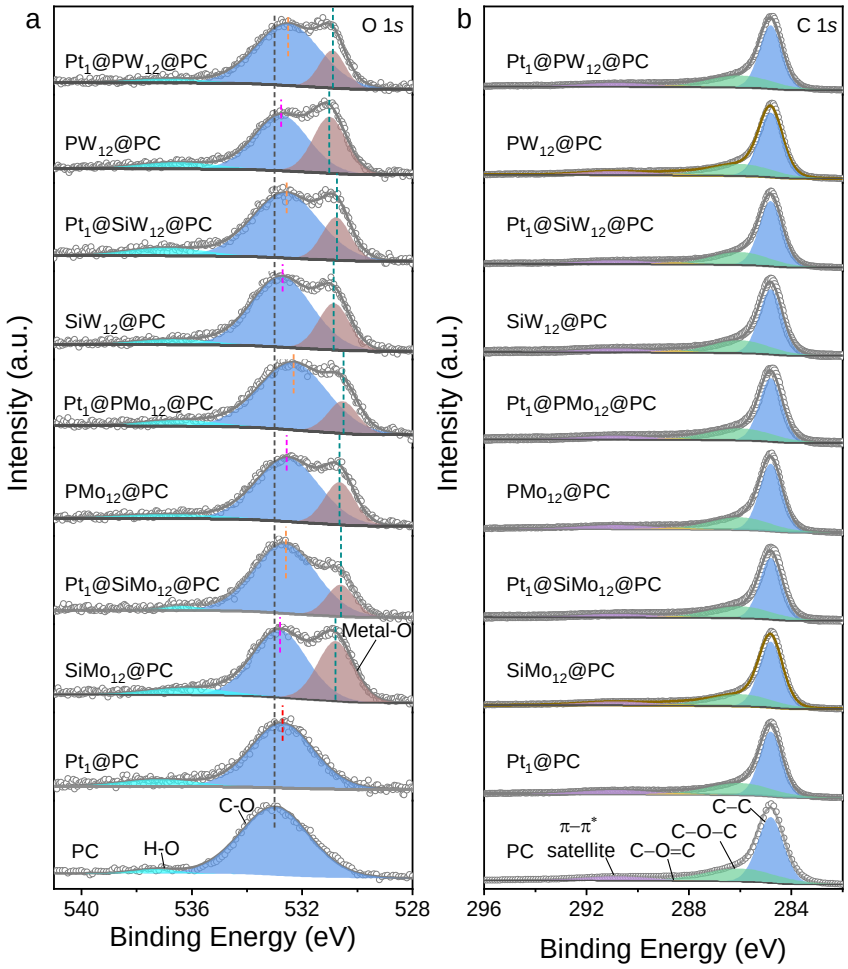

Fig. S29. The high-resolution XPS spectra of Pt_1@PC and Pt_1@POMs@PC in (**a**) O 1*s* and (**b**) C 1*s* regions.

A negative shift of C–O for POMs@PC and Pt_1@POMs@PC compared with the PC (533.097 eV) also verifies electron transfer between PC, POMs, and Pt. Note that the peak at about 539.5~531.0 is ascribed to W/Mo–O–W/Mo and W/Mo=O of POMs.[13] The peak at about 536–537 eV for all samples is assigned to the presence of the hydroxyl (O–H), which may be ascribed to the presence of hydrogen protons connected to oxygen atoms and the crystal H_2O adsorbed throughout the POM molecule.[14] The XPS spectra of C 1*s* is shown in **Fig. S29b**, the peak at 284.8 eV, 286 eV, 288.5 eV, and 290.8 eV can be ascribed to C–C, C–O–C, O–C=O, and π–π* transitions of aromatic C–C, respectively. Simultaneously, the C 1*s* for all control samples are also similar, thus the structural uniformity of the PC matrix is maintained regardless of the incorporation of POMs or H_2PtCl_6. That the metal–C bond (283 eV) is not obvious, which indicating the absence of the Pt–C bond for all samples.

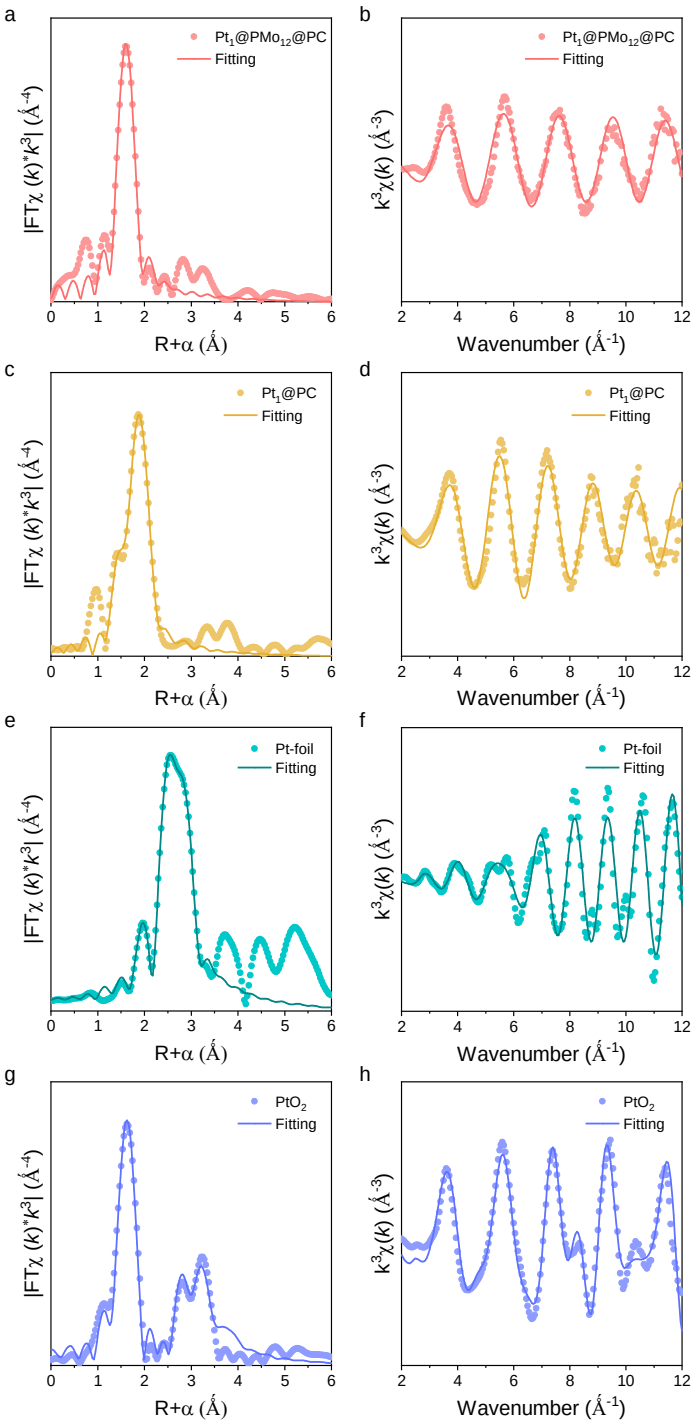

Fig. S30. EXAFS fitting curves of Pt_1@PMo_{12}@PC, Pt_1@PC, Pt-foil, and PtO_2 at Pt *L*3-edge of (**a**), (**c**), (**e**), (**g**) *R*-space and (**b**), (**d**), (**f**), (**h**) *k*-space, respectively.

a

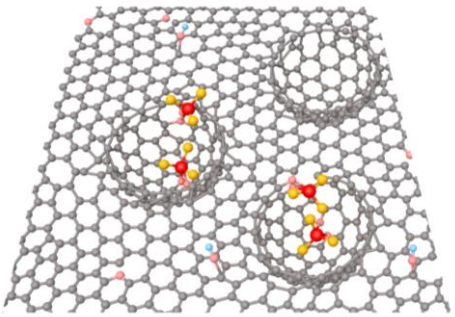

Pt_1@PC

b

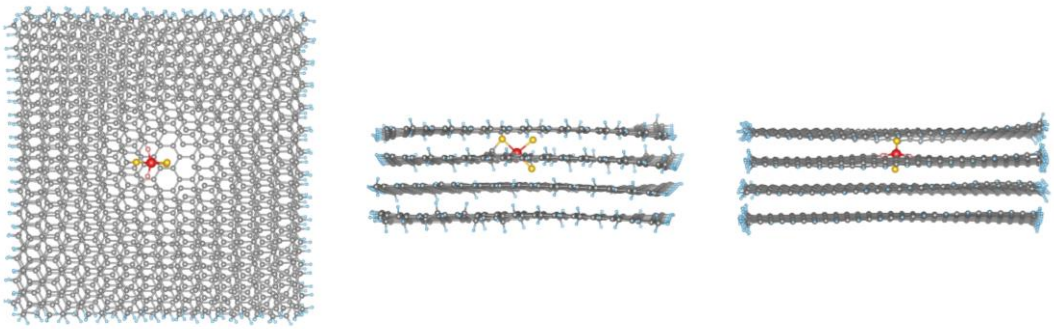

Fig. S31. (**a**) Schematic illustration of Pt_1@PC. (**b**) Optimized structural models showing the top view, front view, and side view of $PtCl_3$-O_2@G.

Pt−O (2.058 Å) and Pt−Cl (2.322 Å) with a coordination number of two and three, respectively, are shown in Pt_1@PC, suggesting that the actual configuration of Pt_1@PC is $PtCl_3$-O_2@PC. It is apparent that Cl is not completely cleaved from the precursor, which may be toxic to Pt atoms. The actual configuration of Pt_1@PC is shown in **Fig. S31a**, which is expressed as $PtCl_3$-O_2@G. Note that xTB analysis displays a strong binding energy (-2.74 eV) between $PtCl_3$ and O_2@PC, which is detrimental to the exposure of the Pt active site (**Fig. S31b**).

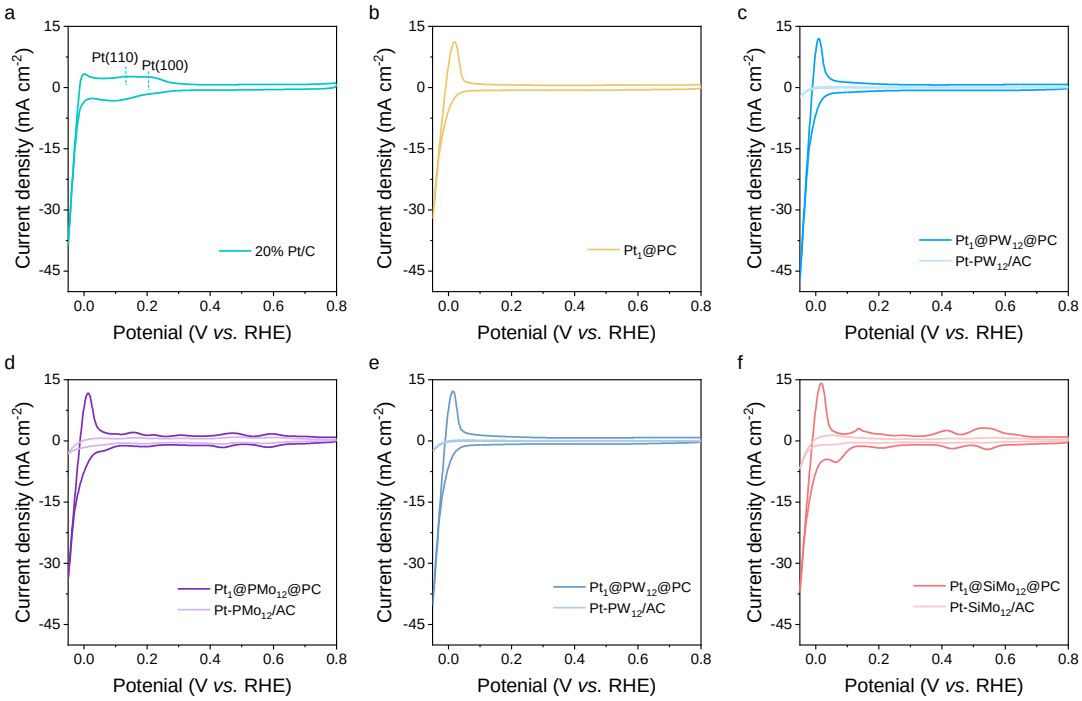

Fig. S32. CV curves of (**a**) 20% Pt/C, (**b**) Pt_1@PC, (**c**)−(**f**) Pt-POMs/AC and Pt_1@POMs@PC in 0.5 M H_2SO_4 at 40 mV s^{-1}.

The hydrogen desorption peak of Pt(100) and Pt(110) of 20% Pt/C is absent in CV curves of Pt_1@POMs@PC and Pt_1@PC in 0.5 M H_2SO_4, indicating the atomic state distribution of Pt element in Pt_1@POMs@PC and Pt_1@PC (**Fig. S32**).[16] Moreover, the more obvious hydrogen desorption peak of Pt SAs for Pt_1@POMs@PC than that in Pt-POMs/AC suggests that more absorbed hydrogen would be generated on the catalyst surface, which is conducive to the hydrogen spillover.

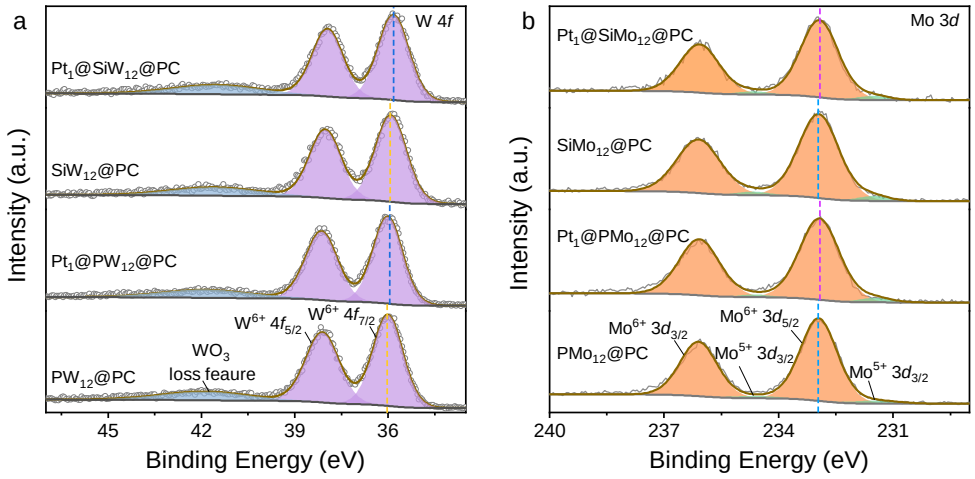

Fig. S33. The high-resolution XPS spectra of (**a**) W 4*f* and (**b**) Mo 3*d*.

Compared with POMs@PC, negatively shifted W^{6+} 4*f* and Mo^{6+} 3*d* peaks of Pt_1@POMs@PC[17] reveals the accumulated electrons on W/Mo atoms.

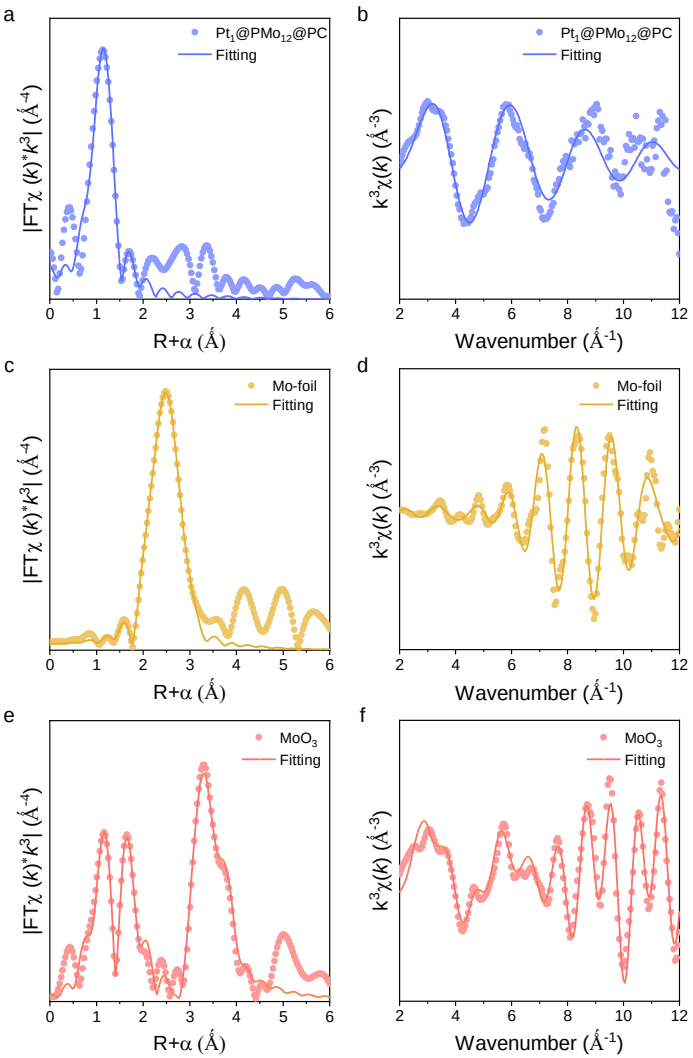

Fig. S34. EXAFS fitting curves of Pt_1@PMo_{12}@PC, Mo-foil, and MoO_3 at Mo *K*-edge of (**a**), (**c**), (**e**) *R*-space and (**b**), (**d**), (**f**) *k*-space, respectively.

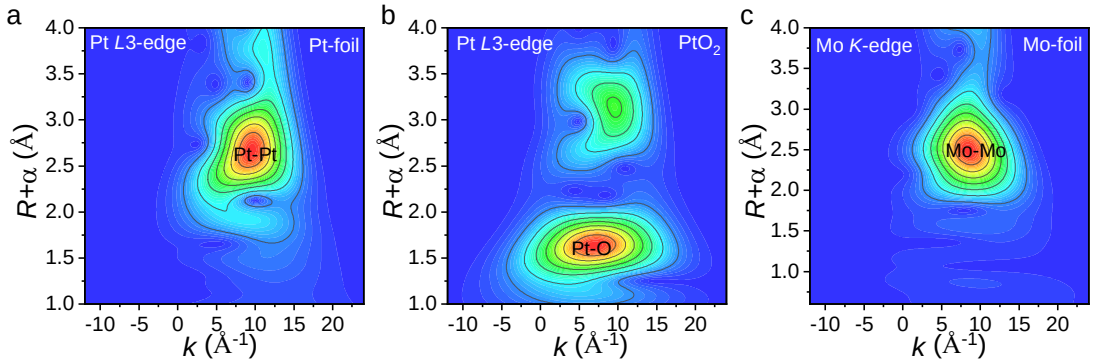

Fig. S35. Wavelet-transform images of (**a**) Pt-foil and (**b**) PtO_2 at Pt *L*3-edge and (**c**) Mo-foil at Mo *K*-edge.

For Wavelet Transform analysis, the χ(k) exported from Athena is imported into the Hama Fortran code. The parameters are listed as follow: R range, Pt: 1-4 Å, Mo: 0.6-4 Å; *k* range, 0-12.0 $Å^{-1}$; *k* weight, 3; and Morlet function with κ=15, σ=1 is used as the mother wavelet to provide the overall distribution.

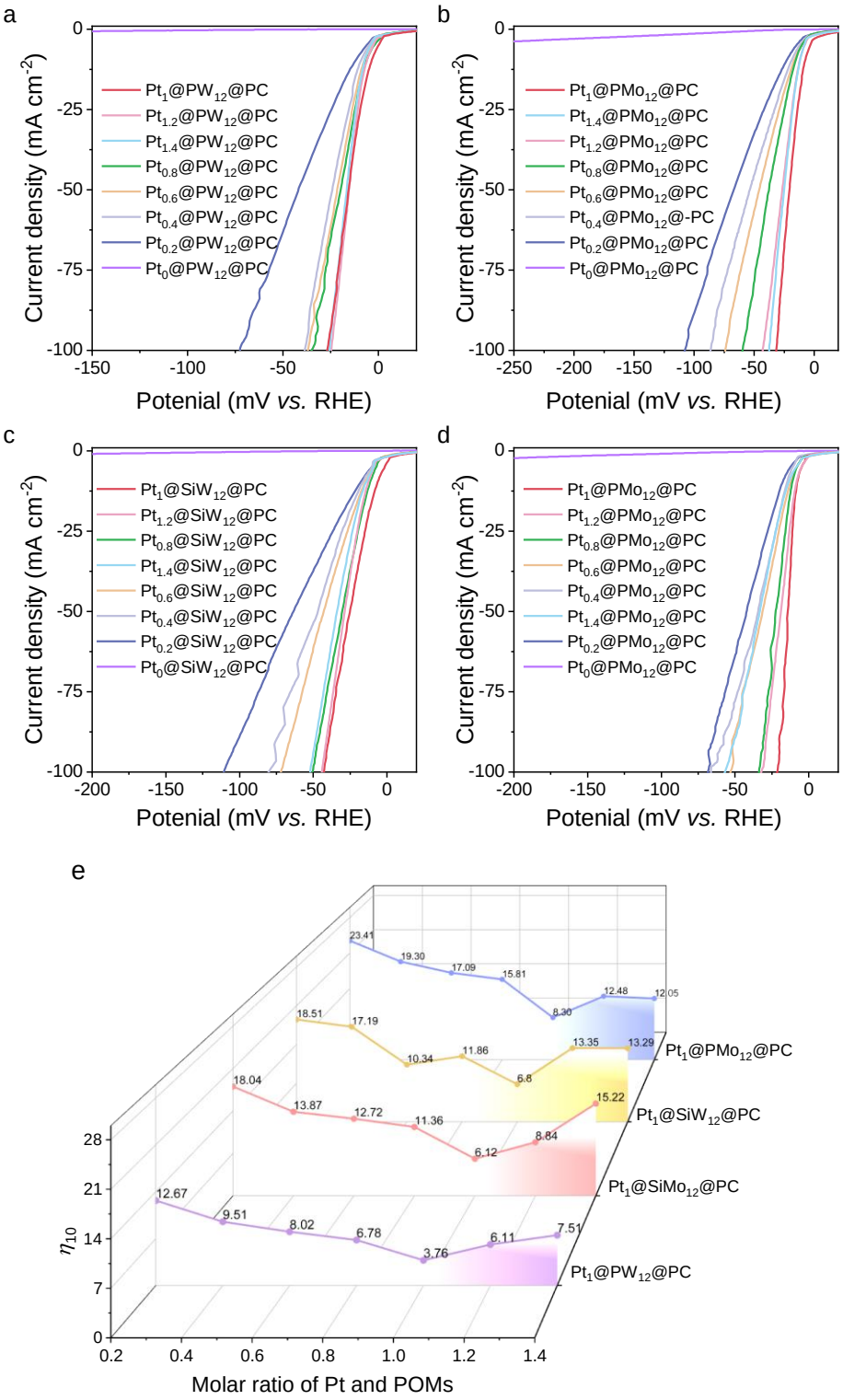

Fig. S36. (**a**–**d**) LSV curves of the Pt$_x$@POMs@PC in 0.5 M H_2SO_4 solution at 40 mV s^{-1} (*x* represents the molar ratio of Pt and POMs). (**e**) The overpotentials at 10 mA cm^{-2} of Pt$_x$@POMs@PC.

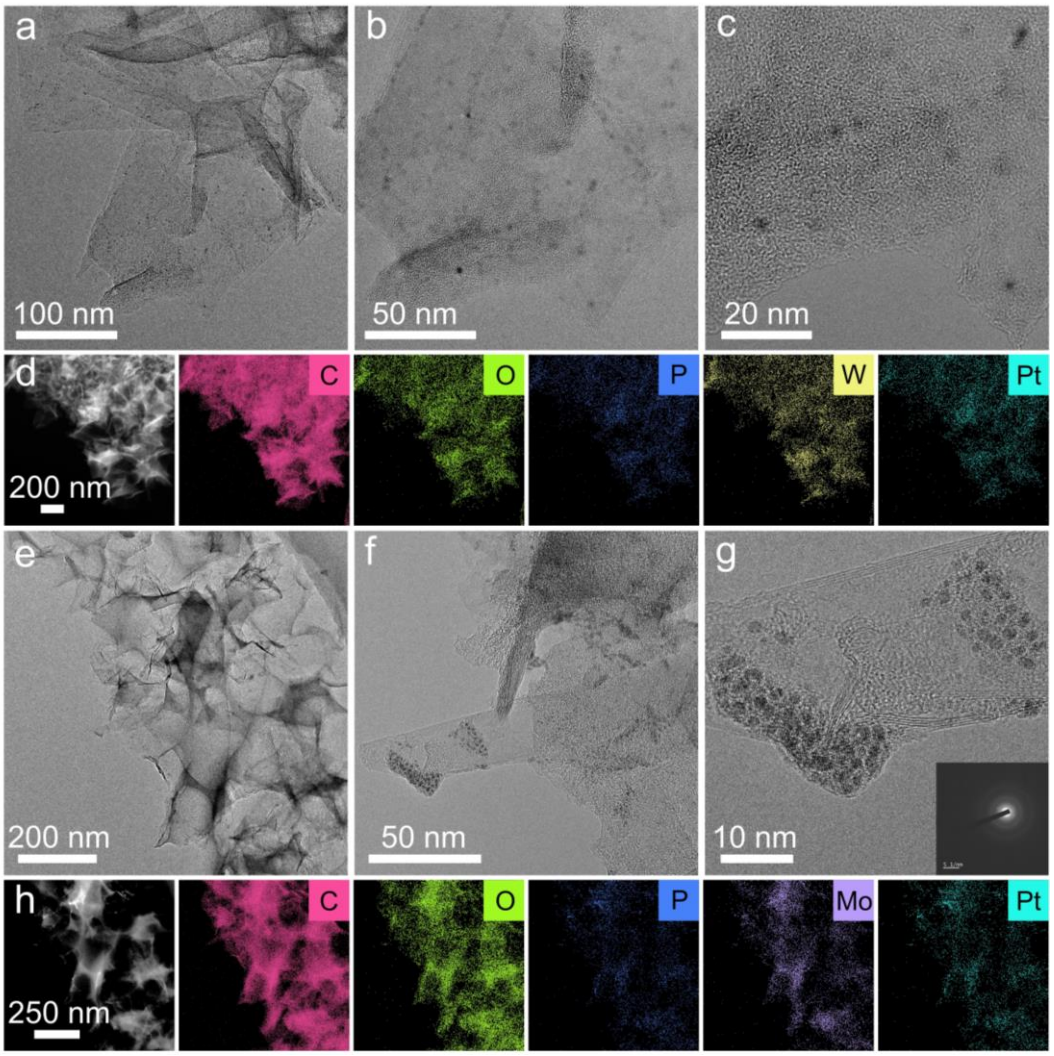

Fig. S37. (**a**–**d**) TEM images of $Pt_{1.4}$@PW_{12}@PC and corresponding EDS mapping images of C, O, P, W, and Pt elements. (**e**–**h**) TEM images of $Pt_{1.4}$@PMo_{12}@PC and corresponding EDS mapping images of C, O, P, Mo, and Pt elements.

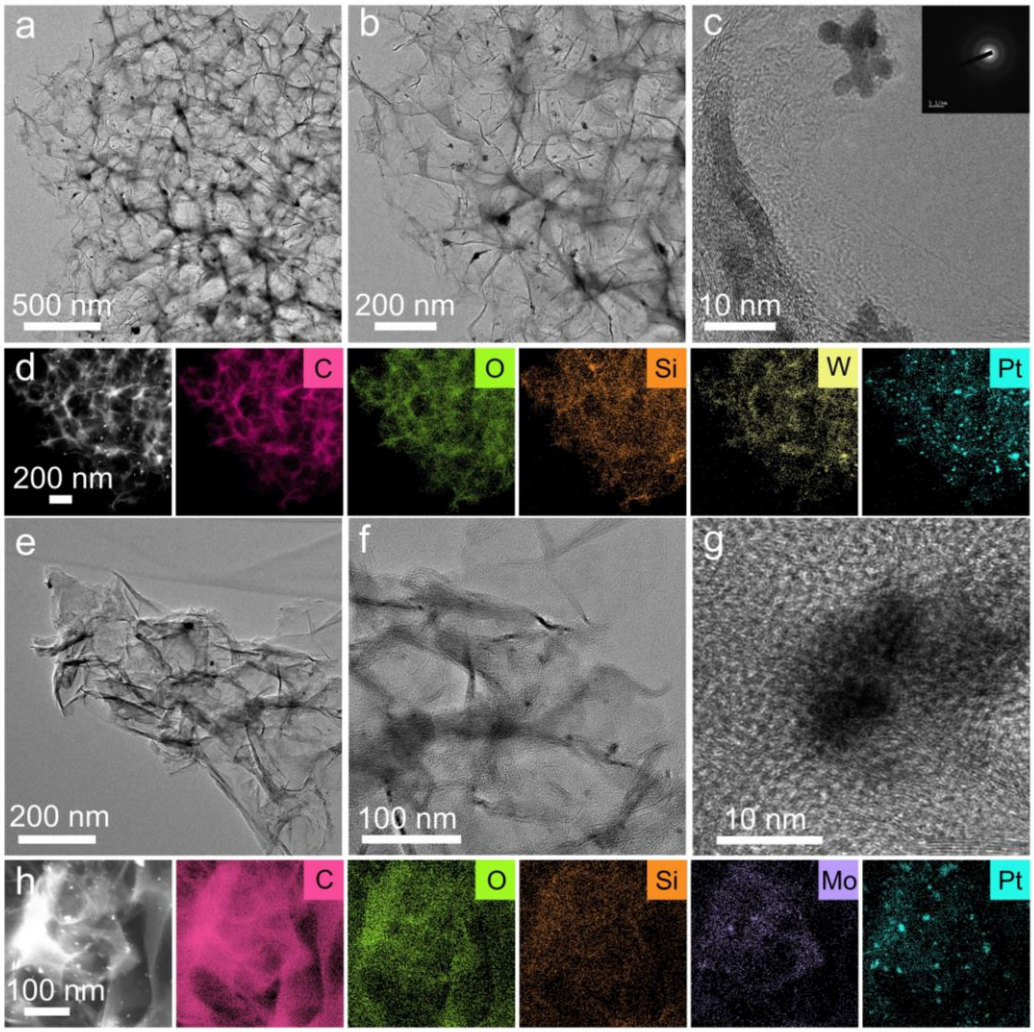

Fig. S38. (**a**–**d**) TEM images of $Pt_{1.4}$@SiW_{12}@PC and corresponding EDS mapping images of C, O, Si, W, and Pt elements. (**e**–**h**) TEM images of $Pt_{1.4}$@$SiMo_{12}$@PC and corresponding EDS mapping images of C, O, Si, Mo, and Pt elements.

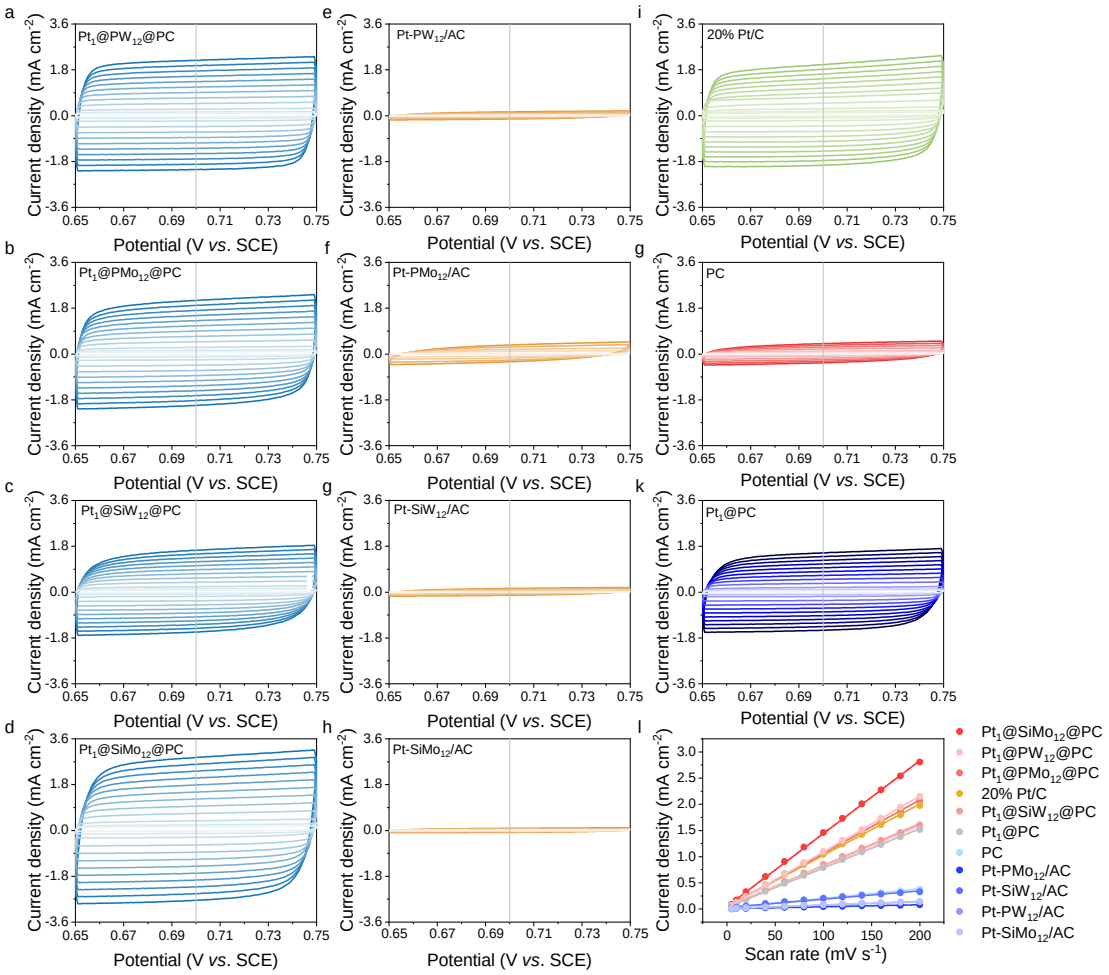

Fig. S39. (**a**)−(**k**) Cyclic voltammetry curves in the region of 0.65−0.75 V (*vs*. SCE) of samples with different scan rates from 5 to 200 mV s^{-1} in 0.5 M H_2SO_4. (**l**) Calculated capacitive currents at 0.7 V (*vs*. SCE) as a function of scan rates.

The geometric current density (*j*) normalized by electrochemical active surface area (ECSA; j_{ECSA}), as determined by deriving the electrochemical double-layer capacitance, (C_{dl},) was applied to identify the intrinsic activity of Pt_1@POMs@PC. The C_{dl} values and ECSA values were measured, as shown in **Table S5.** The ECSA corresponding to the dual-confinement system is larger than that of Pt_1@PC, which may be due to the improved electron transfer driven by confined POMs.

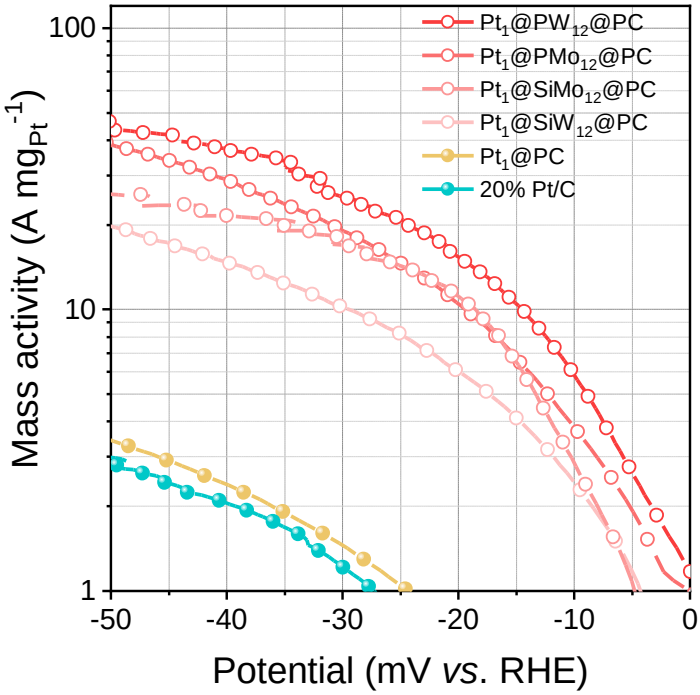

Fig. S40. Mass activity values of Pt_1@POMs@PC, Pt_1@PC, and 20% Pt/C in 0.5 M H_2SO_4.

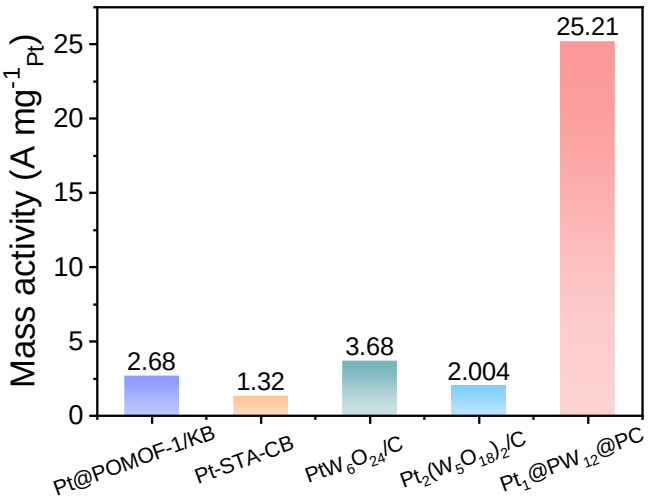

Fig. S41. Comparison of mass activity at η_{30} for Pt/POMs-contained composite catalysts in HER.

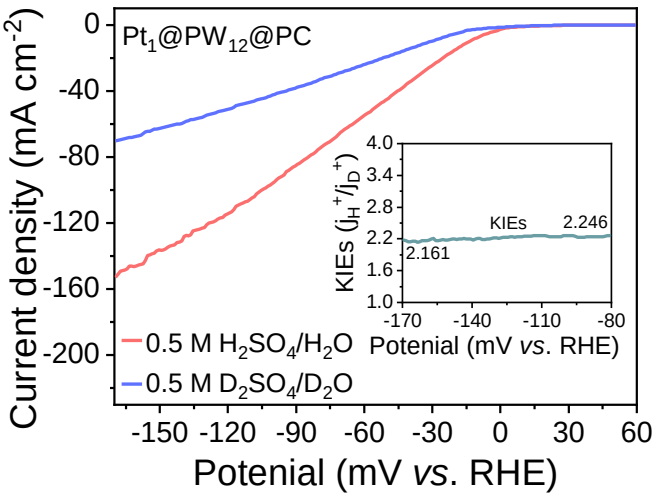

Fig. S42. Polarization curves of $Pt_1@PW_{12}@PC$ catalyst in aqueous 0.5 M H_2SO_4 and 0.5 M D_2SO_4 solutions. The inset is the kinetic isotope effect value *vs*. potential.

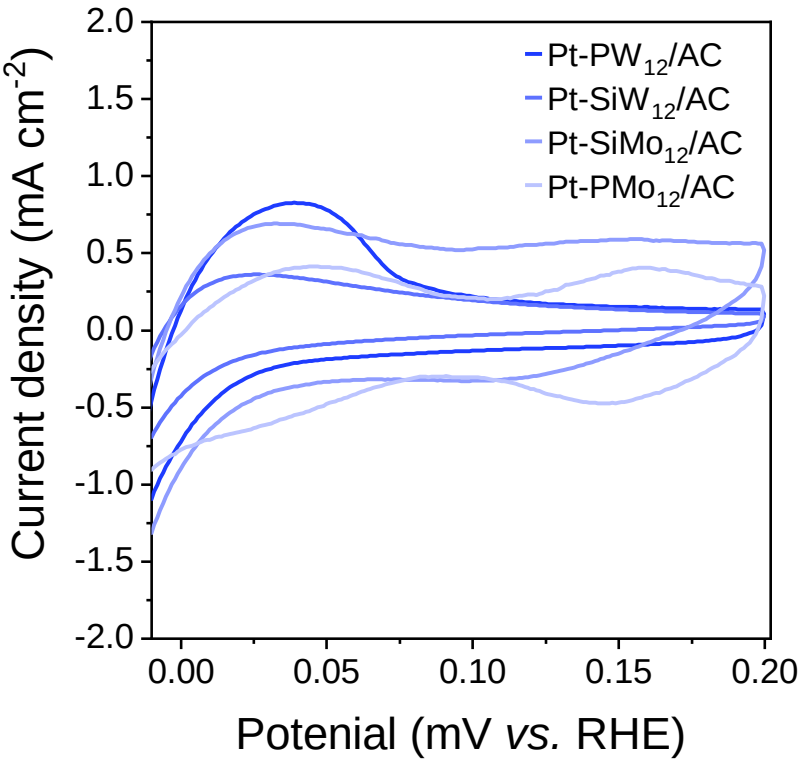

Fig. S43. Hydrogen desorption region of the steady-state cyclic voltammetry curves for Pt-POMs/AC at a scan rate of 50 mV s^{-1}.

Generally, electrochemical adsorption of hydrogen on the surface of precious metals can occur at a more positive potential (viz. underpotential) compared to RHE. Meanwhile, the hydrogen (H_{ad}) binding energy (HBE) of a catalyst can be evaluated by such peak potential of absorbed hydrogen desorption peak with CV while hydrogen coverage can be determined by the peak area.[18, 19]

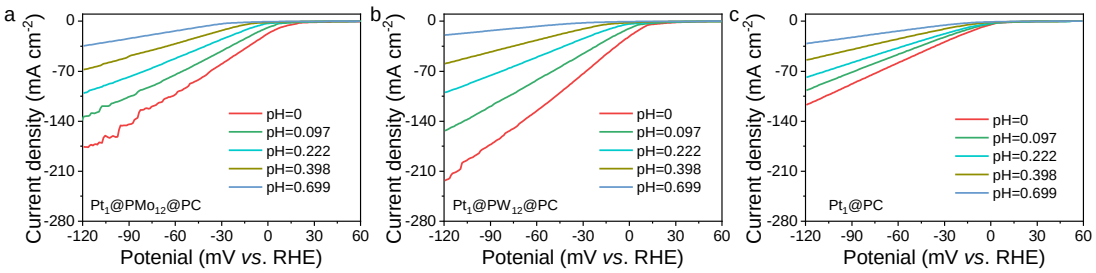

Fig. S44. The pH-dependence measurements. LSV curves of (**a**) $Pt_1@PMo_{12}@PC$, (**b**) $Pt_1@PW_{12}@PC$, and (**c**) $Pt_1@PC$ in Ar-saturated H_2SO_4 electrolyte with pH ranging from 0 to 0.699.

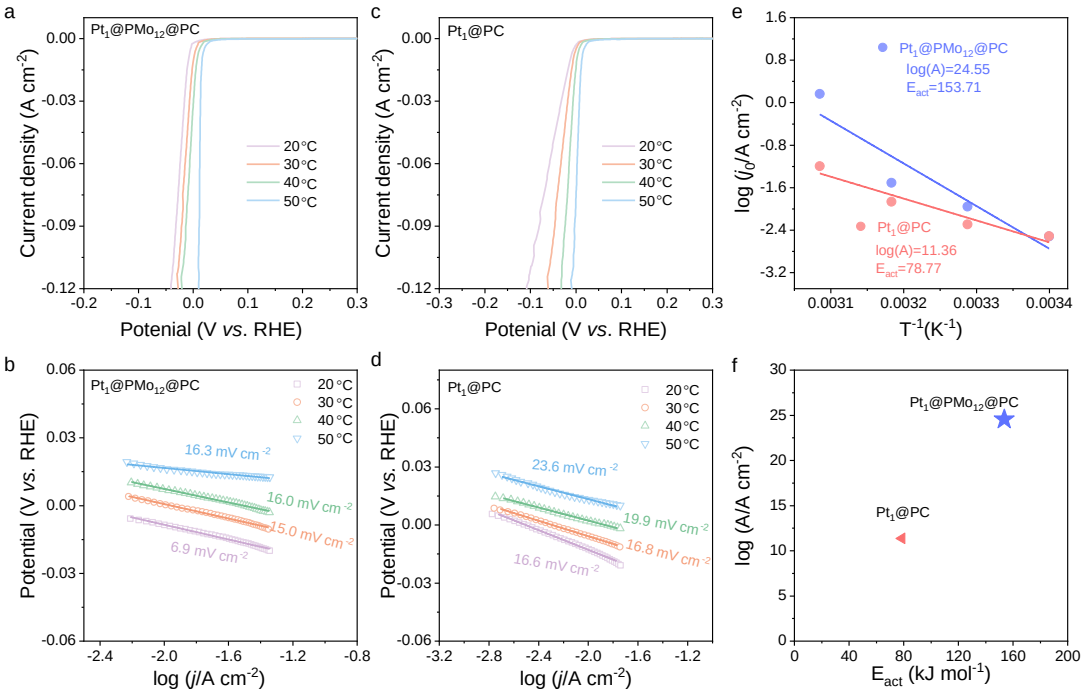

Fig. S45. Example of Ohmic drop-corrected HER polarization curves and Tafel plots for $Pt_1@PMo_{12}@PC$ (a, b) and $Pt_1@PC$ (c, d) in 0.5 M H_2SO_4 at four different temperatures, recorded using hydrodynamic LSV using a scan rate of 5 mV s^{-1} with 1600 rpm. (e) The Arrhenius plot for HER on $Pt_1@PMo_{12}@PC$ and $Pt_1@PC$ in in 0.5 M H_2SO_4. (f) Relation between activation energy (E_{act}) and the logarithm of pre-exponential factor (log *A*) as an illustration of the compensation effect for HER in acidic media.

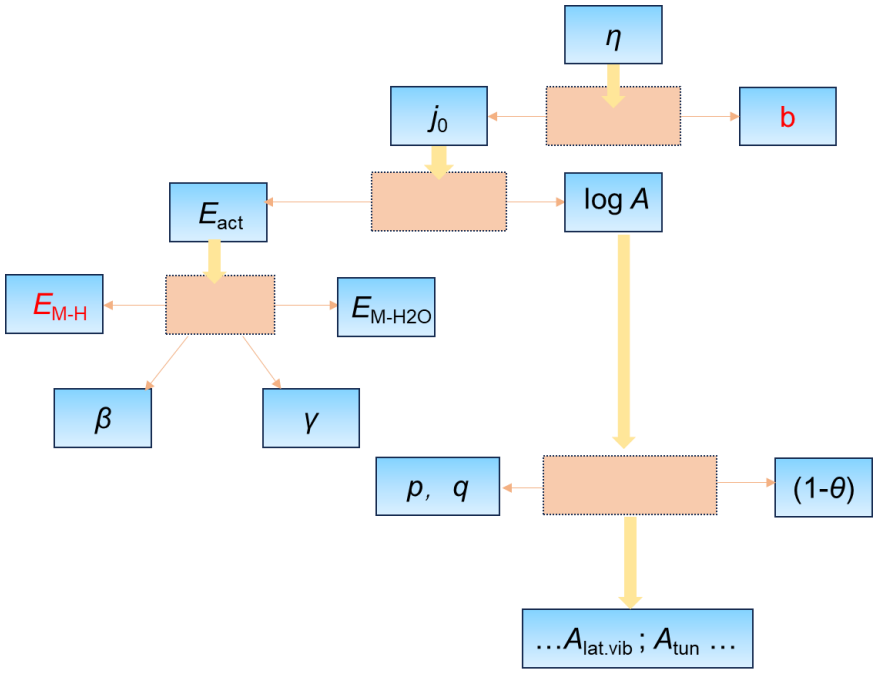

Fig. S46. Schematic representation of the rate law "dissection" with an indication of the relevant parameters that could be potentially linked with material properties or interfacial properties of the electrode/electrolyte boundary in acid[20].

Note that the meaning of each symbol is as follows: E_{act}, activation energy; A, preexponential factor; $E_{M\text{-}H}$, intermediate bond strength energy, which is linked with intermediate adsorption energy; $E_{M\text{-}H2O}$, energy consumed for metal water interaction or water bilayer reconstruction during HER; β, symmetry factor, γ, Bronsted-Evans-Polanyi coefficient, p, partial order concerning H^+ ion concentration; q, the partial order concerning the number of available active sites, θ is total coverage, $Al_{at.vib}$, the hypothetical contribution of individual and collective lattice vibrations to effective collisions; A_{tun}, the hypothetical contribution of proton tunneling to product formation.

Firstly, LSVs and corresponding Tafel slope on $Pt_1@PMo_{12}@PC$ (**Fig. S45a−b**) and $Pt_1@PC$ (**Fig. S45c−d**) at four different temperatures are given. As expected, as the temperature increases, the performance of both catalysts will be enhanced. Then, j_0 and Tafel slope can be obtained from the Tafel plots. The E_{act} and preexponential factor determination on our catalysts are further illustrated in **Fig. S45e** and **Note S2** ($\log j_0$ *vs* 1/T)[20, 21]. The slope of the inverse temperature dependence of the j_0 comprises E_{act}, while the intercept is equal to the logarithm of the pre-exponential factor. Notably, the $Pt_1@PMo_{12}@PC$ for HER shows a higher pre-exponential factor than that of $Pt_1@PC$ (**Fig. S45f**). So, the high HER activity of $Pt_1@PMo_{12}@PC$ in acidic electrolytes mainly depends on the pre-exponential frequency factor. In **Fig. S46**, it is evident that the H^+ concentration and the effective collision of reactants with the surface of the electrocatalyst are related to the pre-exponential factor. Therefore, it can be predicted that the H-spillover can encourage more effective collisions of H^+ with the active surface of Pt and improve the H coverage on the Pt surface. So, we speculate that Arrhenius plots may be used as a criterion for judging the occurrence of H-spillover.

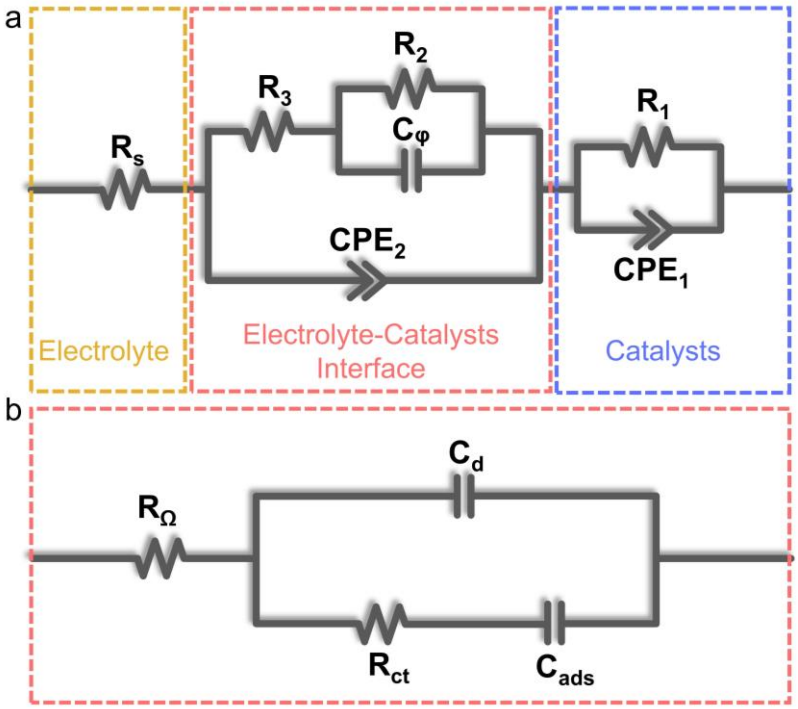

Fig. S47. (**a**) Schematic diagram of the electrode structure and the equivalent circuit model. (**b**) Equivalent circuit model of intermediate adsorption.

The EIS data was simulated using an equivalent circuit model (**Fig. S47a)** consisting of four parts, namely, electron transfer from the catalyst inner-layer to the reaction interface (R_1 and CPE_1), reaction intermediate (H_{ad}) adsorption (R_2 and C_φ), catalyst-electrolyte interface charge transfer (R_3 and CPE_2), and electrolyte resistance (Rs),[22] where CPE refers to constant phase angle components. C_φ and R_2 represent Volmer step relating to low-frequency region while CPE_2 and R_3 represent Heyrovsky step associating with middle-frequency region. Note that the intermediate (H_{ad}) adsorption behavior on the active sites can be reflected by C_φ,[14, 22, 23] which includes double layer capacitance (C_d) and adsorption layer capacitance (C_{ads}) (**Fig. S47b)**.[24] Besides, C_φ as a function of overpotential can be integrated to calculate the hydrogen adsorption charge (Q_{H^*}) on a unit area of Pt during HER.[14]

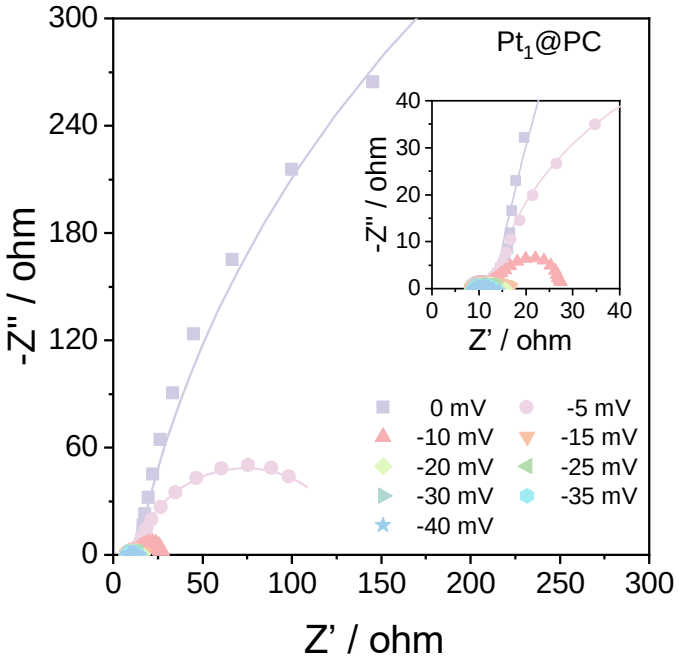

Fig. S48. Nyquist plots of Pt_1@PC at different overpotentials. The inside is a zoomed-in view.

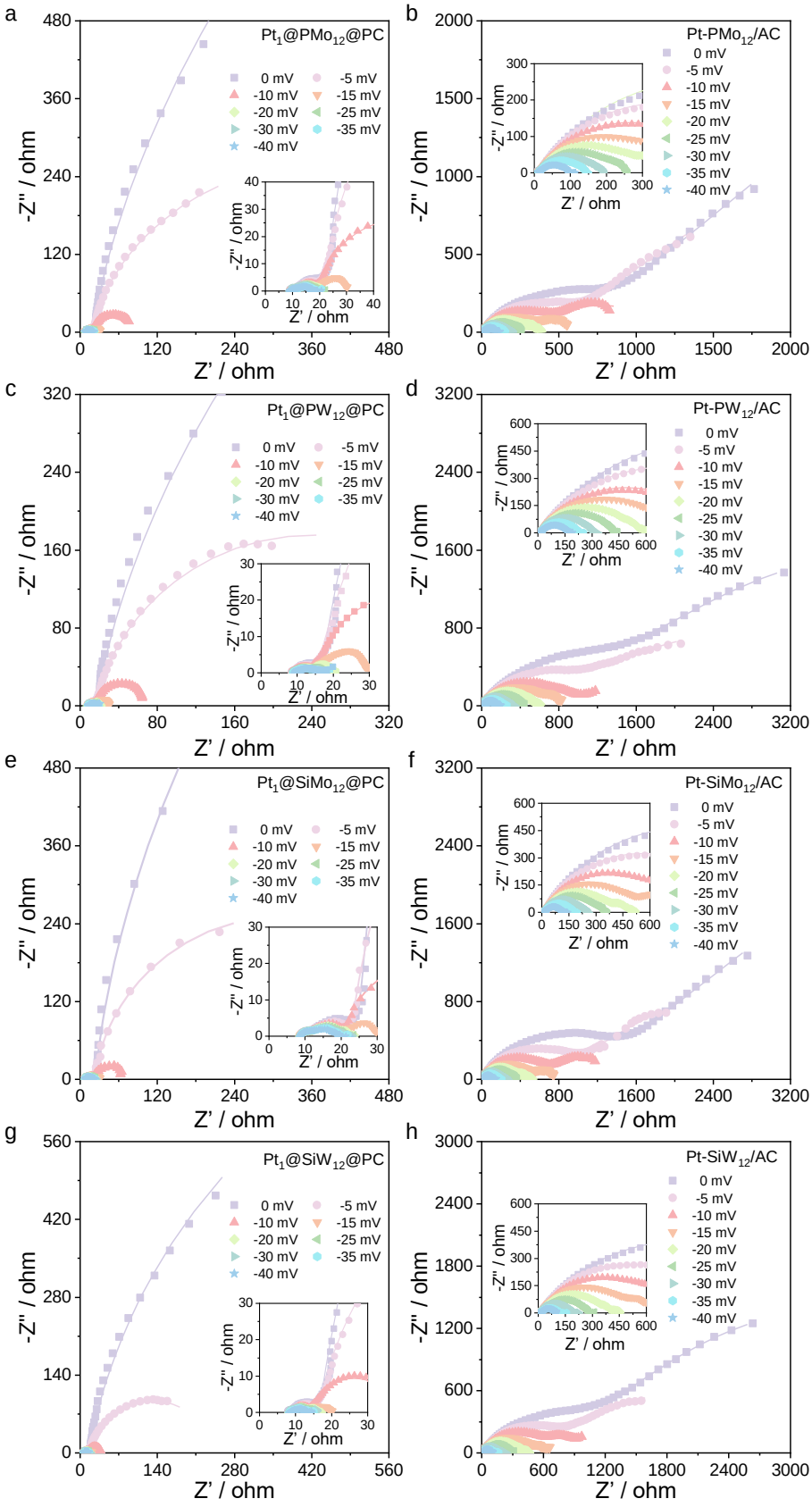

Fig. S49. Nyquist plots of Pt_1@POMs@PC and Pt-POMs/AC at different overpotentials. The inside is a zoomed-in view.

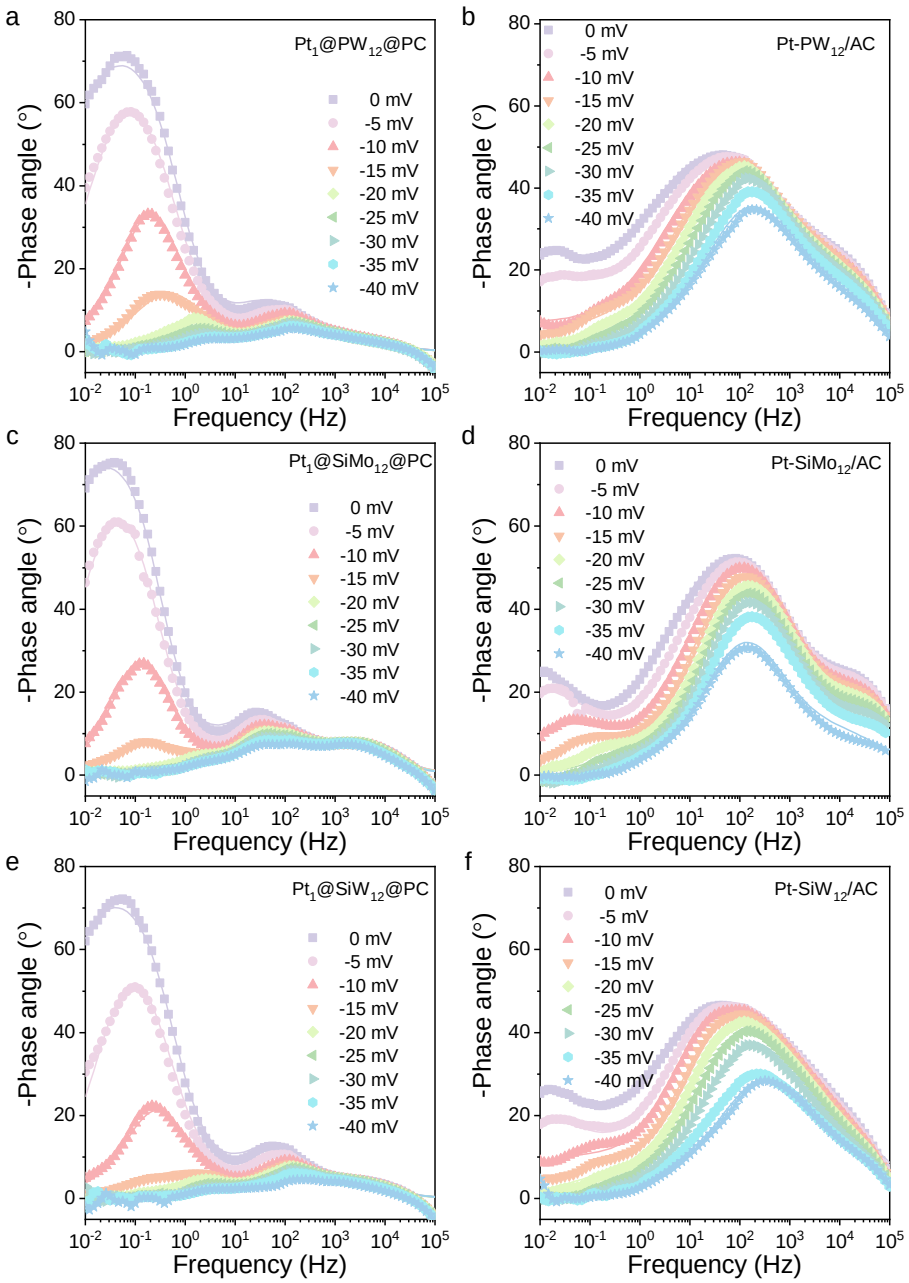

Fig. S50. Bode plots of Pt_1@POMs@PC (Pt_1@PW_{12}@PC, Pt_1@$SiMo_{12}$@PC, and Pt_1@SiW_{12}@PC) and Pt-POMs/AC (Pt-PW_{12}/AC, Pt-SiW_{12}/AC, and Pt-$SiMo_{12}$/AC) at various overpotentials.

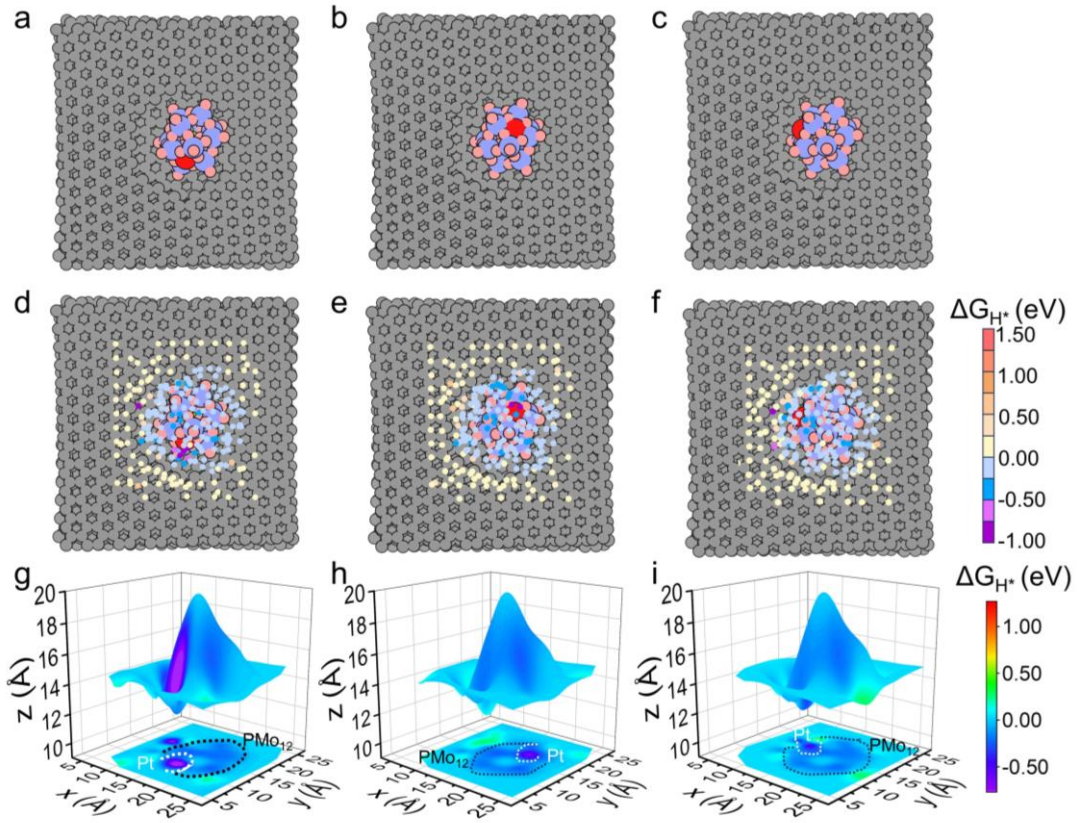

Fig. S51. Optimized structural models showing the top view of (**a**) Pt_1@PMo_{12}@G-01, (**b**) Pt_1@PMo_{12}@G-02, and (**c**) Pt_1@PMo_{12}@G-03. H adsorption free energy maps for HER on (**d**) Pt_1@PMo_{12}@G-01, (**e**) Pt_1@PMo_{12}@G-02, and (**f**) Pt_1@PMo_{12}@G-03. Corresponding 3D contour of ΔG_{H^*} on (**g**) Pt_1@PMo_{12}@G-02, (**h**) Pt_1@PMo_{12}@G-02, and (**i**) Pt_1@PMo_{12}@G-03.

Since there are three 4H sites exposed on the surface of confined POMs. The H migration processes for three surface O4H sites are calculated and the Pt at the other two surface O4H sites of confined PMo_{12} are shown in **Fig. S51**. Note that H migration processes at the other two surface O4H sites of confined PMo_{12} show a similar phenomenon. The ΔG_{H^*} gradually decreases, as manifested by the step-by-step discoloration of the H* from purple to yellow, which indicates the occurrence of successive H* migration processes, representing an H-buffer effect.

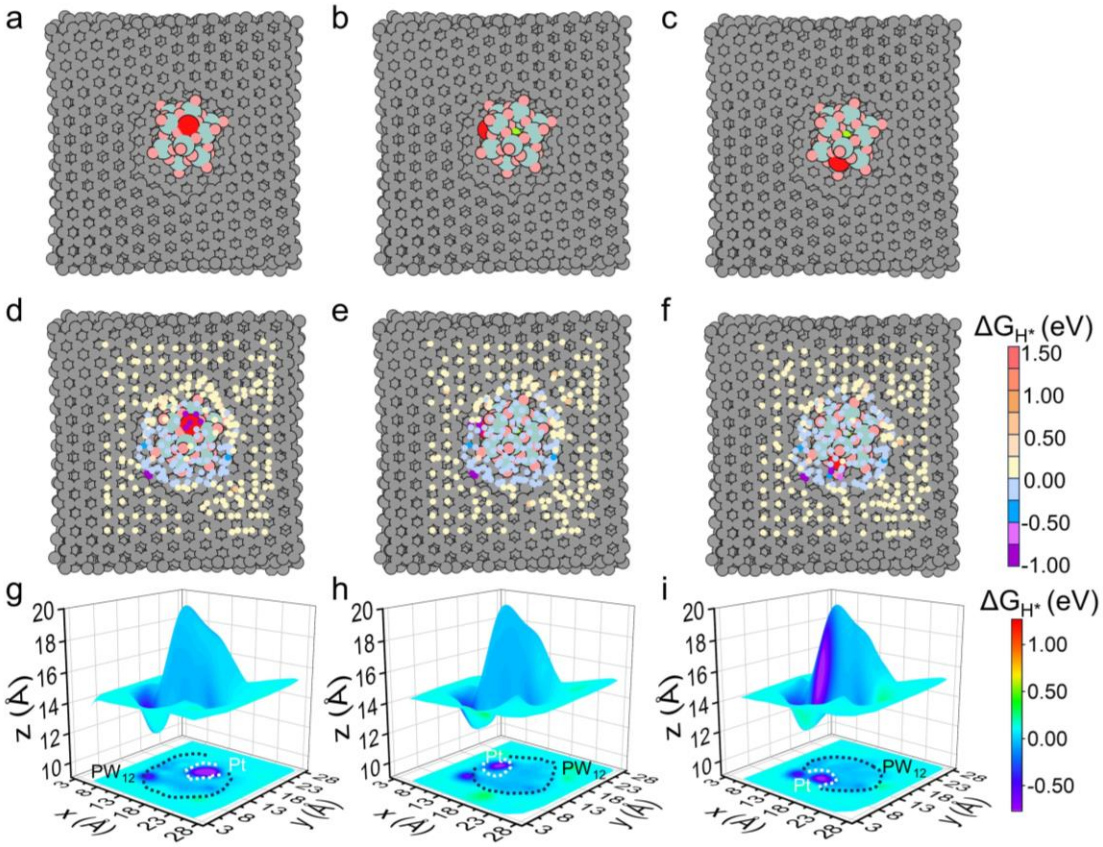

Fig. S52. Optimized structural models showing the top view of (**a**) $Pt_1@PW_{12}$@G-01, (**b**) $Pt_1@PW_{12}$@G-02, and (**c**) $Pt_1@PW_{12}$@G-03. H adsorption free energy maps for HER on (**d**) $Pt_1@PW_{12}$@G-01, (**e**) $Pt_1@PW_{12}$@G-02, and (**f**) $Pt_1@PW_{12}$@G-03. Corresponding 3D contour of ΔG_{H^*} on (**g**) $Pt_1@PW_{12}$@G-01, (**h**) $Pt_1@PW_{12}$@G-02, and (**i**) $Pt_1@PW_{12}$@G-03.

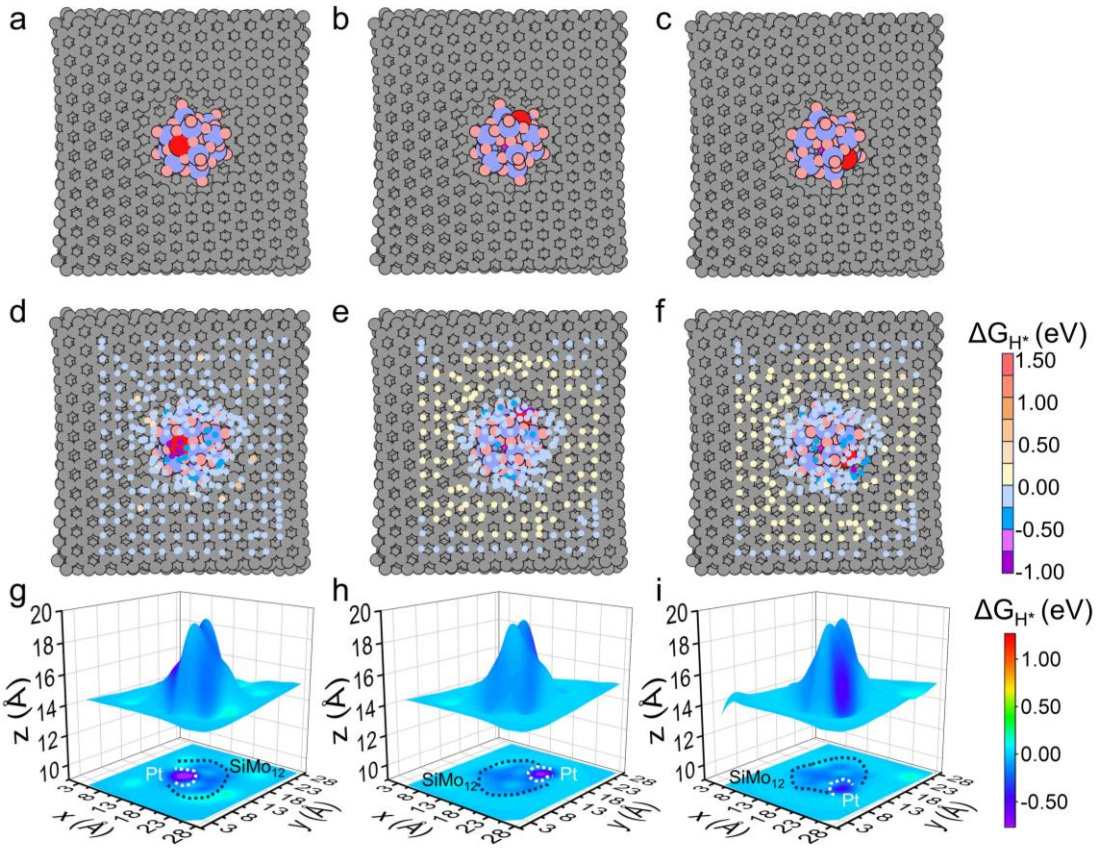

Fig. S53. Optimized structural models showing the top view of (**a**) Pt_1@$SiMo_{12}$@G-01, (**b**) Pt_1@$SiMo_{12}$@G-02, and (**c**) Pt_1@$SiMo_{12}$@G-03. H adsorption free energy maps for HER on (**d**) Pt_1@$SiMo_{12}$@G-01, (**e**) Pt_1@$SiMo_{12}$@G-02, and (**f**) Pt_1@$SiMo_{12}$@G-03. 3D contour of ΔG_{H^*} on (**g**) Pt_1@$SiMo_{12}$@G-01, (**h**) Pt_1@$SiMo_{12}$@G-02, and (**i**) Pt_1@$SiMo_{12}$@G-03.

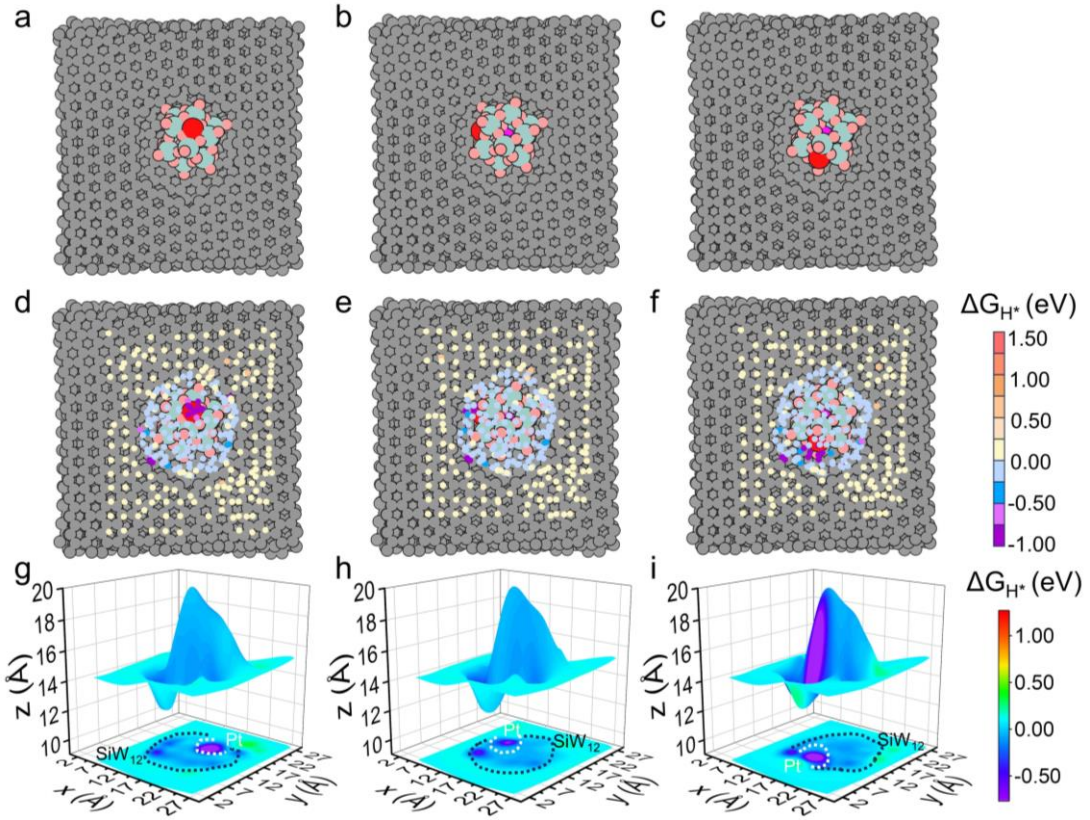

Fig. S54. Optimized structural models showing the top view of (**a**) Pt_1@SiW_{12}@G-01, (**b**) Pt_1@SiW_{12}@G-02, and (**c**) Pt_1@SiW_{12}@PC-03. H adsorption free energy maps for HER on (**d**) Pt_1@SiW_{12}@G-01, (**e**) Pt_1@SiW_{12}@G-02, and (**f**) Pt_1@SiW_{12}@G-03. Corresponding 3D contour of ΔG_{H^*} on (**g**) Pt_1@SiW_{12}@G-01, (**h**) Pt_1@SiW_{12}@G-02, and (**i**) Pt_1@SiW_{12}@G-03.

The role of confined POMs as a buffer chain is confirmed by the larger light-blue areas (from -0.25 to 0 eV) with ΔG_{H^*} close to 0 eV around PMo_{12} (**Fig. S51**), PW_{12} (**Fig. S52**), $SiMo_{12}$ (**Fig. S53**), and SiW_{12} (**Fig. S54**).

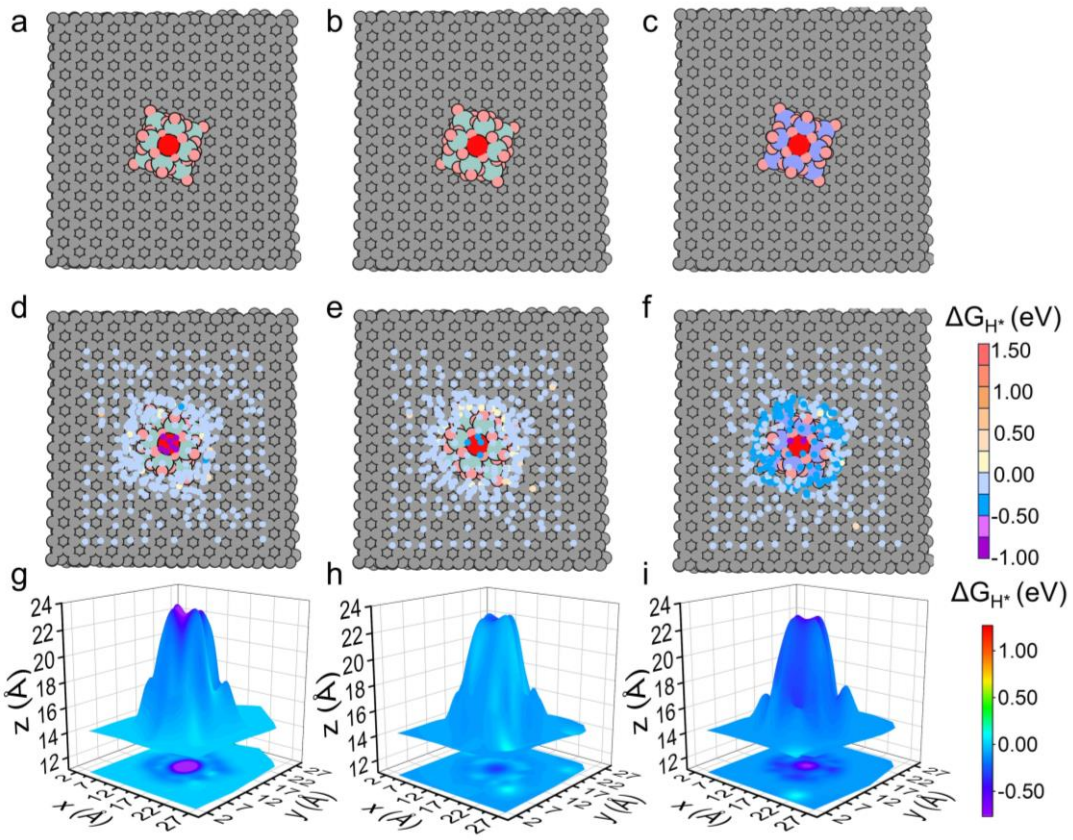

Fig. S55. Optimized structural models showing the top view of (**a**) $Pt_1@PW_{12}/G$, (**b**) $Pt_1@SiW_{12}/G$, and (**c**) $Pt_1@SiMo_{12}/G$. H* adsorption free energy maps for HER on (**d**) $Pt_1@PW_{12}/G$, (**e**) $Pt_1@SiW_{12}/G$, and (**f**) $Pt_1@SiMo_{12}/G$. 3D contour of ΔG_{H^*} on (**g**) $Pt_1@PW_{12}/G$, (**h**) $Pt_1@SiW_{12}/G$, and (**i**) $Pt_1@SiMo_{12}/G$.

Generally, Mo−H possesses a greater bonding energy compared to W−H, indicating the easier formation of Mo−H than W−H.[25] Compared with $Pt_1@PW_{12}/G$ and $Pt_1@SiW_{12}/G$, larger dark-blue areas are shown around the PMo_{12} and $SiMo_{12}$ for $Pt_1@SiMo_{12}/G$ and $Pt_1@PMo_{12}/G$, implying PMo_{12} and $SiMo_{12}$ are exactly unfavorable for H* desorption due to the strong Mo−H bond (**Fig. 6b** and **Fig. S55**). In contrast, for $Pt_1@PMo_{12}@G$ and $Pt_1@SiMo_{12}@G$ (**Fig. S51** and **Fig. S53**), the area around confined the PMo_{12} and $SiMo_{12}$ are significantly reduced in comparison with $Pt_1@SiMo_{12}/G$ and $Pt_1@PMo_{12}/G$, which illustrates that the dual-confinement system can overcome the strong H-binding with Mo, again confirming the buffer effect of confined POMs. Compared with $Pt_1@PW_{12}/G$ and $Pt_1@SiW_{12}/G$, confined PW_{12} and SiW_{12} in $Pt_1@PW_{12}@G$ and $Pt_1@SiW_{12}@G$ also show similar phenomenon with smaller dark-blue area (**Fig. S52** and **Fig. S54**).

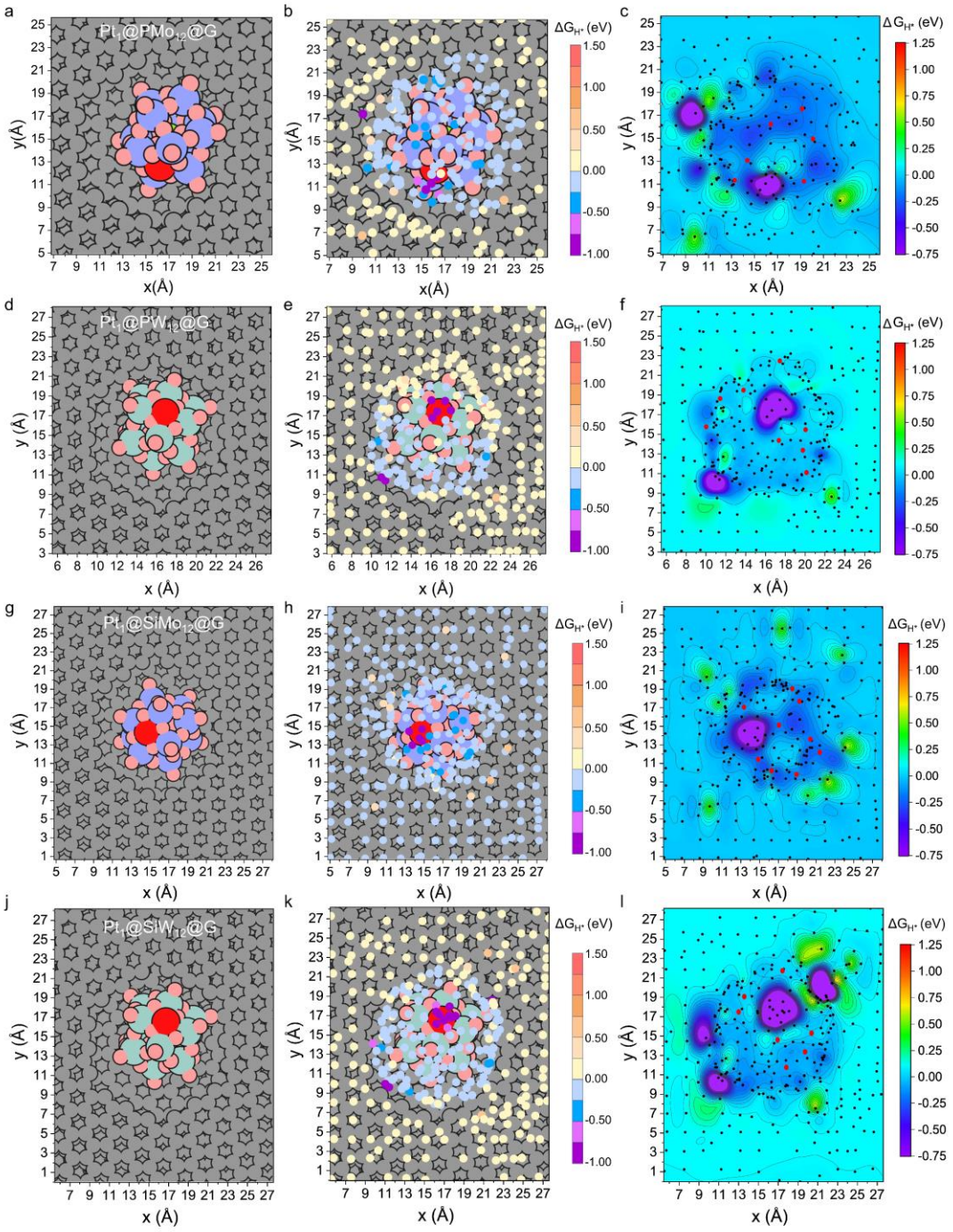

Fig. S56. (**a, d, g, j**) Optimized structural models showing the top view of Pt_1@POMs@G. (**b, e, h, k**) H adsorption free energy maps for HER. (**c, f, i, l**) contour plots of PES resulting from the panel. Saddle points representing TS are marked with red dots in contour plots.

Although sub-nanopores in support occasionally show a certain H adsorption ability (purple area on supports), the absence of gradient energy barriers indicates that the adsorbed H is not easily desorbed. So, H-spillover mainly occurs through the H-buffer chain.

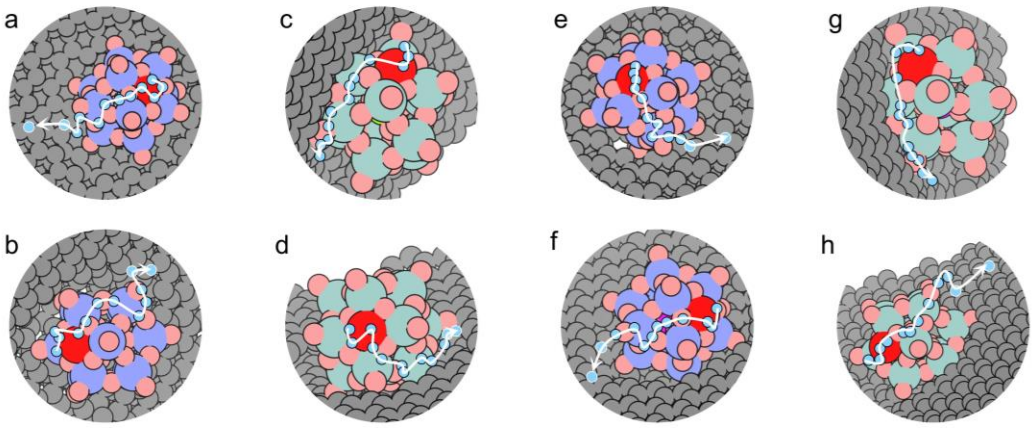

Fig. S57. Schematic illustration of typical hydrogen spillover paths on (**a**) Pt_1@PMo_{12}@G-02, (**b**) Pt_1@PMo_{12}@G-03, (**c**) Pt_1@PW_{12}@G-02, (**d**) Pt_1@PW_{12}@G-03, (**e**) Pt_1@$SiMo_{12}$@G-02, (**f**) Pt_1@$SiMo_{12}$@G-03, (**g**) Pt_1@SiW_{12}@G-02, and (**h**) Pt_1@$SiMo_{12}$@G-03 for HER in acid.

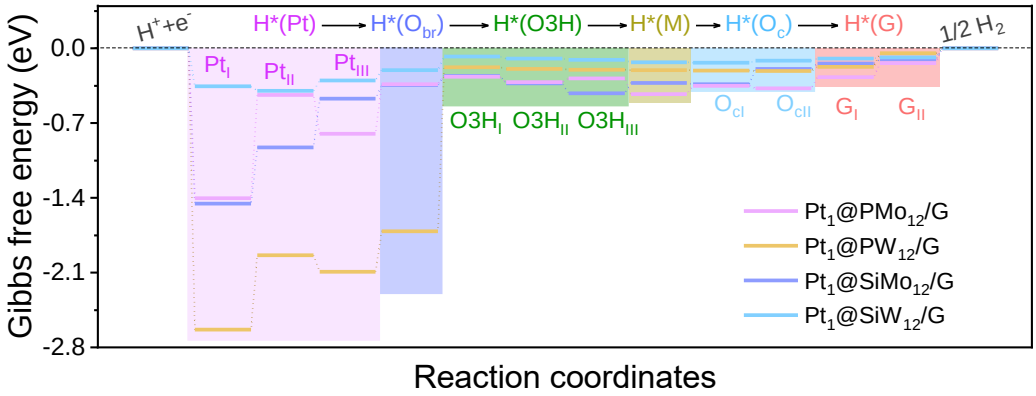

Fig. S58. Typical free energy diagram for HER on Pt_1@POMs/G.

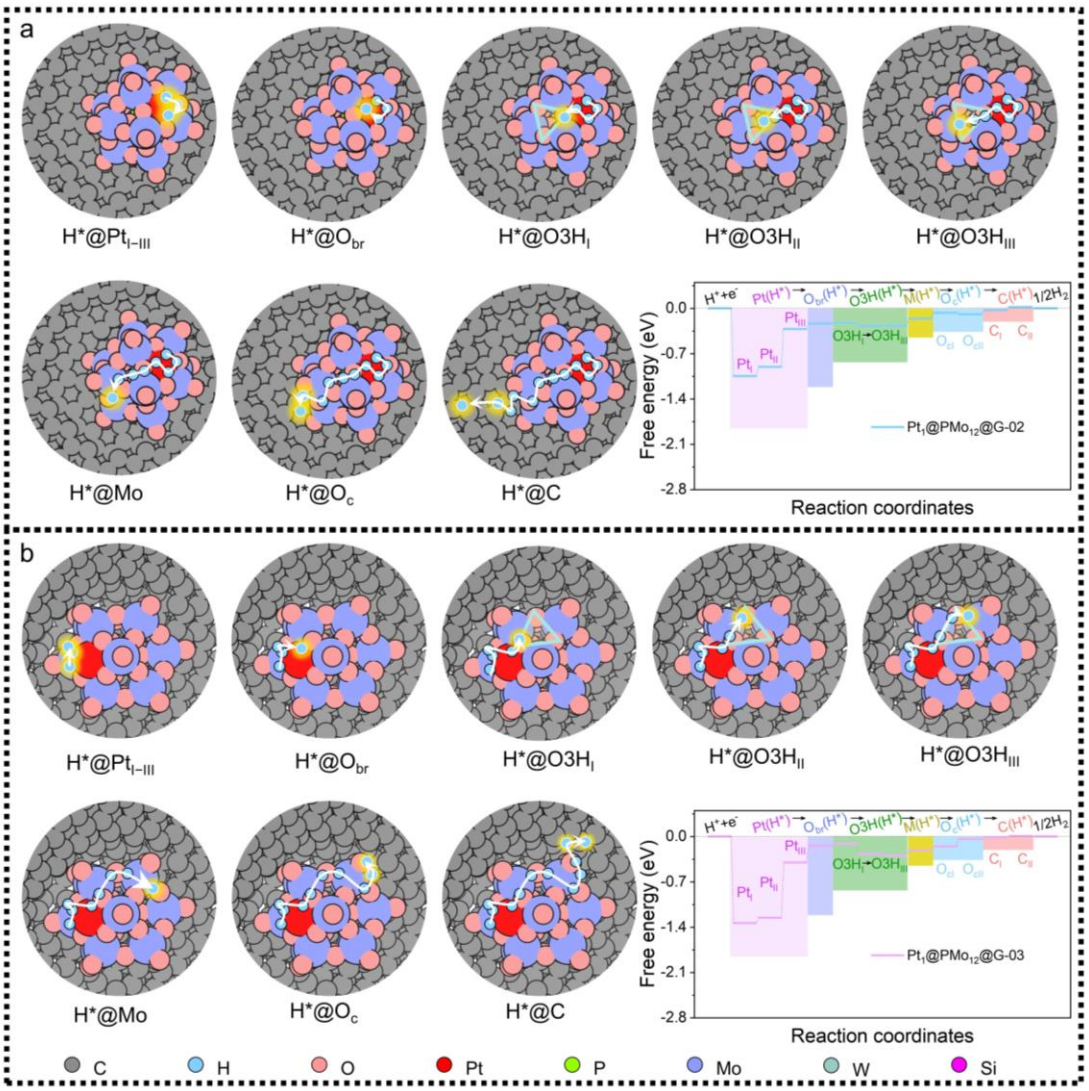

Fig. S59. Schematic illustration of hydrogen spillover path at atomic-scale on the (**a**) Pt_1@PMo_{12}@G-02 and (**b**) Pt_1@PMo_{12}@G-03; Inset are typical free energy diagrams for HER on (**a**) Pt_1@PMo_{12}@G-02 and (**b**) Pt_1@PMo_{12}@G-03.

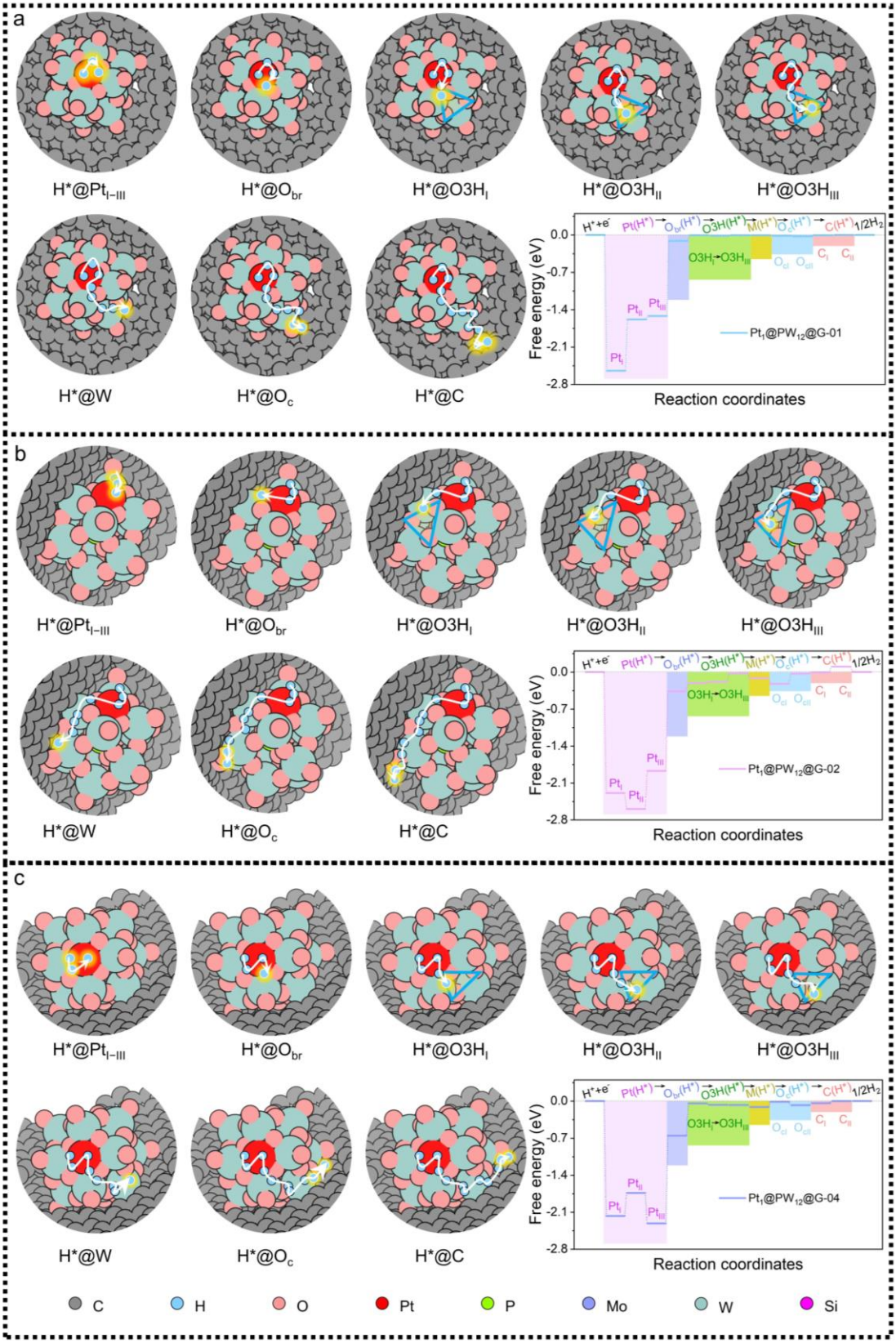

Fig. S60. Schematic illustration of hydrogen spillover paths at atomic-scale on the (**a**) Pt_1@PW_{12}@G-01, (**b**) Pt_1@PW_{12}@G-02, and (**c**) Pt_1@PW_{12}@G-03; Inset are typical free energy diagrams for HER on (**a**) Pt_1@PW_{12}@G-01, (**b**) Pt_1@PW_{12}@G-02, and (**c**) Pt_1@PW_{12}@G-03.

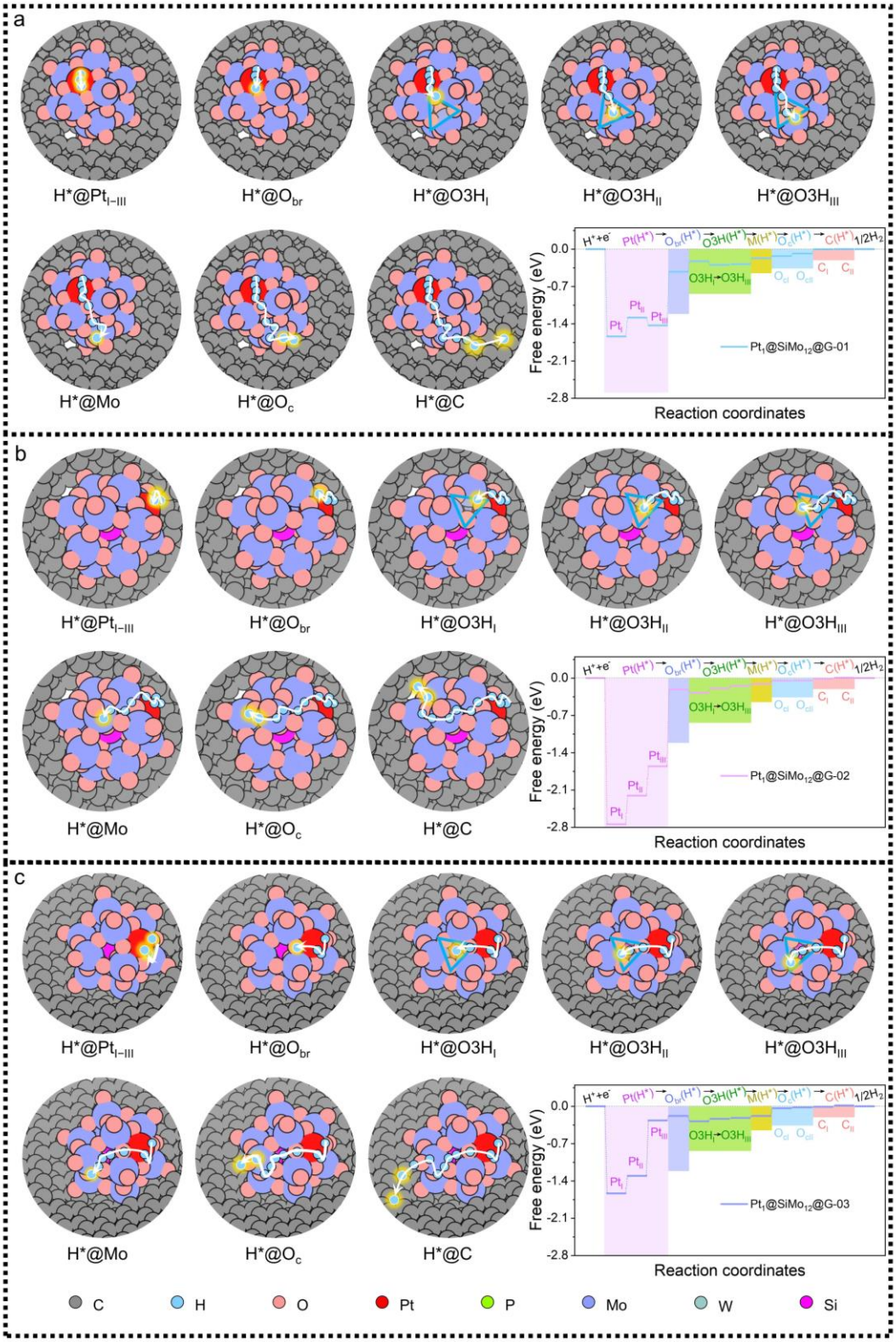

Fig. S61. Schematic illustration of hydrogen spillover paths at atomic-scale on the (**a**) Pt_1@$SiMo_{12}$@G-01, (**b**) Pt_1@$SiMo_{12}$@G-02, and (**c**) Pt_1@$SiMo_{12}$@G-03; Inset are typical free energy diagrams for HER on (**a**) Pt_1@$SiMo_{12}$@G-01, (**b**) Pt_1@$SiMo_{12}$@G-02, and (**c**) Pt_1@$SiMo_{12}$@G-03.

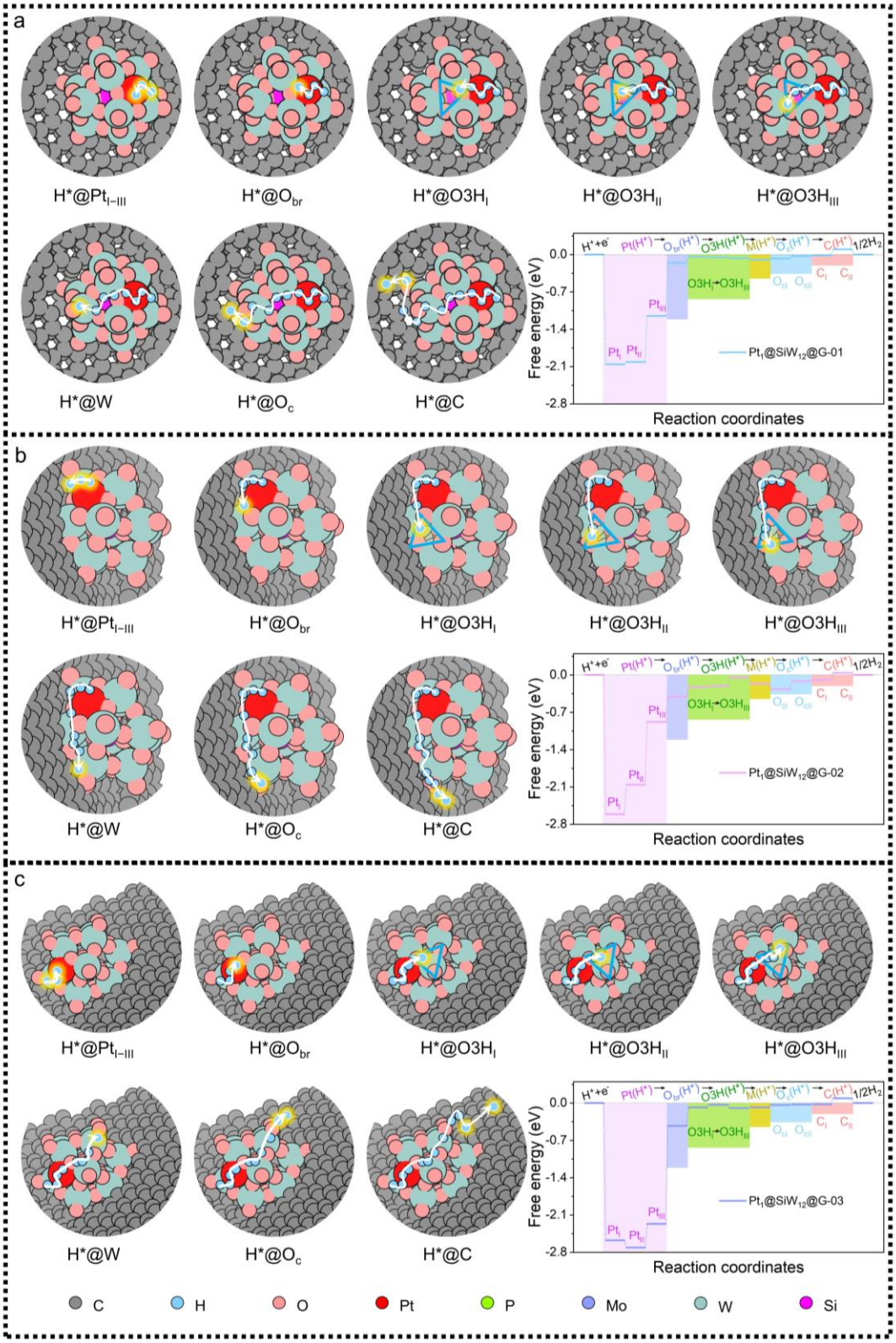

Fig. S62. Schematic illustration of hydrogen spillover path at atomic-scale on the (**a**) Pt_1@SiW_{12}@G-01, (**b**) Pt_1@SiW_{12}@G-02, and (**c**) Pt_1@SiW_{12}@G-03; Inset are typical free energy diagrams for HER on (**a**) Pt_1@SiW_{12}@G-01, (**b**) Pt_1@SiW_{12}@G-02, and (**c**) Pt_1@SiW_{12}@G-03.

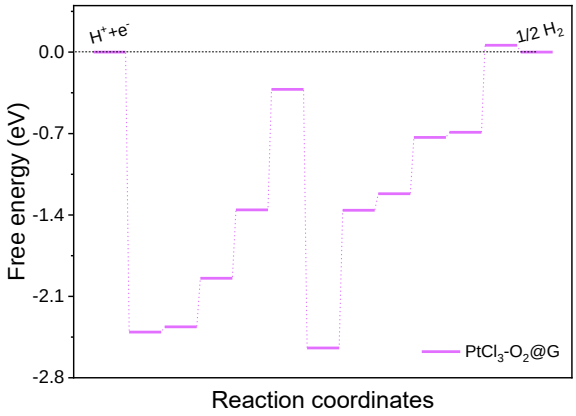

Fig. S63. Typical free energy diagram for HER on $PtCl_3$-O_2@G.

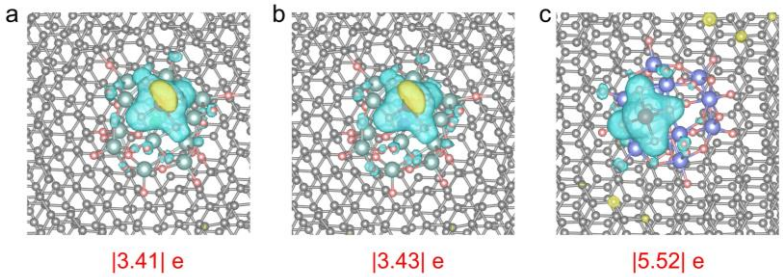

Fig. S64. Differential charge densities for (**a**) $Pt_1@PW_{12}@G$, (**b**) $Pt_1@SiW_{12}@G$, and (**c**) $Pt_1@SiMo_{12}@G$.

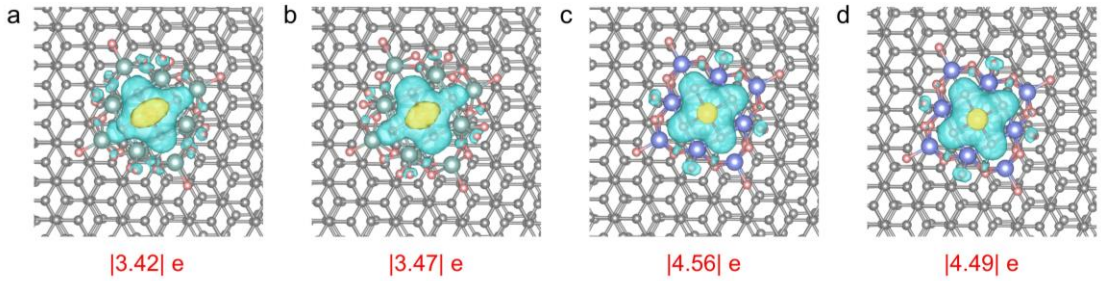

Fig. S65. Differential charge densities for (**a**) $Pt_1@PW_{12}/G$, (**b**) $Pt_1@SiW_{12}/G$, (**c**) $Pt_1@PMo_{12}/G$, and (**d**) $Pt_1@SiMo_{12}/G$.

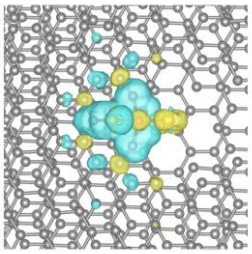

Fig. S66. The differential charge density for $PtCl_3$-O_2@G.

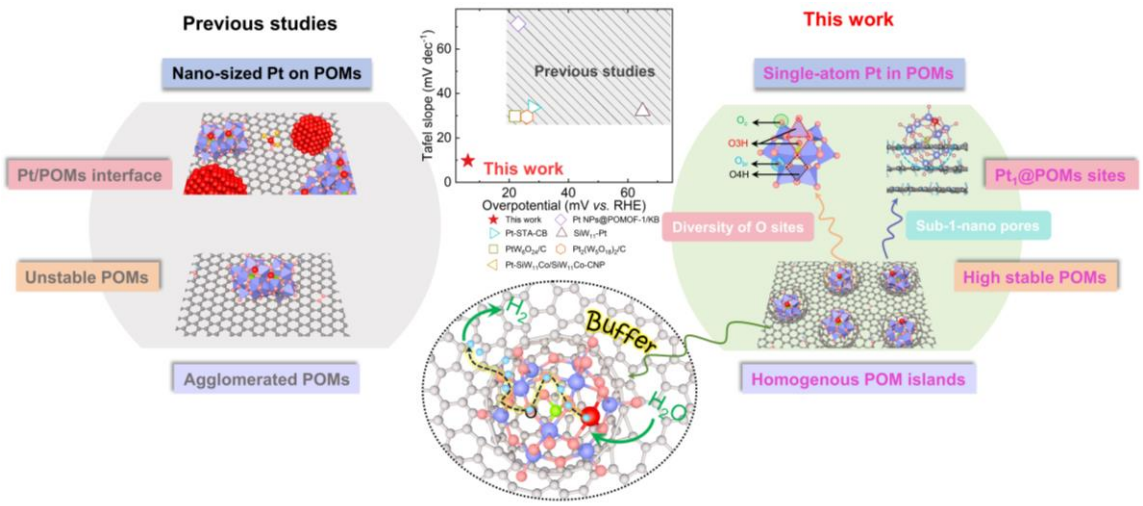

Fig. S67. Comparison of Pt/POMs-contained composite catalysts for HER.
(Ref: Pt NPs@POMOF-1/KB,[26] Pt-STA-CB,[27] SiW_{11}-Pt,[28] PtW_6O_{24}/C,[29] $Pt_2(W_5O_{18})_2$/C,[14] Pt-$SiW_{11}Co$/$SiW_{11}Co$-CNP[30]).

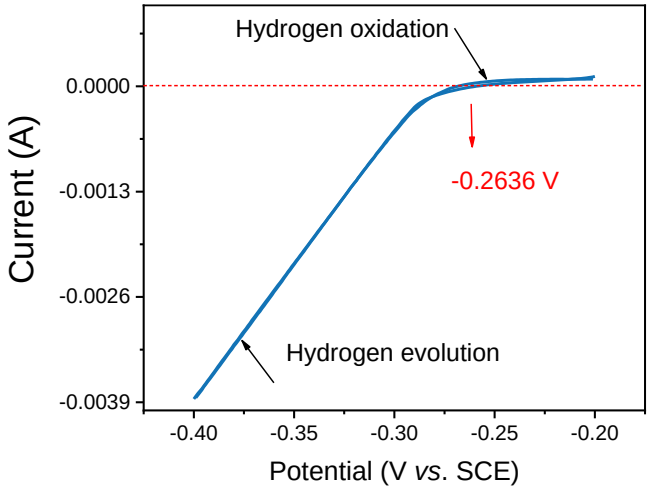

Fig. S68. RHE calibration of SCE reference electrode in 0.5 M H_2SO_4.

Table S1. Binding energies of Pt atom in supports.

Label	Binding energy (eV)
$Pt_1@PMo_{12}@G$-4H	-1.46
$Pt_1@PMo_{12}@G$-3H	-1.63
$Pt_1@PMo_{12}/G$	-0.95
$Pt_1@PW_{12}@G$-4H	-2.6
$Pt_1@PW_{12}@G$-3H	0.94
$Pt_1@PW_{12}/G$	-0.6
$Pt_1@SiMo_{12}@G$-4H	-1.3
$Pt_1@SiMo_{12}@G$-3H	3.97
$Pt_1@SiMo_{12}/G$	-0.9
$Pt_1@SiW_{12}@PC$-4H	-1.47
$Pt_1@SiW_{12}@PC$-3H	9.32
$Pt_1@SiW_{12}/G$	-1.2
$Pt_1@G$(O/POMs)	-0.78
$Pt_1@G$(O)	-0.6
$PtCl_3$-$O_2@G$	-2.74

Table S2. The geometry parameters of POMs and Pt atoms confined in O4H sites of POMs@G and POMs/G.

Label	Pt−O bond length (Å)[a]	Dihedral angle (◦)[a]
PMo_{12}	-	16.715
$Pt_1@PMo_{12}@G$-01	1.946, 1.964, 1.692, 1.704	0.1776
$Pt_1@PMo_{12}@G$-02	1.976, 1.861, 1.734, 1.792	0.0523
$Pt_1@PMo_{12}@G$-03	1.798, 1.843, 1.808, 1.839	0.6851
$Pt_1@PMo_{12}/G$	1.812, 1.809, 1.829, 1.833	0.1111
$SiMo_{12}$	-	21.4450
Pt1@$SiMo_{12}@G$-01	1.882, 1.841, 1.800, 1.795	0.1004
$Pt_1@SiMo_{12}@G$-02	2.077, 1.857, 1.809, 1.575,	1.2267
$Pt_1@SiMo_{12}@G$-03	1.863, 1.863, 1.835, 1.781,	0.4576
$Pt_1@SiMo_{12}/G$	1.812, 1.830, 1.852, 1.835	0.0892
PW_{12}	-	16.8300
$Pt_1@PW_{12}@G$-01	1.972, 2.045, 1.650, 1.657	15.7900
$Pt_1@PW_{12}@G$-02	2.106, 1.950, 1.777, 1.552	17.5800
$Pt_1@PW_{12}@G$-03	2.060, 1.946, 1.639, 1.706,	15.9586
$Pt_1@PW_{12}/G$	2.064, 1.999, 1.654, 1.702,	16.5803
SiW_{12}	-	19.6000
$Pt_1@SiW_{12}@PC$-01	2.136, 1.969, 1.672, 1.669	18.8202
$Pt_1@SiW_{12}@PC$-02	1.978, 2.098, 1.538, 1.726	18.7992
$Pt_1@SiW_{12}@PC$-03	2.191, 2.658, 1.616, 1.640,	20.1720
$Pt_1@SiW_{12}@G$	2.169, 2.200, 1.585, 1.629,	22.6756

[a] Note that for Mo-based POMs (PMo_{12} and $SiMo_{12}$), the length of the four Pt-O bonds is approximate and four oxygens of O4H site tend to be in one plane, suggesting that the introduction of Pt has a great influence on the configuration of PMo_{12} and $SiMo_{12}$, as confirmed by the significantly reduced dihedral angle. For W-based POMs, two Pt−O bonds are longer and two Pt−O bonds are shorter, as demonstrated by the dihedral angle showing non-obvious change. This may be attributed to the difference in atomic structure between Mo and W.

Table S3. EXAFS curve fitting parameters at the Pt *L*3-edge for various samples.

Catalyst	Shell	*CN*[a]	*R*(Å)[b]	σ^2(Å^2)[c]	ΔE_0(eV)[d]	*R* factor
Pt-foil	Pt−Pt	12*	2.765±0.003	0.0041±0.0004	7.8±0.5	0.0072
PtO_2	Pt−O	5.2±0.4	2.011±0.001	0.0026±0.0008	9.5±0.5	0.0099
	Pt−Pt	3.2±0.7	3.078±0.001		5.6±1.6	
	Pt−O	11.6±2.2	4.043±0.001		-1.7±1.0	
Pt_1@PMo_{12}@PC	Pt−O	4.3±0.5	1.987±0.001	0.0007±0.0015	9.9±0.9	0.0093
Pt_1@PC	Pt−O	1.6±0.2	2.058±0.001	0.0029±0.0015	7.4±0.4	0.0080
	Pt−Cl	2.9±0.4	2.332±0.001			

[a]*CN*, coordination number; [b]*R*, the distance to the neighboring atom; [c]σ^2, the Mean Square Relative Displacement (MSRD); [d]ΔE_0, inner potential correction; *R* factor indicates the goodness of the fit. $S0^2$ was fixed to 0.756 and 0.938, according to the experimental EXAFS fit of Pt foil and Mo foil by fixing *CN* as the known crystallographic value. * This value was fixed during EXAFS fitting, based on the known structure. Fitting range: $2.1 \le k$ (/Å) ≤ 12.0 and $1.3 \le R$ (Å) ≤ 3.2 (Pt foil); $3.0 \le k$ (/Å) ≤ 12.0 and $1.3 \le R$ (Å) ≤ 3.6 (PtO_2); $2.1 \le k$ (/Å) ≤ 12.0 and $1.2 \le R$ (Å) ≤ 2.0 (Pt_1@PMo_{12}@PC); $2.1 \le k$ (/Å) ≤ 12.0 and $1.2 \le R$ (Å) ≤ 2.5 (Pt_1@PC); $2.5 \le k$ (/Å) ≤ 12.0 and $1.0 \le R$ (Å) ≤ 3.4 (Mo foil); $3.0 \le k$ (/Å) ≤ 12.0 and $0.7 \le R$ (Å) ≤ 4.0 (MoO_3); $2.5 \le k$ (/Å) ≤ 11.5 and $0.6 \le R$ (Å) ≤ 2.0 (Pt_1@PMo_{12}@PC). A reasonable range of EXAFS fitting parameters: $0.700 < S_0^2 < 1.000$; $CN > 0$; $\sigma^2 > 0$ Å^2; $|\Delta E_0| < 15$ eV; *R* factor < 0.02.

Table S4. EXAFS curve fitting parameters at the Mo *K*-edge for various samples.

Catalyst	Shell	*CN*[a]	*R*(Å)[b]	σ^2(Å^2)[c]	ΔE_0(eV)[d]	*R* factor
Mo foil	Mo−Mo	8*	2.717±0.005	0.0038±0.0008	4.7±0.8	0.0057
	Mo−Mo	6*	3.135±0.009	0.0033±0.0010	5.6±1.4	
MoO_3	Mo−O	4.3±0.2	1.717±0.001	0.0074±0.0013	6.9±1.5	0.0159
	Mo−O	6.3±0.5	1.961±0.001			
	Mo−O	3.6±0.5	2.246±0.001			
	Mo−Mo	9.2±0.7	3.670±0.001	0.0085±0.0021	-5.5±0.8	
	Mo−Mo	2.1±0.3	4.036±0.001	0.0019±0.0041	8.3±1.8	
Pt_1@PMo_{12}@PC	Mo−O	4.2±0.5	1.689±0.001	0.0085±0.0019	-3.2±1.7	0.0097
	Mo−O	1.0±0.5	1.900±0.001			

Table S5. The C_{dl} and ECSA values of all samples.

Samples	C_{dl} (mF cm^{-2})	ECSA
Pt_1@PW_{12}@PC	10.67	177.8
Pt-PW_{12}/AC	0.683	11.38
Pt_1@PMo_{12}@PC	10.2	170
Pt-PMo_{12}/AC	1.59	25.5
Pt_1@SiW_{12}@PC	7.98	133
Pt-SiW_{12}/AC	0.658	10.97
Pt_1@$SiMo_{12}$@PC	13.9	231.67
Pt-$SiMo_{12}$/AC	0.383	6.38
20% Pt/C	9.77	162.83
Pt_1@PC	7.53	125.5
PC	1.82	30.333

Tabel S6. Exchange current densities extracted for HER in 0.5 M H_2SO_4

Materials	Log(j_0/ A cm^{-2}), 25°C	j_0(A cm^{-2}), 25°C
Pt_1@PMo_{12}@PC	-2.49	0.0032
Pt_1@PW_{12}@PC	-2.28	0.0052
Pt_1@$SiMo_{12}$@PC	-2.39	0.0040
Pt_1@SiW_{12}@PC	-2.48	0.0033
Pt-PMo_{12}/AC	-2.94	0.0011
Pt-PW_{12}/AC	-2.59	0.0025
Pt-$SiMo_{12}$/AC	-2.58	0.0026
Pt-SiW_{12}/AC	-2.54	0.0028
Pt_1@PC	-2.50	0.0031

Table S7. The HER activities of Pt_1@POMs@PC compared with other recently reported Pt single atom catalysts in 0.5 M H_2SO_4.

Samples	Tafel slopes (mV dec^{-1})	η_{10} (mV)	Mass loading (mg cm^{-2})	Mass activity (A mg_{Pt}^{-1})	TOF (s^{-1})	Ref
Pt_1@PMo_{12}@PC	14.8	8.30	0.132	3.68, 10 mV 18.8, 30 mV 37.78, 50 mV	3.72, 10 mV 19.3, 10 mV 39.0, 50 mV	This work
Pt_1@PW_{12}@PC	15.4	3.76	0.132	5.61, 10 mV 25.21, 30 mV 44.01, 50 mV	5.65, 10 mV 25.6, 30 mV 44.23, 50 mV	This work
Pt_1@$SiMo_{12}$@PC	9.76	6.12	0.132	2.85, 10 mV 17.23, 30 mV 25.85, 50 mV	3.07, 10 mV 18.3, 30 mV 25.6, 50 mV	This work
Pt_1@SiW_{12}@PC	18.5	6.8	0.132	2.45, 10 mV 10.17, 30 mV 19.66, 50 mV	2.66, 10 mV 10.6, 30 mV 20.17, 50 mV	This work
PtSA-MIL100/Fe	28.87	60	0.2	-	-	31
Bpy-CP-900@Pt	29.0	54	0.2538	1.24, 50 mV	-	32
Pt_{1+Cs}-NPC	12.5	24	0.198	4.59, 30 mV	16.94, 50 mV	33
Pt-$MoAl_{1-x}B$	78.8	18	3.0	4.0, 100 mV	0.68, 100 mV	34
Pt-SA/pCNFs	24	21	0.40	14.5, 50 mV	14.8, 50 mV	35
PtSA/CoAC-O@ACTP	43	61	0.3	64.0, 100 mV	-	36
$Ti_3C_2T_x$@PtSA	45	38	0.283	23.2, 100 mV	23.4, 50 mV	23
Pt/MoS_2	27	38	0.71	-	19.8, 100 mV	37
Pt/MoS_2-NTA/Ti_3C_2	35	32	-	46.5, 100 mV	47.0, 100 mV	38
Pt-CNTs	48.57	41	0.336	-	-	39
O@Pt on Au NDs	31	18	0.0038	-	40.1, 50 mV	40
PtW NPs/C	27.8	19.4	-	-	-	41
Pt-GDY_2	46.6	23.64	0.48	-	-	42
PtPVP/TNR@GC	27	21	1.25	16.53, 50 mV	-	43
AC Pt-NG/C	27	35.28	-	12.62, 50 mV	0.093, 50 mV	44
Pt/ WO_3@CFC	73	42	0.255	0.321, 20 mV	-	45
Pt SASs/AG	29.33	12	-	11.8, 30 mV	-	46
A/C@P@$PtTe_2$	37	28	-	-	2.45, 150 mV	47
Pt_1/NMHCS	56	40	0.412	2.07, 50 mV	4.47, 100 mV	48
Pt_{doped}@WC_x	20	4	-	14.3, 100 mV	14.1, 100 mV	13
Pt SA/WO_{3-x}	45	38	0.196	12.8, 50 mV	35.0, 100 mV	49
K_2PtCl_4@NC-M	21	11	0.294	5.6, 20 mV	6.1, 100 mV	50
$Pt_{61}La_{39}$@KB	29	21	0.142	5.39, 70 mV	8.73, 70 mV	51

Table S8. The HER activities of recently reported catalysts with hydrogen spillover effect.

Samples	Electrolyte	Tafel slopes (mV dec^{-1})	η(mV)	Ref
Ru-WO_{3-x}/CP	1.0 M PBS	41	19, 10 mA·cm^{-2}	22
PtIr/CoP	0.5 M H_2SO_4	25.2	7, 20 mA·cm^{-2}	14
$La_2Sr_2PtO_{7+\delta}$	0.5 M H_2SO_4	22	13, 10 mA·cm^{-2}	19
PtNiP NWs	1 M KOH	39.2	24, 10 mA·cm^{-2}	52
Ru_1Fe_1/CoP	0.5 M H_2SO_4	24.5	6, 20mA·cm^{-2}	53
PtCu/WO_3@CF	0.5 M H_2SO_4	45.9	41, 10 mA·cm^{-2}	54
Pt/$RuCeO_x$@PA	0.5 M H_2SO_4	31	41, 10 mA·cm^{-2}	55
MoS_2/$NiPS_3$	1 M KOH	64	112, 10 mA·cm^{-2}	56
OH-Ni/Ni_3C	1 M KOH	106.3	72, 10 mA·cm^{-2}	57
Pt-CoP	0.5 M H_2SO_4	28.2	53, 10 mA·cm^{-2}	58
IrGe	0.5 M H_2SO_4	27.8	12, 10 mA·cm^{-2}	59
Ru/NCDs	0.5 M H_2SO_4	25	12, 10 mA·cm^{-2}	60

Table S9. Comparison of Pt/POMs-contained composite catalysts for HER.

Catalysts	Synthesis	Interaction between POM and supporting	Pt states	Pt (wt%)	Mass activity @30 mV (A mg^{-1}_{Pt})	Tafel slopes (mV dec^{-1})	η_{10} (mV)	Ref.
Pt NPs@POMOF-1/KB	Adsorption and light-reduction method	Coordination interaction	Nanoparticles	0.43	2.68	71.29	23	[26]
Pt-$SiW_{11}Co/SiW_{11}Co$-CNP	Hydrothermal method-anodic dissolution-cathodic deposition	With no supports (deposition)	Composite	-	-	61	150	[30]
Pt-STA-CB	Hydrothermal method-heated-reduction	Loading	Clusters	1.2	1.32	33.8	27.9	[27]
SiW_{11}-Pt	Electrochemical deposition	With no supports (deposition)	Composite	-	-	32	65	[28]
[TTMAP/$Ti_{12}P_8W_{60}$@Pt]$_n$ [TTMAP/$Zn_4P_4W_{30}$@Pt]$_n$	Photochemical reduction followed self-assembly	With no support (film)	Nanoparticles	1.97 8.5	-	-	-	[61]
PtW_6O_{24}/C	Cation exchange method	Loading	Compound	1	3.68	29.8	22	[29]
$Pt_2(W_5O_{18})_2$/C	Cation exchange method	Loading	Compound	1	2.004	29.5	26	[14]
Pt_1@PMo_{12}@PC	Dual-confinement impregnation	Confining	Single-atom	2.15	18.8	14.8	8.3	This work
Pt_1@PW_{12}@PC	Dual-confinement impregnation	Confining	Single-atom	3.5	25.21	15.4	3.76	This work
Pt_1@$SiMo_{12}$@PC	Dual-confinement impregnation	Confining	Single-atom	3.81	17.23	9.76	6.12	This work
Pt_1@SiW_{12}@PC	Dual-confinement impregnation	Confining	Single-atom	3.1	10.17	18.5	6.8	This work

Table S10. Fitted data of EIS Nyquist plots by the equivalent circuit for Pt_1@PC, Pt_1@POMs@PC, and Pt-POMs/AC.

Catalyst	η(mV)	Rs	CPE_1	R_1	CPE_2	R_3	$C_φ$(F)	R_2
	0	8.25	0.00093	3.933	0.013	4.80	0.0097	1301
	5	8.22	0.00092	3.68	0.020	4.92	0.013	120.1
	10	8.25	0.0013	3.48	0.036	3.18	0.018	13.89
	15	8.39	0.00082	2.62	0.041	2.45	0.022	3.46
Pt_1@PC	20	8.41	0.00092	2.9	0.034	2.36	0.026	0.63
	25	8.60	0.00092	2.93	0.031	2.08	0.028	0.32
	30	8.67	0.00095	2.65	0.026	1.74	0.033	0.28
	35	8.56	0.00097	2.25	0.031	1.87	0.034	0.24
	40	8.86	0.00064	2.08	0.052	1.75	0.036	0.16
	0	8.47	6.76E-5	0.69	0.0031	9.86	0.013	2196
	5	8.47	8.76E-5	0.59	0.0034	8.19	0.019	458.5
	10	8.65	3.40E-5	0.69	0.0016	6.06	0.032	54.9
	15	9.41	3.12E-5	0.71	0.0015	5.22	0.048	15.7
Pt_1@PW_{12}@PC	20	9.63	2.13E-5	0.60	0.0014	4.68	0.054	5.80
	25	8.87	2.07E-5	0.70	0.0013	4.26	0.064	4.09
	30	8.89	3.89E-5	0.73	0.0013	4.10	0.078	3.38
	35	9.17	2.13E-5	0.88	0.0013	4.09	0.091	2.74
	40	9.79	3.00E-5	0.99	0.0012	3.90	0.099	2.55
	0	8.73	2.35E-5	7.24	0.00019	1682	0.0018	5927
	5	8.70	3.01E-5	7.66	0.00016	1148	0.0027	3060
	10	9.08	2.71E-5	7.06	0.00017	754.8	0.0042	1803
	15	9.00	2.80E-5	7.08	0.00014	607.4	0.0052	339.4
Pt-PW_{12}/AC	20	9.57	3.95E-5	7.71	0.00013	455.2	0.0058	128.3
	25	9.58	3.09E-5	6.75	0.00013	354.7	0.0071	63.19
	30	9.31	4.09E-5	6.90	0.00013	267.6	0.0082	35.90
	35	9.60	4.79E-5	6.94	0.00013	194.7	0.0099	20.15
	40	10.25	3.51E-5	6.02	0.00016	139.8	0.012	18.51
	0	9.06	0.00016	2.02	0.0052	17.49	0.014	5143
	5	8.93	0.00016	2.20	0.0073	15.3	0.019	770.8
	10	9.38	0.00014	2.06	0.0034	9.47	0.039	63.63
	15	9.24	0.00014	2.06	0.0033	8.31	0.084	11.49
Pt_1@PMo_{12}@PC	20	9.42	0.00017	2.23	0.0027	6.16	0.10	2.23
	25	9.14	0.00025	2.35	0.0027	6.26	0.12	2.17
	30	9.27	0.00022	2.35	0.0032	6.42	0.13	1.11
	35	9.79	0.00016	2.07	0.0044	5.75	0.14	1.07
	40	9.07	0.00014	2.17	0.0038	5.65	0.16	0.97
	0	8.39	6.83E-5	6.10	0.00016	780.3	0.0026	2196
	5	8.40	8.21E-5	6.46	0.00015	574.7	0.0034	458.5
	10	8.15	4.61E-5	6.30	0.00015	430.3	0.0044	54.32
	15	7.86	4.21E-5	7.09	0.00015	325.1	0.0055	15.47
Pt-PMo_{12}/AC	20	8.19	5.01E-5	6.43	0.00017	252.6	0.0068	5.52
	25	8.31	5.87E-5	5.88	0.00019	199.0	0.0076	3.91
	30	8.61	5.67E-5	6.44	0.00020	154.5	0.0089	3.25
	35	8.55	6.89E-5	5.52	0.00026	118.0	0.0095	2.88
	40	9.23	5.33E-5	4.42	0.00035	74.39	0.0117	2.79
	0	7.91	1.92E-5	0.89	0.0023	9.203	0.017	2093
	5	8.53	1.47E-5	0.79	0.0022	7.65	0.025	231.2
	10	8.27	2.77E-5	0.93	0.0014	5.17	0.043	24.4
Pt_1@SiW_{12}@PC	15	8.39	2.83E-5	0.86	0.0012	4.36	0.065	6.53
	20	8.55	3.25E-5	0.97	0.0011	4.07	0.071	3.28
	25	8.22	3.25E-5	1.07	0.0008	3.36	0.082	2.69
	30	8.20	4.81E-5	1.14	0.0008	3.28	0.093	2.48
	35	8.29	4.09E-5	1.19	0.0007	2.89	0.099	2.22

	40	8.56	4.17E-5	1.25	0.0007	1.00	0.113	1.01
$Pt\text{-}SiW_{12}/AC$	0	8.69	0.00017	7.41	0.00018	1292	0.0022	4918
	5	8.90	0.00015	8.16	0.00016	870.7	0.0039	2075
	10	9.01	0.00020	9.40	0.00015	632.4	0.0054	562.5
	15	9.16	0.00022	9.37	0.00014	467.7	0.0083	215.7
	20	9.23	0.00029	10.56	0.00014	329.3	0.011	98.31
	25	8.82	0.00083	9.28	0.00018	219.2	0.013	72.11
	30	9.71	0.00049	10.76	0.00016	143.3	0.014	56.70
	35	9.87	0.00076	9.45	0.00029	81.11	0.015	32.21
	40	9.75	0.00076	7.44	0.00025	68.35	0.017	17.56
$Pt@SiMo_{12}@PC$	0	8.58	4.91E-5	2.62	0.0027	16.50	0.018	4323
	5	8.67	4.74E-5	2.58	0.0024	13.28	0.026	587.9
	10	8.50	6.52E-5	2.86	0.0019	10.60	0.044	47.16
	15	8.57	5.84E-5	2.73	0.0023	9.77	0.074	8.42
	20	8.58	6.19E-5	2.73	0.0023	9.34	0.098	2.21
	25	8.56	6.29E-5	2.73	0.0025	9.04	0.11	1.07
	30	8.70	7.72E-5	2.88	0.0029	8.67	0.12	0.69
	35	8.64	6.83E-5	2.60	0.0031	8.25	0.13	0.58
	40	8.70	7.07E-5	2.39	0.0038	7.81	0.14	0.50
$Pt\text{-}SiMo_{12}/AC$	0	8.40	1.07E-5	9.96	8.92E-5	1408	0.0021	17219
	5	8.21	1.44E-5	10.36	8.24E-5	965.6	0.0028	4314
	10	8.26	2.09E-5	10.24	7.70E-5	658.8	0.0040	878.5
	15	8.24	2.52E-5	9.87	8.07E-5	485.8	0.0052	290.5
	20	8.24	2.87E-5	9.00	8.53E-5	353.4	0.0067	136.7
	25	8.33	3.74E-5	8.84	9.25E-5	283.3	0.0083	55.29
	30	8.30	5.87E-5	8.37	0.00010	216.5	0.0094	21.85
	35	8.49	0.00010	7.19	0.00013	155.7	0.0096	9.84
	40	10.53	0.00021	6.13	0.00022	96.58	0.0138	5.12

Table S11. Electron transfer based on Hirshfeld population analysis.

Label	Q(Pt), Hirshfeld
Pt_1@PMo_{12}@G-01	5.57
Pt_1@PMo_{12}/G	4.56
Pt_1@PW_{12}@G-01	3.41
Pt_1@PW_{12}/G	3.42
Pt_1@$SiMo_{12}$@G-01	5.52
Pt_1@$SiMo_{12}$/G	4.49
Pt_1@SiW_{12}@PC-01	3.43
Pt_1@SiW_{12}/G	3.47
Pt_1@G(O)	2.88

* Positive value means Pt is losing electrons.

Table S12. Contents of Pt and M (Mo or W) in Pt_1@PC and Pt_1@POMs@PC by ICP-OES.

Catalysts	**Pt (wt%)**	**Mo (wt%)**	**W(wt%)**
Pt_1@ PC	6.63	——	——
$Pt_1@PMo_{12}$@PC	2.15	7.92	——
$Pt_1@SiMo_{12}$@PC	3.81	7.69	——
$Pt_1@PW_{12}$@PC	3.50	——	15.38
$Pt_1@SiW_{12}$@PC	3.10	——	14.89

Table S13. The calculated elemental compositions by XPS spectra.

Catalysts	Pt (at%)	Mo (at%)	W (at%)	C (at%)	O (at%)	P(at%)	Si (at%)
Pt_1@PC	0.31	——	——	94.24	0.05	——	——
PMo_{12}@PC	——	0.82	——	91.88	6.88	0.41	——
Pt_1@PMo_{12}@PC	0.19	0.75	——	90.8	6.55	0.45	——
$SiMo_{12}$@PC	——	0.78	——	91.07	7.72	——	0.43
Pt_1@$SiMo_{12}$@PC	0.23	0.5	——	90.62	6.55	——	0.69
PW_{12}@PC	——	——	0.9	91.39	7.20	0.52	——
PC@PW_{12}@Pt_1	0.25	——	0.77	90.34	6.57	0.25	——
PC@SiW_{12}	——	——	0.59	92.6	6.37	——	0.5
Pt_1@SiW_{12}@PC	0.24	——	0.58	91.27	5.94	——	0.9
Catalysts	**Pt (wt%)**	**Mo (wt%)**	**W (wt%)**	**C (wt%)**	**O (wt%)**	**P(wt%)**	**Si (wt%)**
Pt_1@PC	4.61	——	——	86.38	4.72	——	——
PMo_{12}@PC	——	6.03	——	84.56	8.43	0.97	——
Pt_1@PMo_{12}@PC	2.72	5.28	——	79.98	7.69	1.02	——
$SiMo_{12}$@PC	——	5.74	——	83.90	9.48	——	0.93
Pt_1@$SiMo_{12}$@PC	3.31	3.54	——	80.30	7.74	——	1.43
PW_{12}@PC	——	——	11.8	78.70	1.15	1.16	——
Pt_1@PW_{12}@PC	3.40	——	9.76	74.75	7.24	1.47	——
SiW_{12}@PC	——	——	8.12	83.19	7.63	——	1.05
Pt_1@SiW_{12}@PC	3.33	——	7.57	77.82	6.75	——	1.80

As revealed by the calculated elemental compositions (**Table S11**), the Pt content in Pt_1@POMs@PC is lower than that in the Pt_1@PC, which is in line with the ICP-OES results (**Table S12**).

Note S1

Keggin-structure POMs show a classical structure with one P/Si atom in the center that is caged by 12 octahedral MoO_6/WO_6-units linked together by 24 bridging oxygen atoms (O_{br}). Another 12 corner oxygen atoms (O_c) complete the structure, each of which is double-bonded with an additional Mo/W atom. Due to the exposed 36 oxygen atoms, POMs furnishes a range of coordination sites (**Fig. 1a**) made of the single corner site, the bridge site (the O_c-O_{br}-bridge site), the threefold hollow site (O_c 3H and O_{br} 3H), and the four-fold hollow site (O4H).[17]

Note S2

In the Pt_1@POMs@PC system, the HER can be split into three parts: (i) the protons are adsorbed on the Pt surfaces and reduced to hydrogen atoms (Volmer), (ii) the hydrogen atoms migrate via the H-buffer chains (Pt→O_{br}→O3H→Mo/W→O_c→$PC_{sub\text{-}1\text{-}nm}$) (H-spillover), and (iii) absorbed H atoms combine to generate the hydrogen molecules which are desorbed (Tafel).

The corresponding reactions are as follows [62, 63]:

$H^+ + e \rightarrow H^*(Pt)$ (i)

$H^*(Pt) \rightarrow H^*(O_{br}) \rightarrow H^*(O3H) \rightarrow H^*(Mo/W) \rightarrow H^*(O_c) \rightarrow H^*(PC_{sub\text{-}1\text{-}nm})$ (ii)

$2H^*(PC_{sub\text{-}1\text{-}nm}) \rightarrow H_2$ (iii)

For the Volmer−H-spillover−Tafel reaction on Pt_1@POMs@PC, the derivation process of the Tafel slope is as follows:

Assuming θ^0_{POMs-H} is the hydrogen coverage on POMs at equilibrium potential.

At certain overpotential *V*,

$$\theta_{POMs-H} = \theta^0_{POMs-H}\, exp\left(-\frac{FV}{RT}\right) \quad \text{(iv)}$$

The concentration of hydrogen ions under an electric field is

$$C_{H*} exp\left(-\frac{\alpha FV}{RT}\right) \quad \text{(v)}$$

The hydrogen coverage on the Pt surface was determined by hydrogen concentration and the hydrogen coverage on the POMs surface:

$$\theta_{Pt-H} = k_1 \theta_{POMs-H}\, C_{H*} exp\left(-\frac{\alpha FV}{RT}\right) = k_1 \theta^0_{POMs-H} C_{H*} exp\left(-\frac{(1+\alpha)FV}{RT}\right) \quad \text{(vi)}$$

On Pt surface, the adsorbed hydrogen atoms combine to form a hydrogen molecule:

$$-j_c = 2Fk_0\theta^2_{Pt-H} = 2Fk_0k_1^2(\theta^0_{POMs-H})^2 C^2_{H*} exp\left(-\frac{2(1+\alpha)FV}{RT}\right) \quad \text{(vii)}$$

$$\lg(-j) = Const + 2\lg C_{H*} - \frac{2(1+\alpha)FV}{2.303RT} \quad \text{(viii)}$$

Therefore, the Tafel slope is:

$$\frac{2(1+\alpha)FV}{2.303RT} \quad \text{(ix)}$$

The partial order for pH of 2 is the reaction order of $\lg C_{H*}$ from equation (viii), which is deduced on the complete coverage of H* in the ideal state. Therefore, when the slope (log *j* vs. pH) for Pt_1@POMs@PC approaches the theoretical value of 2, it signifies nearly unhindered migration of H*, representing the occurrence of H-spillover. So, that partial order concerning pH of 2 can represent the H-spillover involved mechanism.

Note S3

The relationship between the exchange current (j_0) and the Tafel slope as follows[20, 21]:

The dependence of overpotential on exchange current and Tafel slope is given by

$$\eta = b\ log\ \frac{j}{j_0} \qquad (1)$$

To analyze the key determinants of j_0, it was necessary to utilize the Arrhenius equation. The Arrhenius equation (eq 2) gives the temperature dependence of the rate constant of any chemical reaction.

$$k = A_{freq} exp\left(\frac{-E_{act}}{RT}\right) \qquad (2)$$

where A_{freq} is collision frequency. The activation energy (E_{act}) is enthalpy that comprises activation free energy (ΔG_{act}) and activation entropy (ΔS_{act}). For HER, the free energy of activation depends on the standard free energy of activation (ΔG^*), the adsorption energy of intermediate formation (ΔG_{ad}), and the electrode potential. Then the rate constant becomes

$$k = A_{freq} exp\left(\frac{-\triangle S_{act}}{RT}\right) exp\left(\frac{-\triangle G^*}{RT}\right) exp\left(\frac{-\gamma \triangle G_{ad}}{RT}\right) exp\left(\frac{-\beta F E_{rev}}{RT}\right) \qquad (3)$$

The most general equation for the rate of reaction in electrochemistry shows a direct relationship between the current density and the rate constant (k) concerning the (over)potential and the concentration of all reactants ($\Pi_i c_i^R$). This equation is related to the rate determination step:

$$j = nF\Pi_i c_i^R k \qquad (4)$$

By plugging the rate constant (eq. 3) into the equation for current density (eq. 4), where the reactants are protons capable of adsorbing on the surface of the metal (sites not yet occupied by intermediates) on the available active site, eq. 4 can be obtained:

$$j = nFc^p(\mathrm{H^+})(1-\theta)^q A_{freq} exp\left(\frac{-\triangle S_{act}}{RT}\right) exp\left(\frac{-\triangle G^*}{RT}\right) exp\left(\frac{-\gamma \triangle G_{ad}}{RT}\right) exp\left(\frac{-\beta F E_{rev}}{RT}\right) \qquad (5)$$

If we are at reversible potential and we transform the reaction rate (eq. 5) into a semilogarithmic relation, we get

$$log j_0 = \log\left(nFc^p(\mathrm{H^+})(1-\theta)^q A_{freq}\right) + \frac{1}{2.303}\left(\frac{-\triangle S_{act}}{RT} + \frac{-\triangle G^*}{RT} + \frac{-\beta F E_{rev}}{RT} + \frac{-\gamma \triangle G_{ad}}{RT}\right) \qquad (6)$$

Finally, we obtain a form of the equation that is relevant to the experimental work

$$log j_0 = \log A - \frac{E_{act}}{2.303RT} \qquad (7)$$

Note S4

X-ray absorption fine structure (XAFS) including X-ray absorption near-edge structure (XANES) and extended X-ray absorption fine structure (EXAFS) of the Pt_1@PMo_{12}@PC and Pt_1@PC were collected at the SPring-8 14b2, where a pair of channel-cut Si (111) crystals was used in the monochromator. The storage ring was working at the energy of 8.0 GeV with an average electron current of 99.5 mA. Data reduction, data analysis, and EXAFS fitting were performed and analyzed with the Athena and Artemis programs of the Demeter data analysis packages[64] that utilize the FEFF6 program[65] to fit the EXAFS data. The energy calibration of the sample was conducted through standard and Pt foil and Mo foil, which as a reference was simultaneously measured. A linear function was subtracted from the pre-edge region, then the edge jump was normalized using Athena software. The χ(k) data were isolated by subtracting a smooth, third-order polynomial approximating the absorption background of an isolated atom. The *k*3-weighted $\chi(k)$ data were Fourier transformed after applying a HanFeng window function (Δk = 1.0). For EXAFS modeling, The global amplitude EXAFS (*CN*, *R*, σ^2 and ΔE_0) were obtained by nonlinear fitting, with least-squares refinement, of the EXAFS equation to the Fourier-transformed data in *R*-space, using Artemis software, EXAFS of the Pt foil and Mo foil are fitted and the obtained amplitude reduction factor S_0^2 value (0.756 and 0.938) was set in the EXAFS analysis to determine the coordination numbers (*CNs*) in the Pt−O, Pt−Cl and Mo−O scattering path in sample.

Note S5

The C_{dl} was obtained based on the CV of the double-layer region (non-Faradaic reaction region).[22] By plotting $\Delta j/2 = (j_{anodic} - j_{cathodic})/2$ against the scan rates (5, 10, 20, 40, 60, 80, 100, 120, 140, 160, 180, and 200 mV s^{-1}), the slope of the fitting line was regarded as the geometric C_{dl} of the sample. The j_{anodic} and $j_{cathodic}$ indicate the current density of the anodic and cathodic sweeps at the midpoint of the potential region, respectively. Moreover, ECSA is calculated by assuming a standard value of C_{dlref} (60 μF cm^{-2}):[66] ECSA= $\frac{C_{dl}}{C_{dlref}}$.

The mass activity is calculated based on the following equation: $\text{Mass Activity} = \frac{I}{m}$, where I (A) is the measured current, m (mg) is the mass of Pt loaded on the glassy carbon electrode. The turnover frequency (TOF) is calculated based on the following equation:[67] $TOF = \frac{1}{2\text{F}n}$, where I (A) is the measured current, F is the Faraday constant (96485 C mol^{-1}), $n = \frac{m}{M}$, n (mol) is the molar amount of Pt loaded on the glassy carbon electrode, m is the mass of Pt, and M is the molecule weight.

Note S6

The binding energy (E_b) of Pt in Pt@G(O) is defined as:

$$E_b = E(Pt_1@G(O)) - E(G(O)) - E(Pt)$$

The binding energy (E_b) of Pt in Pt_1@G(O/POM) is defined as:

$$E_b = E(Pt_1@G(O/POM)) - E(G(O/POM)) - E(Pt)$$

The binding energy (E_b) of Pt in $PtCl_3$-O_2@G is defined as:

$$E_b = E(PtCl_3\text{-}O_2@G) - E(O_2@G) - E(PtCl_3)$$

The binding energy (E_b) of Pt in Pt_1@POMs/G is defined as:

$$E_b = E(Pt_1@POMs/G) - E(POMs/G) - E(Pt)$$

Note S7

The charge density difference of Pt@G(O) is defined as:

$$\Delta\rho = \rho(Pt_1@G(O)) - \rho(G(O)) - \rho(Pt)$$

The binding energy (E_b) of Pt in $PtCl_3$-O_2@G is defined as:

$$\Delta\rho = \rho(PtCl_3\text{-}O_2@G) - \rho(O_2@G) - \rho(PtCl_3)$$

The binding energy (E_b) of Pt in Pt_1@POMs/G is defined as:

$$\Delta\rho = \rho(Pt_1@POMs/G) - \rho(POMs/G) - \rho(Pt)$$

Reference

1. S. Yang, M. Wang, Y. Zhang, P. He, W. Cong, C. Wang, Q. Yang, X. Liu, T. Wang, X. Zhang and J. Zhou, *Energy Environ. Mater.*, 2022, **6**, e12396.
2. C. Bannwarth, E. Caldeweyher, S. Ehlert, A. Hansen, P. Pracht, J. Seibert, S. Spicher and S. Grimme, *WIREs Comput. Mol. Sci.*, 2020, **11**, e1493.
3. R. Kobayashi, M. A. Addicoat, A. T. B. Gilbert, R. D. Amos and M. A. Collins, *WIREs Comput. Mol. Sci.*, 2019, **9**, e1413.
4. P. Král, *Nat. Mater.*, 2019, **18**, 99–101.
5. A. Govind Rajan, K. S. Silmore, J. Swett, A. W. Robertson, J. H. Warner, D. Blankschtein and M. S. Strano, *Nat. Mater.*, 2019, **18**, 129–135.
6. R. Tran, Z. Xu, B. Radhakrishnan, D. Winston, W. Sun, K. A. Persson and S. P. Ong, *Sci. Data*, 2016, **3**, 160080.
7. T. Lu and F. Chen, *J. Comput. Chem.*, 2011, **33**, 580–592.
8. J. K. Nørskov, T. Bligaard, A. Logadottir, J. R. Kitchin, J. G. Chen, S. Pandelov and U. Stimming, *J. Electrochem. Soc.*, 2005, **152**, J23–J26.
9. S. Spicher and S. Grimme, *Angew. Chem. Int. Ed.*, 2020, **59**, 15665-15673.
10. Y. Liu, X. Wu, Z. Li, J. Zhang, S.-X. Liu, S. Liu, L. Gu, L. R. Zheng, J. Li, D. Wang and Y. Li, *Nat. Commun.*, 2021, **12**, 4202.
11. B. Zhang, G. Sun, S. Ding, H. Asakura, J. Zhang, P. Sautet and N. Yan, *J. Am. Chem. Soc.*, 2019, **141**, 8185-8197.
12. W. Wang, J. Zhou, Z. Wang, L. Zhao, P. Li, Y. Yang, C. Yang, H. Huang and S. Guo, *Adv. Energy Mater.*, 2018, **8**.
13. T. Ma, H. Cao, S. Li, S. Cao, Z. Zhao, Z. Wu, R. Yan, C. Yang, Y. Wang, P. A. V. Aken, L. Qiu, Y. G. Wang and C. Cheng, *Adv. Mater.*, 2022, **34**, e2206368.
14. F. Y. Yu, Z. L. Lang, Y. J. Zhou, K. Feng, H. Q. Tan, J. Zhong, S. T. Lee, Z. H. Kang and Y. G. Li, *ACS Energy Lett.*, 2021, **6**, 4055–4062.
15. Q. Y. Li, L. Zhang, Y. X. Xu, Q. Li, H. Xue and H. Pang, *ACS Sustain. Chem. Eng.*, 2019, **7**, 5027–5033.
16. Y. Liu, J. Ding, F. Li, X. Su, Q. Zhang, G. Guan, F. Hu, J. Zhang, Q. Wang, Y. Jiang, B. Liu and H. B. Yang, *Adv. Mater.*, 2023, **35**, e2207114.
17. B. Zhang, H. Asakura, J. Zhang, J. Zhang, S. De and N. Yan, *Angew. Chem. Int. Ed.*, 2016, **55**, 8319–8323.
18. J. Ohyama, D. Kumada and A. Satsuma, *J. Mater. Chem. A*, 2016, **4**, 15980-15985.
19. J. Dai, Y. Zhu, Y. Chen, X. Wen, M. Long, X. Wu, Z. Hu, D. Guan, X. Wang, C. Zhou, Q. Lin, Y. Sun, S.-C. Weng, H. Wang, W. Zhou and Z. Shao, *Nat. Commun.*, 2022, **13**, 1189.
20. P. Narangoda, I. Spanos, J. Masa, R. Schlögl and A. R. Zeradjanin, *ChemElectroChem*, 2022, **9**, e202101278.
21. A. R. Zeradjanin, P. Narangoda, J. Masa and R. Schlögl, *ACS Catal.*, 2022, **12**, 11597-11605.
22. J. Chen, C. Chen, M. Qin, B. Li, B. Lin, Q. Mao, H. Yang, B. Liu and Y. Wang, *Nat. Commun.*, 2022, **13**, 5382.
23. J. Wu, X. Wang, W. Zheng, Y. Sun, Y. Xie, K. Ma, Z. Zhang, Q. Liao, Z. Tian, Z. Kang and Y. Zhang, *J. Am. Chem. Soc.*, 2022, **144**, 19163–19172.
24. T. M. Nahir and E. F. Bowden, *J. Electroanal. Chem.*, 1996, **410**, 9−13.

25. S. Sun and S. Chen, *Electrocatalysis*, Beijing: Chemical Industry Press, 2013.
26. H. Peng, X. Yang, Y. Ma, J. Liu, Y. Wang, H. Tan and Y. Li, *CrystEngComm*, 2018, **20**, 5387-5394.
27. T. Zhang, S. Weng, X. Wang, Z. Zhang, Y. Gao, T. Lin, Y. Zhu, W. Zhang and C. Sun, *J. Colloid Interface Sci.*, 2022, **624**, 704-712.
28. C. Zhang, Y. Hong, R. Dai, X. Lin, L.-S. Long, C. Wang and W. Lin, *ACS Appl. Mater. Interfaces*, 2015, **7**, 11648-11653.
29. F. Y. Yu, Z. L. Lang, L. Y. Yin, K. Feng, Y. J. Xia, H. Q. Tan, H. T. Zhu, J. Zhong, Z. H. Kang and Y. G. Li, *Nat. Commun.*, 2020, **11**, 490.
30. R. Hashemniaye Torshizi, N. Ashraf, M. H. Arbab Zavar and S. Dianat, *Catal. Sci. Technol.* , 2020, **11**, 1098−1109.
31. J. Zhu, Y. Cen, H. Ma, W. Lian, J. Liu, H. Ou, F. Ouyang, L. Zhang and W. Zhang, *Nanoscale Horiz.*, 2023, **8**, 1273–1281.
32. S. Zhai, D. Zhai, L. Sun, N. Feng, X. Chen, W.-Q. Deng and H. Wu, *Mater. Chem. Front.*, 2023, **7**, 2889–2895.
33. C. Wang, H. Zang, C. Liu, J. Wang, L. Kuai and B. Geng, *Inorg. Chem.*, 2023, **62**, 6856–6863.
34. S. J. Park, T. H. Nguyen, D. T. Tran, V. A. Dinh, J. H. Lee and N. H. Kim, *Energy Environ. Sci.*, 2023, **16**, 4093–4104.
35. H. Ying, D. Hengli, L. Wei, Z. Chenhui, W. Baoshun, J. Qinyuan, F. Sihua, Y. Wensheng, T. Ting and Z. Rufan, *Appl. Catal. B*, 2023, **335**, 122898.
36. J. Zhang, M. Wang, T. Wan, H. Shi, A. Lv, W. Xiao and S. Jiao, *Adv. Mater.*, 2022, **34**, 2206960.
37. G. Zhan, Y. Yao, F. Quan, H. Gu, X. Liu and L. Zhang, *J. Energy Chem.*, 2022, **72**, 203−209.
38. S. Jiao, M. Kong, Z. Hu, S. Zhou, X. Xu and L. Liu, *Small*, 2022, **18**, 2105129.
39. W. Zhong, W. Tu, Z. Wang, Z. Lin, A. Xu, X. Ye, D. Chen and B. Xiao, *J. Energy Chem.*, 2020, **51**, 280−284.
40. Y. H. Lai, S. R. Li, S. M. G., H. T. Chang, Y. B. Huang, Y. K. Li, Y. M. Chen, S. B. Patil, S. Y. Chang, P. K. Chen, C. C. Chang, Y. C. Chen, C. W. Pao, J. L. Chen, C. Y. Wei, I. K. Lin, H. L. Chou, C. J. Su, U. S. Jeng, T. R. Kuo, C. Y. Wen and D. Y. Wang, *J. Mater. Chem. A*, 2021, **9**, 22901−22912.
41. D. Kobayashi, H. Kobayashi, D. Wu, S. Okazoe, K. Kusada, T. Yamamoto, T. Toriyama, S. Matsumura, S. Kawaguchi, Y. Kubota, S. M. Aspera, H. Nakanishi, S. Arai and H. Kitagawa, *J. Am. Chem. Soc.*, 2020, **142**, 17250–17254.
42. X. P. Yin, H. J. Wang, S. F. Tang, X. L. Lu, M. Shu, R. Si and T. B. Lu, *Angew. Chem. Int. Ed.*, 2018, **57**, 9382−9386.
43. C. Li, Z. Chen, H. Yi, Y. Cao, L. Du, Y. Hu, F. Kong, R. Kramer Campen, Y. Gao, C. Du, G. Yin, I. Y. Zhang and Y. Tong, *Angew. Chem. Int. Ed.*, 2020, **59**, 15902−15907.
44. M. Sun, J. Ji, M. Hu, M. Weng, Y. Zhang, H. Yu, J. Tang, J. Zheng, Z. Jiang, F. Pan, C. Liang and Z. Lin, *ACS Catal.*, 2019, **9**, 8213–8223.
45. H. Tian, X. Cui, L. Zeng, L. Su, Y. Song and J. Shi, *J. Mater. Chem. A*, 2019, **7**, 6285−6293.
46. S. Ye, F. Luo, Q. Zhang, P. Zhang, T. Xu, Q. Wang, D. He, L. Guo, Y. Zhang, C. He, X.

Ouyang, M. Gu, J. Liu and X. Sun, *Energy Environ. Sci.*, 2018, **12**, 1000−1007.
47. H. Ma, X. Huang, L. Li, W. Peng, S. Lin, Y. Ding and L. Mai, *Small*, 2023, **19**, 2302685.
48. P. Kuang, Y. Wang, B. Zhu, F. Xia, C. W. Tung, J. Wu, H. M. Chen and J. Yu, *Adv. Mater.*, 2021, **33**, 2008599.
49. J. Park, S. Lee, H. E. Kim, A. Cho, S. Kim, Y. Ye, J. W. Han, H. Lee, J. H. Jang and J. Lee, *Angew. Chem. Int. Ed.*, 2019, **58**, 16038–16042.
50. H. Jin, S. Sultan, M. Ha, J. N. Tiwari, M. G. Kim and K. S. Kim, *Adv. Funct. Mater.*, 2020, **30**, 2000531.
51. N. Nie, D. Zhang, Z. Wang, Y. Qin, X. Zhai, B. Yang, J. Lai and L. Wang, *Small*, 2021, **17**, 2102879.
52. W. Lai, P. Yu, L. Gao, Z. Yang, B. He and H. Huang, *J. Mater. Chem. A*, 2022, **10**, 16834−16841.
53. Z. Zeb, Y. Huang, L. Chen, W. Zhou, M. Liao, Y. Jiang, H. Li, L. Wang, L. Wang, H. Wang, T. Wei, D. Zang, Z. Fan and Y. Wei, *Coordination Chemistry Reviews*, 2023, **482**, 215058.
54. H. Yan, X. Qin, J. C. Liu, L. Cai, P. Xu, J. J. Song, C. Ma, W. W. Wang, Z. Jin and C. J. Jia, *J Catal*, 2022, **413**, 703–712.
55. T. Liu, W. Gao, Q. Wang, M. Dou, Z. Zhang and F. Wang, *Angew. Chem. Int. Ed.*, 2020, **59**, 20423–20427.
56. Y. Liu, Y. Chen, Y. Tian, T. Sakthivel, H. Liu, S. Guo, H. Zeng and Z. Dai, *Adv. Mater.*, 2022, **34**, 2203615.
57. Q. Wen, J. Duan, W. Wang, D. Huang, Y. Liu, Y. Shi, J. Fang, A. Nie, H. Li and T. Zhai, *Angew. Chem. Int. Ed.*, 2022, **61**, e202206077.
58. Y. N. Zhou, X. Liu, C. J. Yu, B. Dong, G. Q. Han, H. J. Liu, R. Q. Lv, B. Liu and Y. M. Chai, *J. Mater. Chem. A*, 2023, **11**, 6945−6951.
59. Z. Li, L. Sheng, R. Deng, Z. Zheng, P. Hou, M. Chen, Z. Ma, K. Sun, Y. Wang, Q. Liu, P. Xu, X. Ma and H. Chu, *ACS Energy Lett.*, 2023, **8**, 5136-5142.
60. Z. Liu, H. Zhang, D. Liu, Y. Feng, D. Jia, C. Li, Q. Sun, Y. Zhou, Z. Kang and B. Li, *J. Mater. Chem. A*, 2024, DOI: 10.1039/D3TA07016F.
61. D. Zang, Z. Huo, S. Yang, Q. Li, G. Dai, M. Zeng, L. Ruhlmann and Y. Wei, *Mater. Today Commun.*, 2022, **31**, 103811.
62. M. Sheng, B. Jiang, B. Wu, F. Liao, X. Fan, H. Lin, Y. Li, Y. Lifshitz, S.-T. Lee and M. Shao, *ACS Nano*, 2019, **13**, 2786-2794.
63. J. Li, J. Hu, M. Zhang, W. Gou, S. Zhang, Z. Chen, Y. Qu and Y. Ma, *Nat. Commun.*, 2021, **12**, 3502.
64. B. Ravel and M. Newville, *J. Synchrotron Radiat.*, 2005, **12**, 537–541.
65. S. I. Zabinsky, J. J. Rehr, A. Ankudinov, R. C. Albers and M. J. Eller, *Phys. Rev. B*, 1995, **52**, 2995–3009.
66. Y. Huang, Q. Gong, X. Song, K. Feng, K. Nie, F. Zhao, Y. Wang, M. Zeng, J. Zhong and Y. Li, *ACS Nano*, 2016, **10**, 11337–11343.
67. X. Xiao, Z. Li, Y. Xiong and Y. W. Yang, *J. Am. Chem. Soc.*, 2023, **145**, 16548–16556.